Optoelectronic properties of the two-dimensional van der Waals semiconductor indium selenide (InSe)

Debarati Mazumder

Thesis submitted to the University of Nottingham

for the degree of Doctor of Philosophy

August 2021

Abstract

This thesis presents an investigation of the optoelectronic properties of the two-dimensional (2D) van der Waals (vdW) semiconductor indium selenide (InSe) and exploits these properties in InSe-graphene vdW heterostructure devices. These heterostructures are fabricated by mechanical exfoliation and dry transfer of InSe and graphene nanosheets. A novel method of device fabrication by needle transfer of graphene microsheets is also described and used for some devices.

The optical properties of InSe nanosheets differ qualitatively from those reported for other 2D materials, such as transition metal dichalcogenides (TMDCs). In particular, this thesis reports on the controlled modulation of optical signals by exploiting the inherent optical anisotropy and mechanical flexibility of atomically thin 2D vdW InSe bent onto a periodic array of silicon (Si) nanopillars.

A series of vertical and planar vdW heterostructures, including tunnelling transistors and photodetectors, are investigated. The optoelectronic transport characteristics of these devices exploit a favourable band alignment between InSe and graphene. Moreover, 2D energy subbands of InSe exhibit strong quantum confinement, offering a route to the modulation of electrical properties. Optical absorption studies on bulk InSe by variable angle spectroscopic ellipsometry (VASE) are presented, which indicates strong resonances in the ultra-violet (UV) range of the absorption spectrum. A fast, ultra-high photoresponsivity is demonstrated in a hybrid phototransistor based on an InSe/graphene heterostructure that exploits the light-induced charge transfer at the interface of InSe and graphene.

Acknowledgements

Firstly, I would like to thank my supervisor, Prof. Amalia Patanè, for her invaluable support and guidance throughout my time in Nottingham. I cannot be luckier to have her as my mentor. I am indebted to her for putting up with me on difficult days and being compassionate especially during the initial months of this PhD and beyond. I am particularly grateful for the time and patience that Amalia has invested in guiding me throughout my research and enabling me to undertake new experiences.

I am eternally grateful to my co-supervisor, Dr Oleg Makarovskyi, for his expertise and assistance with the research and technical aspects of the experiments throughout my PhD.

I am extremely grateful to my co-supervisor, Prof. Laurence Eaves, for all the good times and discussions regarding Physics and cricket.

I would like to thank all current and former members of the Wendy house, particularly Dr Natalia Alexeeva, Dr Nilanthy Balakrishnan, Dr Zakhar Kudrynskyi, Dr Davide Maria Di Paola, Dr Mahabub Bhuiyan, Dr Jake D.G. Greener, Nathan D. Cottam, Dr Wenjing Yan, Anubhab Dey and Shihong Xie, and the visitors, Dr Chengxi Zhang and Dr Quanshan Lv. I thoroughly enjoyed my time here. Special thanks to Dr Kudrynskyi for being kind and cooperative as a co-investigator in many of the experiments. I would like to extend my gratitude to Dr Lyudmila Turynska for the chats during coffee breaks and celebrations over the years and for being supportive all the time.

I would also like to acknowledge the support of our collaborators throughout the course of several research projects, Prof. Lijun Zhang and Jiahao

Xie (Jilin University, China), Dr Christopher Mellor and Richard Cousins (The University of Nottingham), Prof. Diana Huffaker and her group (Cardiff University and University of Los Angeles California) and Prof. Zakhar D. Kovalyuk (Institute for Problems of Materials Science at the National Academy of Sciences of Ukraine, Chernivtsi).

I would like to express my sincere gratitude to all the staff at the School of Physics and Astronomy, The University of Nottingham, particularly, Mr Jas Chauhan for his expertise in cleanroom processes and device fabrication.

I acknowledge the support of the Vice Chancellor's scholarship for research excellence (The University of Nottingham), EU Graphene Flagship project, European Magnetic Field Laboratory (EMFL).

I would like to thank my parents, Mr Benoy Mazumder and Mrs Alo Mazumder, for always believing in me and encouraging me to follow my dreams.

In addition, I express my gratitude to my extended family, my in-laws Mr Kashinath Ghosh and Mrs Kalpana Ghosh, and close friends for their continuous support.

Finally, to my husband, Dr Barun Ghosh, for instilling in me the drive and motivation that has carried me this far. Without you, I would never have had the courage to embark on this journey. And to our little bundle of joy, our son, Deeptarun, for being a sweetheart and making it possible for me to complete what I started. May you always know that you were wished for, longed for, prayed for, and wanted.

List of publications

1. D. Buckley, Z. R. Kudrynskyi, N. Balakrishnan, T. Vincent, D. Mazumder, E. Castanon, Z. D. Kovalyuk, O. Kolosov, O. Kazakova, A. Tzalenchuk, A. Patanè, "Anomalous Low Thermal Conductivity of Atomically Thin InSe Probed by Scanning Thermal Microscopy", *Advanced Functional Materials*, **31**, 2008967 (2021).

2. D. Mazumder, J. Xie, Z. R. Kudrynskyi, X. Wang, O. Makarovsky, M. A. Bhuiyan, H. Kim. T. Y. Chang, D. L. Huffaker, Z. D. Kovalyuk, L. Zhang, A. Patanè, "Enhanced Optical Emission from 2D InSe Bent onto Si Pillars", *Advanced Optical Materials*, **18**, 2000828 (2020).

3. Z. R. Kudrynskyi, J. Kerfoot, D. Mazumder, M. T. Greenaway, E. E. Vdovin, O. Makarovsky, Z. D. Kovalyuk, L. Eaves, P. H. Beton and A. Patanè, "Resonant tunnelling into the two-dimensional subbands of InSe layers", *Nature Communications Physics*, **1**, 16 (2020).

4. M. A. Bhuiyan, Z. R. Kudrynskyi, D. Mazumder, J. D. G. Greener, O. Makarovsky, C. J. Mellor, E. E. Vdovin, B. A. Piot, I. I. Lobanova, Z. D. Kovalyuk, M. Nazarova, A. Mishchenko, K. S. Novoselov, Y. Cao, L. Eaves, G. Yusa and A. Patanè, "Photoquantum Hall effect and light-induced charge transfer at the interface of graphene/InSe heterostructures", *Advanced Functional Materials*, **29**, 1805491 (2019).

Physical constants

Quantity	Symbol	Value	Unit
Boltzmann constant	k_B	1.3807×10^{-23}	JK^{-1}
Electron charge	e	1.6022×10^{-19}	C
Electron mass in vacuum	m_e	9.1094×10^{-31}	kg
Permittivity in vacuum	ε_o	8.8542×10^{-12}	Fm^{-1}
Planck constant	h	6.6261×10^{-34}	Js
Reduced Planck constant	$\hbar$	1.0546×10^{-34}	Js
Speed of light in vacuum	c	2.9979×10^{8}	ms^{-1}

List of Contents

Chapter 1

Introduction

An ever-increasing challenge to beat Moore's law[1] has led to the development of sub-nanoscale devices for next-generation computers, spintronics, ultrafast quantum optics, quantum detection and beyond.[2-4] Material properties are influenced by their size and dimensionality. To date, traditional three-dimensional (3D) semiconductors based on silicon (Si) and germanium (Ge) have been widely used. However, as their size is reduced, they tend to suffer from severe short channel effects,[5] as the electrons cannot travel through sub-nanometer channels due to surface imperfections leading to an enhanced carrier scattering.[6] Furthermore, they face major technical challenges due to crystal lattice mismatch, compatibility with substrates, performance at high temperatures, lack of suitable oxide at the nanoscale[7] *etc.* It is envisaged that low dimensional structures yield better and efficient devices. Quantum wells or heterostructures made of ultrathin semiconductor layers with confinement in one direction, for example, gallium arsenide (GaAs) sandwiched between aluminium gallium arsenide (AlGaAs) *etc.* were the first examples of two-dimensional (2D) structures. However, semiconductor quantum wells are constrained by lattice matching and the thickness variations lead to degradation in device performance.[8]

On the other hand, since the successful isolation of graphene,[9,10] a new class of 2D materials have been intensively studied. These materials have a layered crystal structure with strong in-plane covalent bonds within each layer and weak van der Waals (vdW) forces between the layers. This booming family

of atomically thin vdW materials can compensate for the drawbacks of Si-electronics owing to their diverse range (from conductors to semiconductors to insulators) and distinct set of properties that have the potential to revolutionize electronics and optoelectronics.[11] Unlike conventional 2D quantum wells, these materials can be scaled down to single layers and stacked arbitrarily, unconstraint by lattice matching criteria, thus offering several degrees of freedom in the realization of multi-layered structures.

Graphene, the first member of the family, is a single layer (SL) of carbon atoms arranged in a honeycomb lattice. It has attracted tremendous interest for its exceptional properties, such as linear energy dispersions, exceptionally high carrier mobility (up to 10^5 $cm^2V^{-1}s^{-1}$ at room temperature (RT)), mechanical flexibility (Young's modulus of 1 TPa and intrinsic strength of 130 GPa)[12], impermeability to gases,[13] ability to be readily chemically functionalized[14].[15] However, its gapless nature[16] has restricted its extensive use in optoelectronics, which is primarily governed by the band gap, hence prompting a rigorous study of semiconducting 2D layers, such as transition metal dichalcogenides (TMDCs) (e.g. MoS_2, WSe_2 *etc.*),[17,18] III-VI chalcogenides (e.g. InSe, GaSe *etc.*),[19,20] wide-band gap hexagonal boron nitride (hBN),[21,22] and the narrow band gap black phosphorus (BP).[23,24] More recently, topological insulators ($MoTe_2$, Bi *etc.*) and even superconductors (FeSe, $RbSe_2$ *etc.*) have been explored.[25] These materials offer a wide tunability of their band gap with layer thickness due to quantum confinement. This band gap tunability is generally associated with direct to indirect band gap transitions[26,27] and intralayer coupling.[28,29] Moreover, due to their high surface-to-volume ratio, their electronic band structures are extremely sensitive to external perturbations such as electric fields, strain, chemical doping,

etc. allowing a smooth variation of their electronic band structure.[30] Some of these materials possess excellent transport properties and mechanical flexibility, making them well suited for optoelectronic applications.[11]

Amongst them, post-transitional III-VI metal chalcogenide indium selenide (InSe) is drawing increasing attention. InSe has a direct band gap in its bulk form[26], which is highly tunable (from near-infrared NIR to near ultra-violet UV) by the layer thickness,[31,32] it has light electron effective masses, leading to high electron mobility;[33] it is mechanically robust;[34] it has broadband absorption,[35] and exhibits high chemical stability due to surfaces that are free from dangling bonds.[36,37] These fascinating features make InSe extremely versatile in the field of electronics and optoelectronics. More recently, the optical anisotropy of its band structure has been studied and exploited: the exciton transitions between the uppermost valence band and the lowermost conduction band are direct and their intensity depends on the polarization of light.[38-41] Adding to the extensive research on this wonder material, my thesis exploits the inherent optoelectronic properties of 2D InSe and demonstrates its potential for technologies by the fabrication and investigation of InSe-graphene van der Waals heterostructures.

1.1. Thesis overview

The thesis is structured as follows:

Chapter 2 provides a literature review on the family of 2D materials, focussing on InSe, graphene and hBN, highlighting their uniqueness and the key findings of recent investigations.

Chapter 3 describes the fundamental physical principles of light-matter interaction and resonant tunnelling in 2D materials, particularly relevant to the work presented in this thesis.

Chapter 4 discusses the sample preparation and an overview of the different experimental techniques used in this thesis.

Chapter 5 reports on the controlled modulation of optical signals by exploiting the inherent optical anisotropy and mechanical flexibility of atomically thin 2D InSe.

Chapter 6 presents an investigation on a novel type of tunnel field-effect transistor (TFET) based on 2D InSe sandwiched between two multi-layered graphene (MLG) electrodes. This TFET exhibits multiple regions of negative differential conductance (NDC) peaks in the current-voltage characteristics.

Chapter 7 discusses the potential of InSe-graphene heterostructures as UV detectors. Optical absorption studies on bulk InSe by variable angle spectroscopic ellipsometry (VASE) are also presented.

Chapter 8 investigates an InSe-graphene planar phototransistor that exploits the electronic properties of InSe, hBN and graphene. The mechanism for photosensing, based on a light-induced charge transfer at the interface of InSe and graphene, is also discussed.

Chapter 9 presents a summary of the main results of this PhD work and considers future investigations for further developments.

Chapter 2

Two-dimensional (2D) van der Waals (vdW) crystals

This chapter reviews the literature on the investigations into physical properties of vdW crystals, focussing on InSe, graphene and hBN, which are the materials primarily featured in this thesis. The following section illustrates their specific properties suitable for the development of nanoscale optoelectronic devices. Other 2D materials, like TMDCs, are discussed briefly for a comparison with InSe. However, a detailed study of their properties is beyond the scope of this thesis.

2.1. InSe

Amongst vdW crystals, the III-VI metal chalcogenide InSe compound represents an exciting semiconductor that expands the current library of vdW crystals. This crystal possesses strong in-plane covalent bonds and out of plane weak vdW bonds. However, it features a variety of polytypes,[42-44] for example, $\alpha, \beta, \gamma, \varepsilon$ *etc.*, which depend upon the sequence of layers. The studies herein focus on γ-InSe, whose structure is discussed below.

Figure 2.1 shows the crystal structure of γ-InSe. Each layer consists of Se and In atoms, covalently bonded with the sequence Se-In-In-Se. The primitive unit cell has a lattice constant c = 2.496 nm along the c-axis. In the ab plane, the atoms form hexagons with lattice parameter $a = b$ = 0.400 nm.[45] The primitive unit cell consists of three layers, each with a thickness of t = 0.83 nm.[45] The non-metallic Se atoms form the surface of the exfoliated InSe nanoflakes and hinder oxidation, providing high chemical stability under ambient conditions.[46-48]

However, the presence of Se-vacancies can induce oxidation of the layers in air, influencing optical and electronic properties.[33,49] Thus, an encapsulation by hBN or alumina films is commonly used to preserve optoelectronic properties of InSe films for several weeks or even months.[50,51]

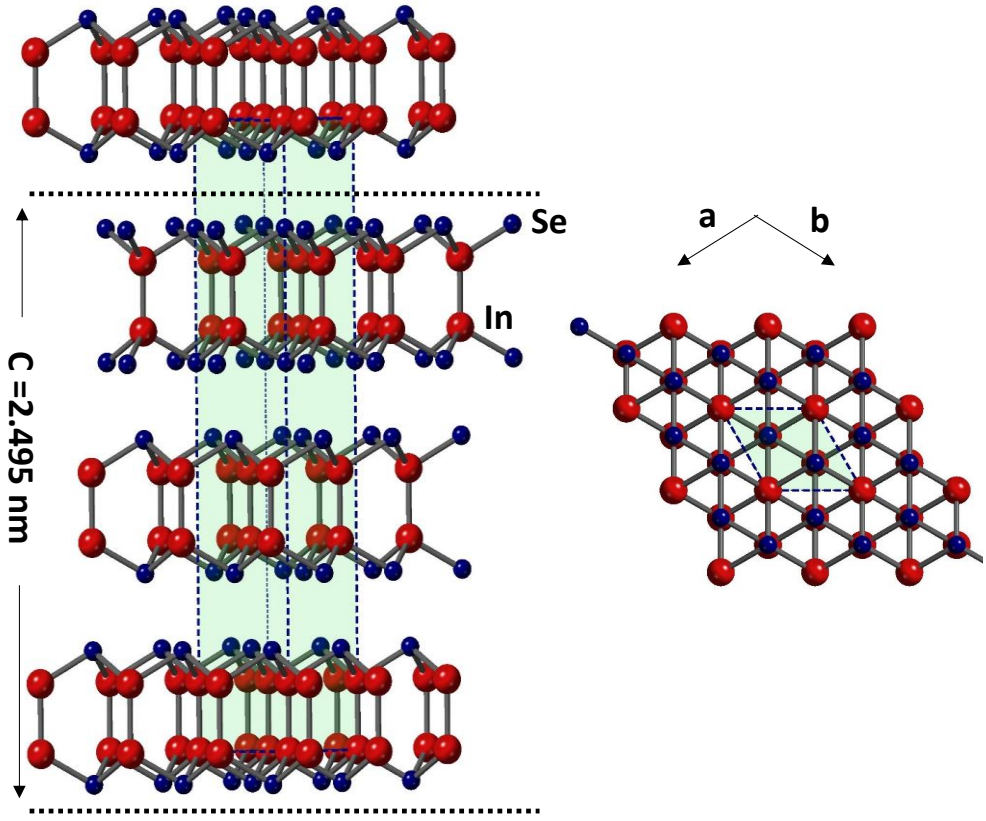

Figure 2.1. Crystal structure of γ-InSe along the *c*-axis and in the *ab*-plane.

The electronic band structure of InSe can be calculated by Density Functional Theory (DFT). **Figure 2.2a** shows the DFT calculated electronic band structure of InSe for 1, 5 and 10 layers. InSe undergoes a direct-to-indirect band gap crossover as the number of layers is reduced to ~ 10 layers.[26] It can be seen that when the thickness *t* is reduced, the conduction band minimum (CBM) remains at the Γ-point and shifts to high energy; in contrast, the valence band maximum (VBM) moves away from Γ towards the K-points, and the VB takes

the form of an inverted "Mexican hat" (Figure 2.2a).[26] With decreasing *t*, the energy interval ΔE between the valence band edge at Γ and the VBM increases from 0 to ~ 70 meV; correspondingly, the VBM shifts from Γ to about 30% of the Γ-K wave-vector.[26]

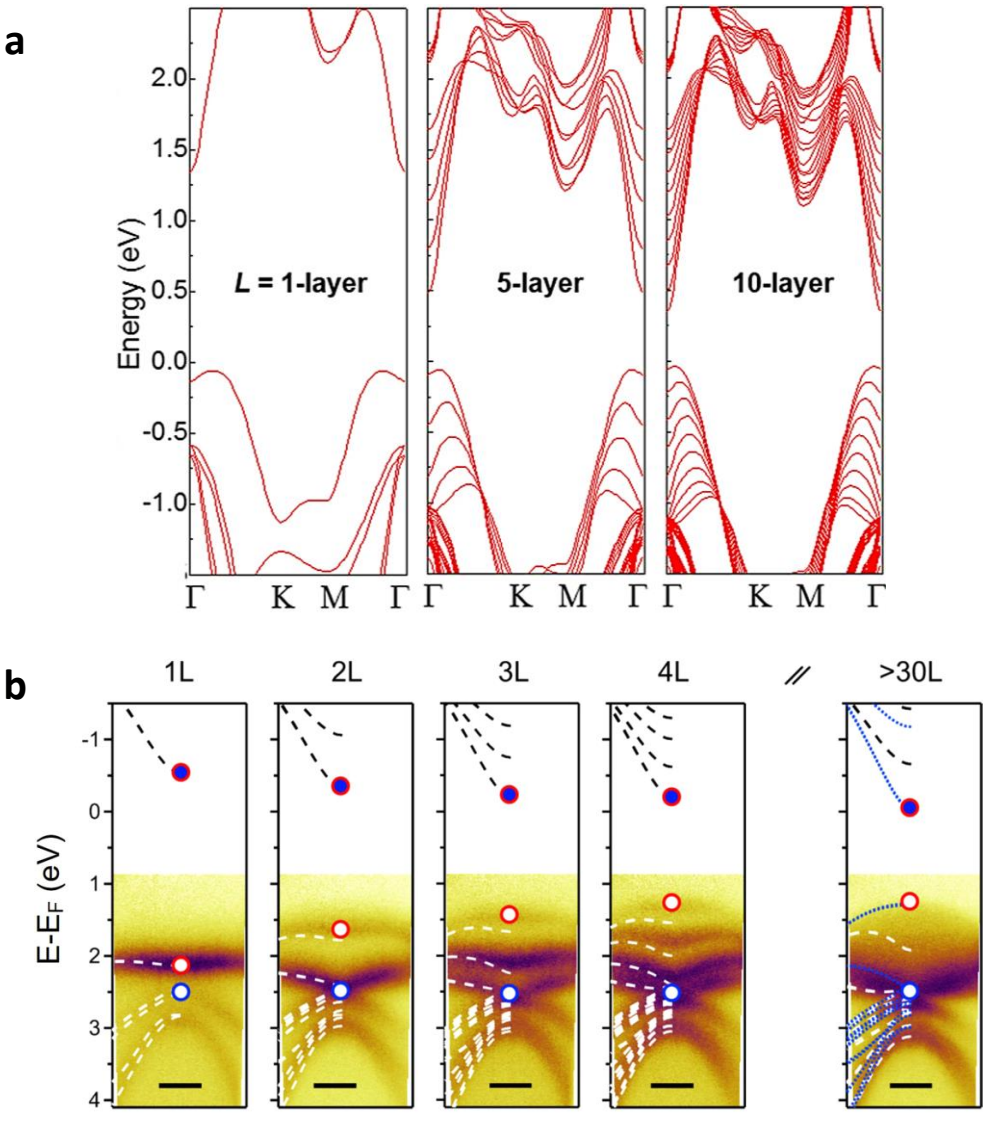

Figure 2.2. (a) DFT calculated band structure of InSe for 1, 5 and 10 layers. **(b)** The evolution of valence bands as the InSe thickness changes. Figures are reproduced from Ref. [26] and [52].

More recently, Hamer *et al.* measured the band structure (filled states) of monolayer and few-layer InSe by angle-resolved photoemission spectroscopy

with a submicrometer spatial resolution (μARPES). This has shown the evolution of the sub-valence bands with the increasing InSe layer thickness due to spin-orbit coupling (SOC) (**Figure 2.2b**).[52] Two interband transitions near the Γ-point in the Brillouin zone are predicted and observed: transition A involves the VBM (predominately consists of Se-p_z orbital) and the CBM (consists of In-*s* orbital); transition B involves a deeper valence band (Se- p_{xy} orbital).[52]

The optical band gap of InSe can be probed experimentally by photoluminescence (PL) spectroscopy.[31,33] Bulk InSe has a direct band gap of E_g = 1.26 eV at *T* = 300 K with the exciton binding energy E_b estimated to be ~ 14 meV. [26] The band gap is strongly dependent on the layer numbers. As shown in **Figure 2.3**, the band gap undergoes a strong blue shift up to ~ 2 eV[33] as the number of layers decreases due to the strong quantum confinement of electrons along the *c*-axis. Moreover, this increase in band gap with decreasing layer thickness is in agreement with a simple 2D quantum well model. Within this model, carriers are confined in a quantum well of thickness *t*. The band-to-band direct edge transition energy E_{2D} is given by

$$E_{2D} = E_g - E_b + \frac{n^2\hbar^2\pi^2}{2m^*t^2}\,, \tag{2.1}$$

where *n* is a positive integer, $\hbar$ is the reduced Planck constant, E_b is the exciton binding energy and m^* is the reduced effective mass of the carriers, defined as $m^* = \frac{1}{m_e} + \frac{1}{m_h}$, where m_e and m_h is the effective mass of electrons and holes. Moreover, carriers have anisotropic effective masses, which are relatively small: m_e= 0.08m_0 and m_h = 0.14m_0 along the *c*-axis and m_e= 0.13m_0 and m_h = 0.73m_0 along the in the plane of γ-InSe.[53] The intensity of the PL emission peak

decreases with decreasing layer thickness. Figure 2.2a (inset) shows the PL peak energy for the two interband transitions A and B near the Γ-point in the Brillouin zone for different InSe layer thicknesses.

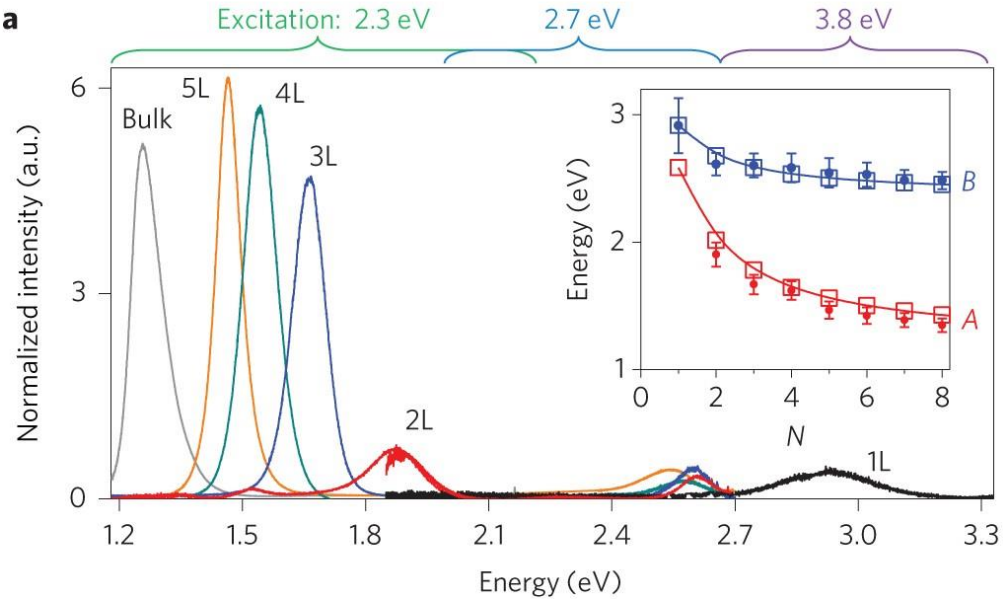

Figure 2.3. Typical μPL spectra of InSe layers at T = 300 K with peak energy strongly dependent on the layer thickness t, **Inset**: PL energy for different layer thickness for transition A and B. Figure is reproduced from Ref. [33].

InSe has been used in field-effect transistors (FETs): it provides an active conductivity channel in Si/SiO_2/InSe FETs with high room-temperature electron mobility (μ = 0.2 $m^2V^{-1}s^{-1}$), making it one of 2D vdW materials with the highest electron mobility.[33] Moreover, it has been recently found that its band gap is affected by strain,[54-56] opening a new avenue towards flexible electronics for sensing,[48] photon sources,[57] bendable photodetectors[58] *etc*. InSe is also widely used as a building block in several vdW heterostructures, leading to many interesting properties. Photodetectors with an active channel of a few layers of InSe show a broadband response from the visible to the near-infrared range (450–785 nm).[35,58] Remarkably, the bending of InSe-based devices fabricated on

a flexible polyethylene terephthalate (PET) substrate does not significantly reduce their performances,[58] which remain the most efficient amongst those realised with two-dimensional materials, including graphene and transition-metal dichalcogenides.[59] Other applications include *p*-InSe/*n*-InSe and *p*-GaSe/*n*-InSe junctions for room temperature electroluminescence.[48] Similarly, InSe/In_2O_3 may be purposely formed by photo- or thermal-annealing of InSe forming an oxide layer and subsequent heterostructure.[36] Such oxidation reduces the InSe thickness, which can be exploited to induce confinement effects.[36] A "giant" quantum hall (QH) plateau has been reported for graphene/InSe heterostructures, which is caused by the magnetic field and electric field effect-induced transfer of charge carriers between InSe and the adjacent graphene layer.[60] A light-induced sign reversal of the QH voltage and the persistence of the $h/2e^2$ QH plateau up to $T \sim 200$K was also reported.[61]

In summary, the science and technology of 2D InSe represent a rapidly developing and vibrant field with breakthroughs emerging from both experiment and theory, making InSe a promising 2D material for the next generation of functional semiconducting devices.

2.2. Graphene

As the first member of this large family of 2D vdW materials, graphene has attracted enormous attention owing to its remarkable properties, since its discovery by Professor Sir Andre Geim and Professor Sir Kostya Novoselov in 2004, leading to a Nobel Prize in Physics.[62] Graphene consists of a single atomic layer of covalently bonded carbon atoms arranged in a honeycomb lattice: each carbon atom forms strong σ-bonds with three nearest atoms by sp^2 hybridisation;

the remaining out of plane non hybridised electronic orbital (p_z) of each carbon atom forms a π-bond. **Figure 2.4** shows the crystal structure and the Brillouin zone of graphene. The unit vectors in real space for graphene are:

$$\overrightarrow{a_1} = \left(\frac{\sqrt{3}}{2}a, \frac{a}{2}\right), \overrightarrow{a_2} = \left(\frac{\sqrt{3}}{2}a, -\frac{a}{2}\right) \tag{2.2}$$

and the corresponding unit vectors of the reciprocal lattice are:

$$\overrightarrow{b_1} = \left(\frac{2\pi}{\sqrt{3}a}, \frac{2\pi}{a}\right), \overrightarrow{b_2} = \left(\frac{2\pi}{\sqrt{3}a}, -\frac{2\pi}{a}\right). \tag{2.3}$$

The corners of the graphene Brillouin zone, *K* and *K'*, are named as Dirac points. At these points, the conduction band and the valence band meet. Due to this crystal structure, charge carriers in graphene are described by a Dirac-like spectrum rather than the usual Schrödinger equation for nonrelativistic quantum particles.[63] The lattice of graphene consists of two equivalent carbon sublattices A and B. Three of their nearest neighbour atoms are distanced by δ_1, δ_2 and δ_3, as shown in Figure 2.4.

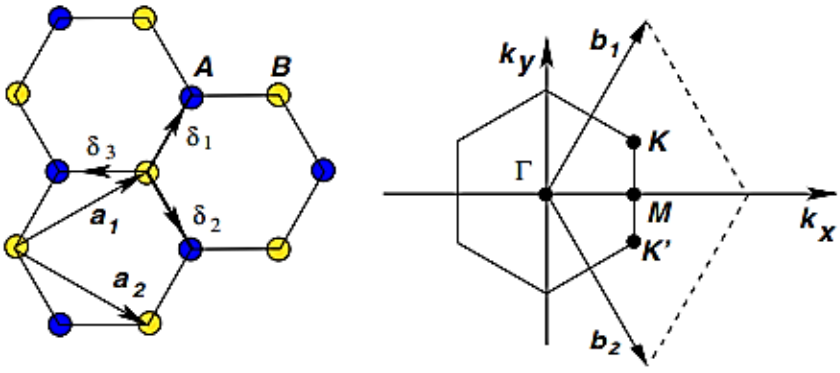

Figure 2.4. The crystal structure and Brillouin zone of graphene. Figure is reproduced from Ref. [16].

Considering that the electrons can hop to the nearest atoms, the tight-binding Hamiltonian for electrons of graphene predicts that the energy dispersion about the Dirac points can be approximated by the linear function:

$$E(q) = \pm v_F|q|, \tag{2.4}$$

where q is the electron momentum relative to the Dirac point and $v_F \sim 10^6$ ms^{-1} is the Fermi velocity. Due to the linear energy dispersion around the Dirac points, the quasiparticles of graphene are called massless Dirac fermions. This unique band structure of graphene leads to many exceptional properties such as ambipolar conduction,[9] charge carrier tunability,[64] high carrier mobility[65] *etc.* Based on the 2D nature of graphene and its linear energy dispersion, the density of states (DOS) can be expressed as

$$D(E) = \frac{2E}{\pi v_F^2 \hbar^2} \tag{2.5}$$

and the carrier density in graphene at T = 0 K can be expressed as

$$n(E_F) = \frac{E_F^2}{\pi v_F^2 \hbar^2}\,. \tag{2.6}$$

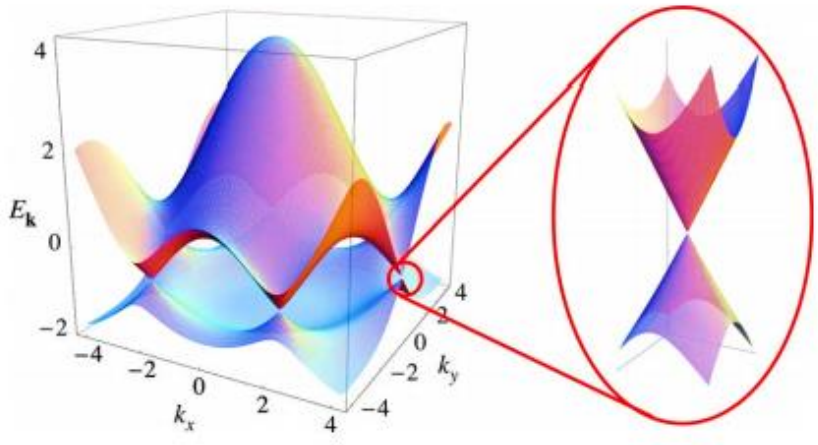

Figure 2.5. Electronic dispersion in the honeycomb lattice and zoom in of the energy bands close to Dirac points. Figure is reproduced from Ref. [16].

For graphene on a SiO_2/Si substrate, the carrier density can be tuned by electrostatic gating as

$$dn = \frac{\varepsilon_0 \varepsilon}{de} dV_{g,} \tag{2.7}$$

where ε_0 and ε are the permittivity in free space and relative permittivity of the SiO_2 layer, respectively, d is the thickness of the oxide layer and V_g is the applied gate voltage on the Si substrate. Depending on the applied gate voltage (V_g), the Fermi level also moves up or down through the Dirac point according to $E_F = \pm\hbar v_F \sqrt{\pi n}$. As the density of charge carriers changes with V_g, the resistance also changes with a maximum value at a particular gate voltage at which the Fermi level aligns with the Dirac point, as shown in **Figure 2.6**.

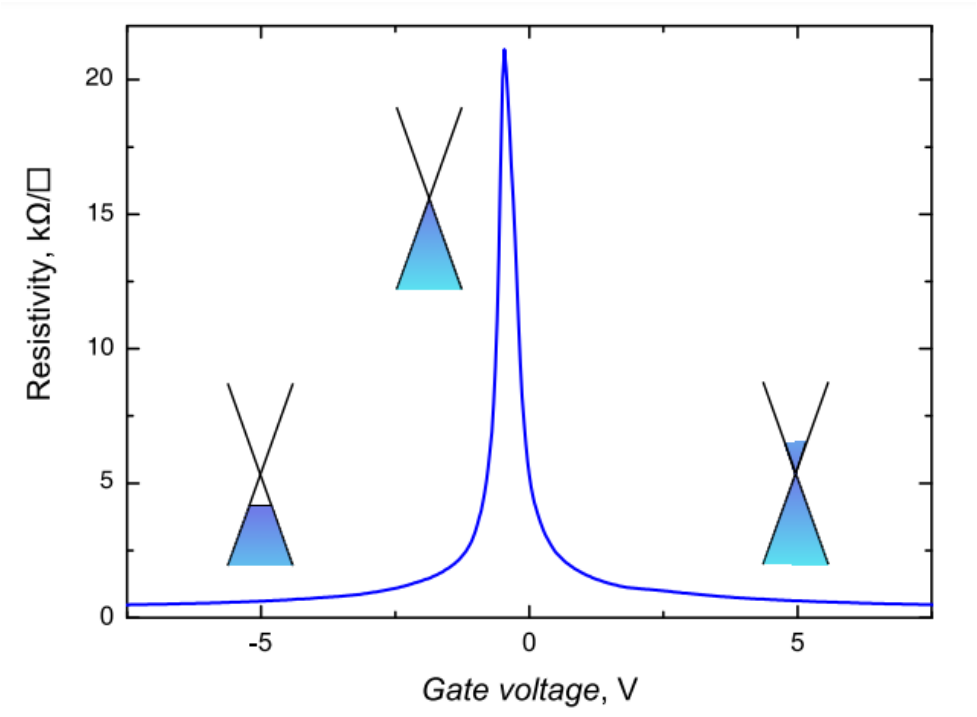

Figure 2.6. The resistivity of graphene as a function of gate voltage. Figure reproduced from Ref. [66].

The mobility is defined as $\mu = {}^{1}/_{en\rho}$, where ρ is the resistivity. The encapsulation of exfoliated graphene by hBN on hBN/SiO_2 substrate has enabled mobilities of up to 1×10^6 cm^2/Vs at T = 1.7 K.

Being a zero-band gap semi-metal with a finite density of states (DOS) and an exceptionally high thermal conductivity,[67] high mechanical robustness (Young's modulus ~ 1 TPa),[68] graphene offers partial optical[13] and electrostatic transparency with a tunable work function,[16] making it an ideal building block for vdW heterostructures.

2.3. hBN

2D hBN commonly known as white graphene is an isomorph of graphene with a minimal lattice mismatch (-1.8%).[69] 2D-hBN nanosheets, arranged in a hexagonal lattice by alternating boron and nitrogen atoms, behave as an insulator with an extremely large band gap ~ 5.97 eV in bulk.[69,70] **Figure 2.7a** shows the crystal structure of hBN with lattice parameters of a = 2.5 Å and c = 6.6 Å with an interlayer spacing of 3.3 Å.[71] The band structure of hBN exhibits an indirect to direct band gap crossover in the monolayer limit, complementary to that of InSe[26] and similar to that of TMDCs, such as molybdenum disulphide (MoS_2).[27] **Figure 2.7b** shows the current-voltage curve demonstrating its excellent insulating property. Due to their unique structure and excellent properties such as mechanical robustness,[72] low density of dangling bonds,[73] high thermal conductivity,[70] electrical insulation,[74] oxidation resistance[75] *etc.*, hBN has drawn immense surge of interest, especially as a substrate as it lowers electron-hole charge fluctuations as compared to those on SiO_2, leading to improved device performances. In graphene electronics, it has been used as a gate dielectric (as

shown by **Figure 2.7c**, resistivity–gate voltage (V_g) curves of monolayer graphene on hBN measured at different temperatures)[76] and tunnelling barrier[77] in nanocapacitors[78] and resistive memory switching devices.[79] Moreover, hBN is widely explored for UV laser devices.[80]

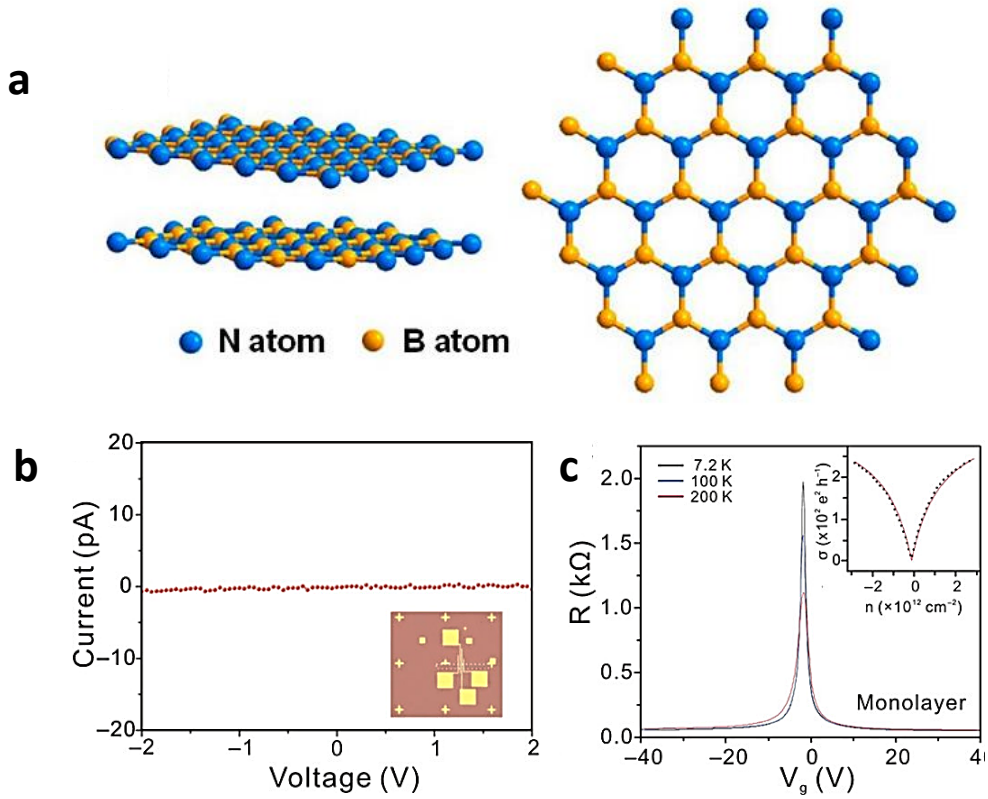

Figure 2.7. (a) The crystal structure of monolayer hBN. **(b)** The current voltage curve shows its excellent insulating property. **(c)** Resistivity–gate voltage (V_g) curves of monolayer graphene on hBN measured at different temperatures. The inset shows the corresponding conductivity–carrier density curve. Figures reproduced from Ref. [81-83].

2.4. Other 2D materials

Apart from the materials discussed above, 2D TMDCs also exhibit extraordinary electronic, optical and mechanical properties that have been extensively studied in recent years.[84,85] Owing to their versatile crystal structures, TMDCs can behave as insulators, semiconductors, and superconductors. In

general, bulk TMDCs exhibit an indirect band gap. However, the band gap becomes direct when they are thinned from bulk to monolayer.[27] The ability to control the electrical properties of TMDCs, such as the carrier density, is crucial in modern electronics. For example, MoS_2 has been realised as a stable *p*-type semiconductor by Nb doping.[86] Moreover, the thin layer thickness of the TMDCs allows efficient electrostatic doping by the gate voltage. This can also improve mobility, reduced contact resistance and enhance the photoresponsivity.[87,88]

Chapter 3

Light-matter interaction and quantum tunnelling in 2D materials

The optical properties of a semiconductor are linked to interband and intraband optical transitions, whereas the electrical transport properties rely on the intraband kinetics of electrons and/or holes depending on the free carriers in the semiconductor. This chapter discusses the fundamental concepts of light-matter interactions and quantum tunnelling in 2D materials that underpin the research presented in this thesis.

3.1. Density of states and exciton physics in 2D semiconductors

An important property of a semiconductor is the density of states (DOS), defined as the number of states available at a given energy, $D(E)$, per unit energy per unit volume. As the free movement of the carriers is restricted by spatial dimensions, $D(E)$ is significantly different for bulk (3D), quantum wells (2D), quantum wires (1D) and quantum dots (0D), as illustrated in **Figure 3.1** for a semiconductor with a parabolic energy dispersion. Specifically, for a 2D semiconductor with a band gap E_g, the electrons and holes are confined in one direction (therefore they have only two degrees of freedom) and the conduction and valence bands can often be described by simple parabolic energy dispersions, leading to an expression for $D(E)$ that does not depend on energy. The quantization of the energy levels in 2D also produces a series of steps in the DOS versus energy, which influence optical properties, such as absorption and emission, and electronic transport. However, the simple picture illustrated in

Figure 3.1 does not take into account several important phenomena, such as the non-parabolicity of the energy dispersions (*e.g.* graphene in which the energy dispersion is linear near the Dirac point) and electron-hole correlations, such as excitons.

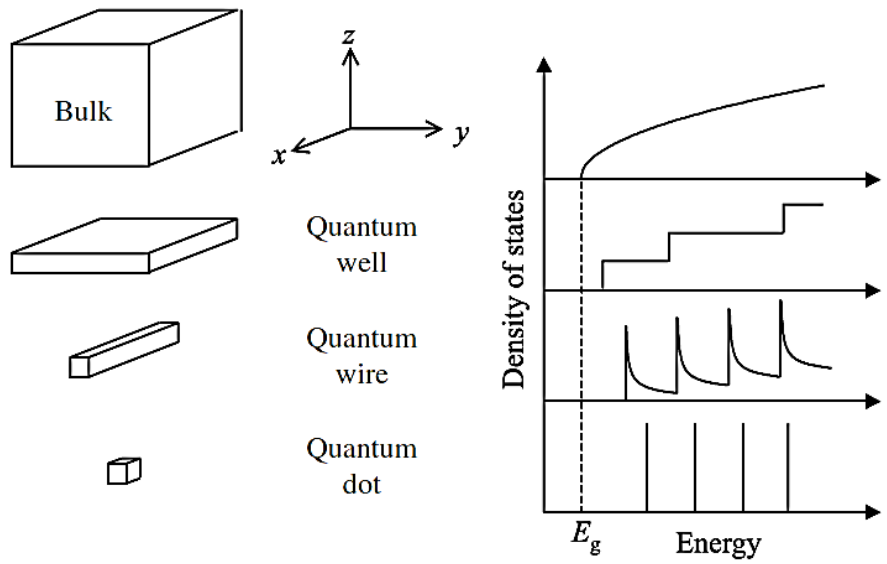

Figure 3.1. Schematic representation of bulk (3D), quantum well (2D), quantum wire (1D) and quantum dot (0D). Electronic density of states versus energy for a semiconductor with a bandgap E_g and a parabolic energy dispersion in 3D, 2D, 1D and 0D cases. Figure adapted from Ref[89].

Here, we focus on excitons. Excitons are Coulomb-bound states of electron-hole pairs, which can be formed when light excites one electron into the conduction band, leaving behind a hole in the valence band. These electrically neutral quasiparticles have a binding energy E_B that depends on several factors, such as the dielectric environment, quantum confinement and effective mass of the carriers. Optical processes, such as emission and absorption are often dominated by excitons due to their large oscillator strength and enhanced light-matter interactions.[90] Within a crystalline material excitons can exist in two

different forms: Wannier-Mott excitons [91] and Frenkel excitons [92]. In contrast to Frenkel excitons, for Wannier-Mott excitons, the average separation between electron and holes is much greater than the atomic spacing. This applies to the excitons in 2D semiconductors considered in this work.[93,94]

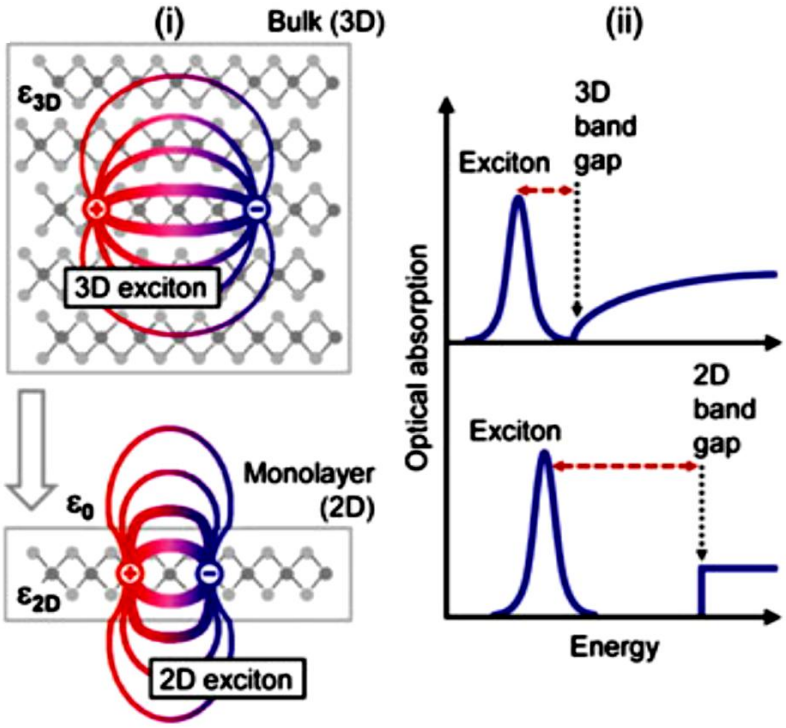

Figure 3.2 Schematic showing the field lines and band diagram for an electron-hole pair in 3D and 2D systems. Figure adapted from Ref.[94].

Since excitons exist in a dielectric medium, Coulomb interactions between charges are screened. The electrons and holes in a 2D material are confined strongly in the *z*-direction (perpendicular to the plane). **Figure 3.2** is a schematic showing the field lines and DOS for electron-hole pairs in 3D and 2D systems. Due to the strong confinement, the effective separation between the electrons and holes decreases, lowering the dielectric screening compared to 3D. In a 2D system, due to the enhanced Coulomb interaction, the quasiparticle energy bandgap and the exciton binding energy increase. For 2D materials based on

free-standing transition metal dichalcogenides (TMDCs) layers, the binding energy of the exciton is approximately 0.5 eV.[94] However, for metal chalcogenides (MCs), the binding energy is much smaller, approximately 14.5 meV for InSe.[95,96]

In 2D materials based on TMDCs, the spin-orbit coupling (SOC) leads to the formation of the so-called A and B excitons. Their energy splitting arises mainly from the valence band.[97] Taking into account the valence band splitting, A and B excitons arise from optical transitions from the upper valence band and deeper valence band to the conduction band, respectively. The energy of the A exciton state is approximately 100-200 meV lower than the high energy B exciton state, which possesses a shorter lifetime.[97] However, MCs, such as InSe, exhibit a different behaviour compared to TMDCs.[39,98] For InSe, SOC effects tend to be weaker: in the absence of SOC, the wave functions for the highest valence band states consist mainly of Se-p_z orbitals whereas the deeper valence band states consist of Se p_{xy} orbitals; the lowest conduction band states are instead dominated by In-*s* orbitals.[99] Due to mirror symmetry, for monolayer InSe, the bandgap transition (transition-A) is forbidden for light polarized in the layer plane and allowed for out-of-plane polarized light. The transition-B, involving the deeper valence band, behaves oppositely.[33] These selection rules apply also to few-layer and bulk InSe, although the mirror symmetry is broken due to the ABC stacking of the individual layers.[28,99] A weak emission from the in-plane dipole is observed due to the mixing between the Se-p_z and Se p_{xy} orbitals valence band when SOC interactions are taken into consideration.[99]

Excitons can be classified as bright and dark. If the electron and hole have the same momentum, they can recombine by emitting a photon. These excitons

are called bright excitons. In contrast, for electrons and holes with a different momentum, excitons cannot easily recombine via direct emission of a photon due to the lack of required spin-momentum conservation. These excitons are called dark excitons. Dark excitons have relatively long radiative lifetimes (~μs) compared to bright excitons. Recently, ultrafast energy transfer of bright and dark excitons in 2D vdW heterostructures was reported.[100] Also, light emission can be induced from dark excitons in the monolayer WSe_2 by controlling spin and valley selectively.[101]

Apart from these intralayer excitons mentioned above, interlayer excitons can form in vdW heterostructures where electrons and holes reside in two adjacent layers. Interlayer excitons can be strongly bound (> 100 meV) and long-lived, with a radiative lifetimes longer than for intralayer excitons.[102,103]

Excitons are often described using a simple hydrogenic model. The excitonic Rydberg energy R_X can be defined as

$$R_X = R_H \frac{m^*}{m_0} \frac{1}{\varepsilon^2}, \tag{3.1}$$

where R_H is the hydrogenic Rydberg constant (13.6 eV), ε is the dielectric constant of the medium, and m^* and m_0 are the reduced and rest mass, respectively. Here m^* is defined as $\frac{1}{m^*} = \frac{1}{m_e} + \frac{1}{m_h}$, where m_e and m_h are the effective masses for electrons and holes, respectively. These excitons are more prominent for semiconductors with a bandgap energy of E_g ~1-3 eV and light carrier effective masses.[89] The total energy of an exciton propagating with wave vector *k* is given by:

$$E_X^n(k) = E_g - R_X \frac{1}{n^2} + \frac{\hbar^2 k^2}{2m^*}\,, \tag{3.2}$$

where *n* is the principal quantum number required to characterize the excitonic bound states. The Bohr radius for the first excited level of the exciton (a_X) is related to the Bohr radius of the hydrogen atom (a_H) as:

$$a_X = \frac{\varepsilon m_0}{m^*} a_H \quad . \tag{3.3}$$

Different experimental techniques allow the measurement of the excitonic binding energy. For example, previous studies have used scanning tunnelling spectroscopy to estimate the band gap energy E_g of $MoSe_2$ supported by monolayer graphene[104]. This was then combined with PL measurements of the exciton recombination energy E_X to determine the exciton binding energy (0.55 eV). For InSe, transmission spectroscopy studies were used to determine the exciton binding energy of bulk crystals (14.5 meV) in line with several magneto-optical experiments.[96,105] Reflectance contrast measurements on monolayer WS_2 on SiO_2 substrate estimated the exciton binding energy to be approximately 0.3 eV.[106] The exciton binding energy can be tuned by engineering the surrounding dielectric environment.[107,108] Furthermore, strain can be used as a tool to control the optical properties of 2D materials. Excitonic resonances significantly shift towards lower energies in the presence of tensile strain.[109,110] However, we note that this shift is due to a decrease of the electronic band gap, whereas the excitonic binding energy shows only slight changes.[111]

3.2. Optical absorption and emission

Here, we consider the interband absorption within the semiclassical framework used to describe light-matter interactions in solid-state systems.

Following the absorption of a photon, an electron is excited from its initial state. The optical absorption coefficient, $\alpha(E)$, is defined by the transition rate $W_{i\to f}$ for excitation of an electron from an initial quantum state ψ_i to the final quantum state ψ_f . According to Fermi's golden rule, the transition rate is given by

$$W_{i\to f} = \frac{2\pi}{\hbar}|M|^2 D(E)\,, \tag{3.4}$$

where M is the transition matrix element that describes light-matter interaction.

For direct bandgap semiconductors, the transitions involve no change in the electron wave vector (k), such that $k_f \approx k_i$. In contrast, for indirect bandgap semiconductors, optical transitions involve phonons to comply with the conservation of momentum. The absorption coefficient $\alpha(E)$ of a semiconductor with a bandgap energy E_g is expected to depend on energy according to the following relations:[89,112]

$$\begin{cases} \alpha\left(E < E_g\right) = 0 \\ \alpha\left(E \geq E_g\right) \propto \left(E - E_g\right)^{1/2} & \text{direct} \\ \alpha\left(E \geq E_g\right) \propto \left(E \pm \hbar\omega - E_g\right)^2 & \text{indirect} \end{cases} \tag{3.5}$$

where $\hbar\omega$ is the phonon energy. However, this simple description does not take into account important processes, such as [89] (i) the excitonic contribution, which notably enhances $\alpha(E)$ at low temperatures; (ii) the extrinsic absorption due to defect states and impurities, which induce additional resonances below E_g; and (iii) the non-parabolicity of the energy dispersions.

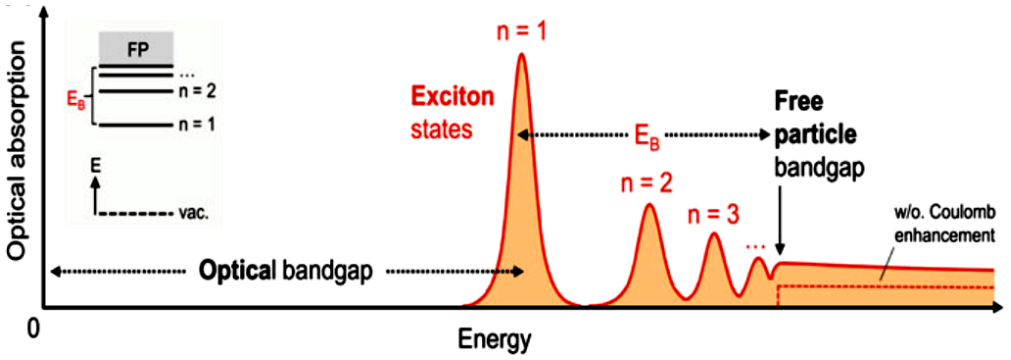

Figure 3.3. Absorption spectrum for excitons as a function of energy: the first absorption peak corresponds to the optical bandgap. n represents the excited excitonic states. Figure reproduced from Ref. [94].

Figure 3.3 illustrates the general absorption spectrum of a semiconductor with strong excitonic resonances. The electronic bandgap is defined as the energy it takes to create an unbound electron-hole pair in the continuum of states of the material. The optical bandgap however is defined as the electronic bandgap energy minus the exciton binding energy E_b. This is the most prominent peak in the absorption spectrum, which corresponds to the lowest excited state n = 1 of the exciton, as labelled in figure 3.3. Above the bandgap, resonances (critical points) appear at progressively higher energies (E_1, E_2…) corresponding to the excitonic excited states. A continuum occurs due to unbound electron-hole pairs above the band edge. The ratio of the absorption coefficients above the band edge with and without the Coulomb interaction is called the Sommerfeld factor or the Coulomb enhancement factor. In a 2D system, the band-to-band step absorption spectrum is multiplied by the 2D Sommerfeld factor which equals 2 at the gap edge and unity far above the gap.[113,114]

Following absorption, light is emitted when excited electrons in the conduction band recombine with holes in the valence bands. Upon electrical or optical excitation, the electron and holes rapidly relax to the bottom of their

respective bands before emitting photons by radiative recombination. In 2D systems, the emission peak is shifted towards higher energy compared to their bulk counterpart due to strong quantum confinement.[89] The electron-hole recombination from the lowest bound state can generate an optical emission band with spectral width limited by thermal broadening (~ k_BT) and extrinsic disorder effects.

Experimentally, the absorption coefficient $\alpha(E)$ of a sample is defined as the fraction of the power absorbed per unit length. If a beam is propagating along the *z*-direction through a thin film, the optical intensity $I(z)$ can be described by Beer's law as

$$I(z) = I_0 e^{-\alpha z} , \tag{3.6}$$

where I_0 is the optical intensity at $z = 0$. The optical intensity of a light wave is also proportional to the square of the electric field, which falls off exponentially with a decay constant $2\kappa\omega/c$,[89] where κ is the imaginary part of the complex refractive index ($N = \eta + i\kappa$). On comparing it to the Beers law (Eq 3.6), we derive

$$\alpha = \frac{2\kappa\omega}{c} = \frac{4\pi\kappa}{\lambda} , \tag{3.7}$$

where λ is the wavelength of the incident beam. In a reflection measurement, α is calculated from the imaginary part of the complex refractive index ($N = \eta + i\kappa$) as:

$$R = \frac{(\eta - 1)^2 + \kappa^2}{(\eta + 1)^2 + \kappa^2} , \tag{3.8}$$

where η and κ are the real and imaginary parts of the complex refractive index. The pseudo dielectric function ($\varepsilon = \varepsilon_1 + i\varepsilon_2$) is also related to η and κ by

$$\eta = \sqrt{\varepsilon_1} \tag{3.9}$$

$$\kappa = \frac{\varepsilon_2}{2n}. \tag{3.10}$$

Thus, η and κ are not independent variables and are related to each other by Kramers-Kronig relationships.[89] A refined version of the reflectivity measurement technique, namely ellipsometry, can be used. In this case, the sample is illuminated at an angle by linearly polarized light. The reflected light becomes elliptically polarized due to different reflectivity of the *s*- and *p*-polarizations. [115,116] It is possible to determine both η and κ from the ellipsometric reflectivity spectra and hence deduce $\alpha(E)$. This approach is described in Chapter 4.

3.3. Resonant tunnelling in 2D heterostructures

Tunnelling is a quantum-mechanical effect. Classically, a particle with kinetic energy E incident on a potential barrier of height V_0 is always reflected if $E < V_0$ and always transmitted for $E > V_0$. In quantum mechanics, an incident particle with $E < V_0$ has a finite probability of tunnelling throughout the barrier. The probability of tunnelling is known as the transmission coefficient $T(E)$. For an electron approaching a square potential barrier of height V_0 and width b, $T(E)$ is given by [117]

$$\begin{aligned} T(E) &= \left[1 + \frac{{V_0}^2}{4E(E-V_0)}\sin^2(kb)\right]^{-1} && E > V_0 \\ T(E) &= \left[1 + \frac{{V_0}^2}{4E(V_0-E)}\sinh^2(kb)\right]^{-1}, && E < V_0 \end{aligned} \tag{3.11}$$

where $k = \sqrt{|2m(E - V_0)|}/\hbar$. Thus, $T(E)$ depends on the energy of the electron and the width of the tunnelling barrier and decreases exponentially with increasing barrier width. Tunnelling has been exploited widely in quantum well structures based on III-V materials[118] and, more recently, using 2D materials.[105,119]

For 2D vertical heterostructures, two types of tunnelling phenomena have been studied: i) within the same (like) band i.e., conduction-to-conduction band or valence-to-valence band tunnelling, typically observed in symmetric field-effect transistors (symFET)[119-122] and ii) between different (unlike) bands, i.e., conduction-to-valence band tunnelling, explored in tunnel field-effect transistors (TFET)[123,124] and Esaki diodes.[125,126] More recently, resonant tunnelling has been explored in 2D vertical symFETs for its widespread potential applications, including multi-valued logic and communication systems.[119,127] In the following, our discussion focuses on interesting cases of tunnelling leading to negative differential conductance effects in the electrical transport[66,105] and relevant for the work presented in this thesis.

Resonant tunnelling is usually considered in systems where a confined region is isolated from electrodes by a tunnel barrier. For example, in a double barrier system, a resonant or quasi-bound state (*i.e.* spatial confinement of electrons) is formed inside a quantum well between two barriers for a finite period before the electrons can tunnel. This is similar to an optical Fabry-Perot etalon where wave-like particles are confined and partially reflected in a resonant cavity by mirrors. For energies near the resonance, $T(E)$ increases and has a Lorentzian shape centred on the first quantized electronic level in the quantum well E_1.[117] Thus, based on Eq 3.11,

$$T(E) = T(E_1)\left[1 + \left(\frac{E-E_1}{\Gamma/2}\right)^2\right]^{-1}, \quad (3.12)$$

where $\Gamma = \hbar v(T_1 + T_2)/2b$ is the width of the Lorentzian transmission curve. T_1 and T_2 are the transmission coefficients for the individual barriers. The peak transmission $T(E_1)$ is given by:

$$T(E_1) \sim \frac{4T_1T_2}{(T_1+T_2)^2} \ . \quad (3.13)$$

However, for a symmetric double-barrier system, $T(E) \sim T_1T_2$. This type of tunnelling will be described in Chapter 6 for a structure where a thin quantum well InSe layer is embedded between two graphene electrodes.

Another interesting example, of resonant tunnelling was reported by Britnell *et. al* on graphene/hBN/graphene heterostructures (**Figure 3.4a**)[105], where they exploited resonant tunnelling of Dirac fermions through a boron nitride barrier, sandwiched between two graphene electrodes. A resonant transmission of charge carriers occurs when the electronic spectra of the two electrodes are aligned. The resulting negative differential conductance in the device characteristics persists up to room temperature and is gate voltage-tuneable due to the graphene's unique Dirac-like spectrum (**Figure 3.4b**). Theoretical simulations based on the Bardeen transfer Hamiltonian approach have unveiled the effect of residual doping in the graphene electrodes on the device characteristics. Elastic scattering due to disorder or interaction effects leads to relaxation of the in-plane wave vector (***k***) conservation otherwise present in an idealized case in which the graphene electrodes are undoped and their crystal lattices are aligned. The scattering potential $V_s(q)$ dictates the Gaussian form of the resonant curve.[105]

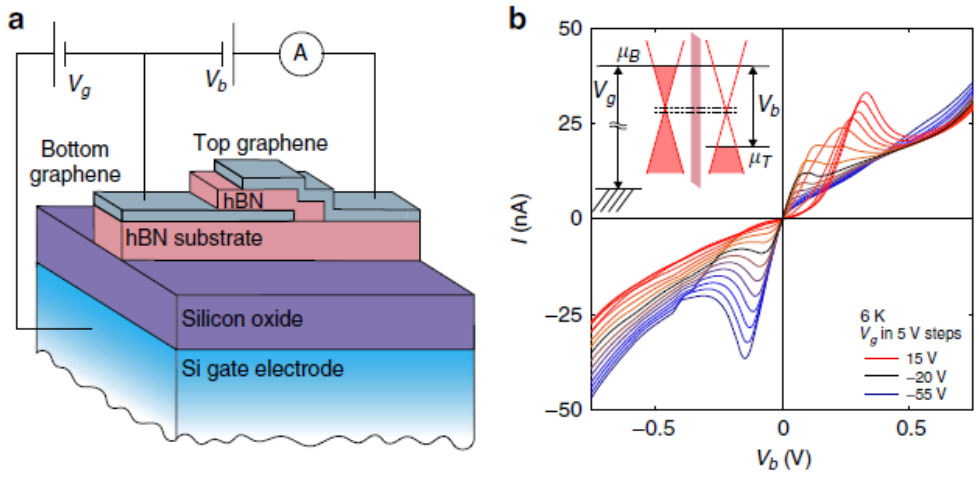

Figure 3.4.(a-b) Schematic diagram and measured current-voltage characteristics of graphene/hBN/graphene vertical heterostructure. For better understanding, the inset band diagram is plotted as energy vs real space positions, but the dispersion of electrons in graphene in k-space is shown as well on top of the real space dependence. Figure reproduced from Ref.[105].

As discussed in Chapter 6, our tunnel field-effect transistor (TFET) in which InSe acts as the tunnel barrier between two graphene electrodes exhibits multiple regions of negative differential conductance peaks in the current-voltage characteristics. In contrast to the work reported by Britnell *et. al.*,[105] our work exploits resonant tunnelling through a quantized 2D subband of the InSe layer when the energy of the subband minimum aligns with the chemical potential of the graphene-source electrode (detailed in Chapter 6).

Chapter 4

Experimental techniques

This chapter presents a description of the sample preparation and different experimental techniques used to investigate the structural, electronic and optical properties of nanosheets and heterostructures fabricated with 2D vdW materials.

4.1. Assembly of van der Waals heterostructures

2D layered materials can be assembled into a virtually infinite combination of vdW heterostructures owing to multiple degrees of freedom, *i.e*., the choice of materials, stacking order, and lateral orientation angle at the interfaces *etc*., making them more versatile than other conventional systems, for example, heterostructures based on covalent semiconductors. In this section, we review the fabrication technique of the vdW heterostructures used in the experiments presented in the thesis.

4.1.1. 2D vdW crystals and mechanical exfoliation

InSe nanoflakes used in the experiments were exfoliated from bulk γ-polytype InSe ingots grown by the Bridgman method[128] at the Institute for Problems of Material Science, Ukraine by Professor Z. D. Kovalyuk and Dr Z. R. Kudrynskyi. In this method, a nonstoichiometric melt of $In_{1.03}Se_{0.97}$ is sealed inside a quartz ampoule under a high vacuum. This ampoule is inserted into the Bridgman furnace and heated above the melting point of the polycrystalline powder to form a homogenous melt. The ampoule is slowly moved to the low-temperature region of the furnace to aid the crystallisation at the tip. After several

days of cooling, it forms an ingot (**Figure 4.1a**). The Bridgman growth of nominally undoped γ-InSe produces an *n*-doped material (electron concentration $n = 10^{15}$ cm^{-3} at $T = 300$ K) due to the presence of excess interstitial In throughout the crystal.[129]

2D graphene nanosheets were exfoliated from commercially available highly oriented pyrolitic graphite (HOPG) and natural graphite. The hBN crystals were provided by Prof. Kenji Watanabe and Prof. Takashi Taniguchi at the National Institute for Material Science in Tsukuba, Japan.[130]

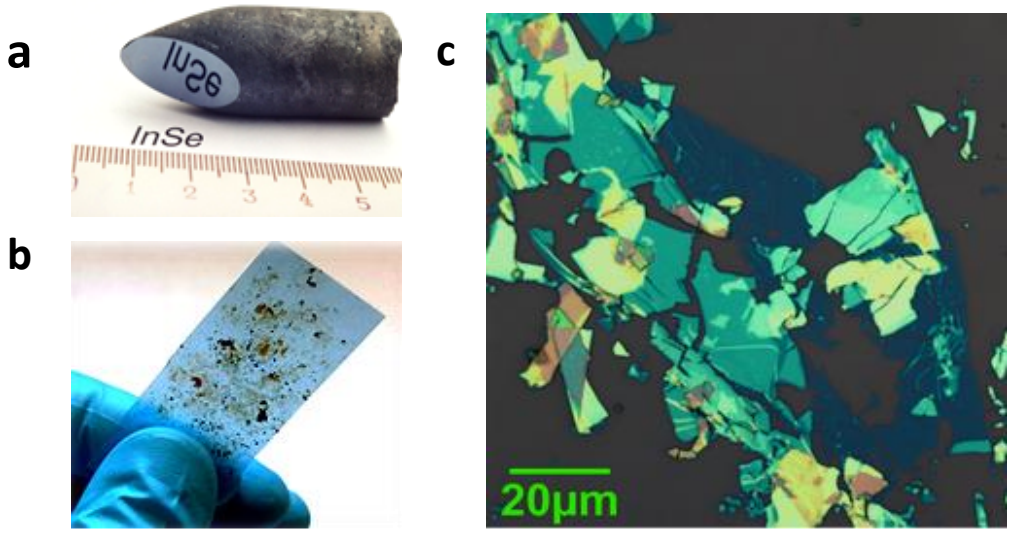

Figure 4.1. (a) Bulk Bridgman grown InSe ingot. **(b)** InSe flakes scattered on adhesive tape. **(c)** Exfoliated flakes of different thicknesses on a SiO_2/Si substrate with a 300 nm thick SiO_2 layer.

The InSe nanosheets were prepared from the Bridgman grown crystals by a mechanical exfoliation method.[131] This method relies on the difference between in-plane covalent and out-of-plane weaker van der Waals bonds, which facilitates the cleavage at the interface between two adjacent planes. In this method, we use a low residue, commercially available adhesive tape to peel the nanosheets directly from the crystal (**Figure 4.1b**). The tape is folded and

unfolded several times to reduce the thickness of the layers. These freshly cleaved nanosheets are transferred onto an intermediate viscoelastic polydimethylsiloxane (PDMS) polymer film (Gelfilm DGL film -50/17-X4 from Gelpak) attached on a glass slide or directly to a target substrate (*i.e.* 300 nm thick SiO_2 on Si wafers). The resultant flakes have a broad range of thicknesses ranging from 2 monolayers (~ 2 nm) to several hundred microns. Lateral dimensions of the flakes are in the range of 10^{-1} μm - 10^{2} μm depending on the thickness, with the thinner flakes being smaller. **Figure 4.1c** shows a typical optical image of exfoliated InSe flakes of different thicknesses on a 300 nm thick SiO_2 on Si. The flakes with a few nanometers thickness can be seen due to an optical interference effect and the thickness of atomic layers can be extracted from the colour contrast using an optical microscope.[41]

4.1.2. Patterning CVD graphene samples

The vdW heterostructures studied in this thesis were primarily fabricated on (i) patterned graphene using commercially available CVD graphene on 300 nm thick SiO_2 on Si or on (ii) a bare 300 nm thick SiO_2 on Si. The graphene/SiO_2/Si structures were processed by electron beam lithography (EBL) using a nanobeam nB5 EBL tool in the Nanoscale and Microscale Research Centre (nmRC) at the University of Nottingham by Dr. Zakhar Kudrynskyi and myself.

Before the EBL processing, a CVD graphene/SiO_2/Si substrate is spin-coated with polymethyl methacrylate (PMMA) (8% in anisole) at 4000 rpm for 30s and baked partially on a preheated hot plate at $T = 180\ ^{\circ}C$ for 10 minutes and left to cool down to room temperature followed by a further spin-coat of PMMA

(2% in anisole) under the same conditions. The resulting stack of thickness ~ 500 nm is used as a high-resolution positive electron-beam resist. The sample is then patterned by EBL in which an accelerated beam of electrons breaks molecular bonds in the PMMA, thus changing its solubility according to the pattern drawn by software. Selective removal of the exposed regions of the resist is done by immersing it in a solution of isopropyl alcohol (IPA) and deionised water (DI) water at a ratio of 7:3, leaving the unexposed PMMA as a mask to pattern graphene by plasma etching. We use reactive ion etching (RIE) using Corial 200IL RIE/ICP plasma etcher that mixes bombardment by ions and chemical etching with alternating electric fields with a range of gas chemistries. **Figure 4.2a** shows an optical image of CVD graphene patterned into squares of lateral dimension 20 μm x 20 μm, leaving 1 μm gap between two consecutive squares.

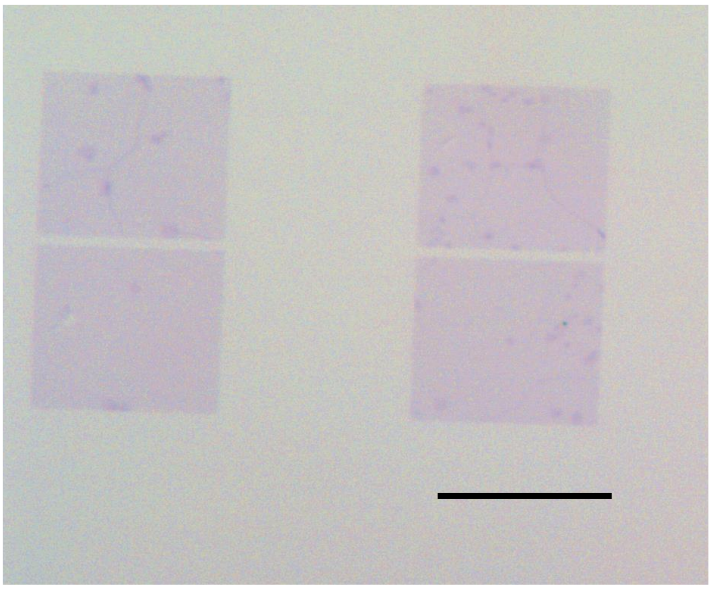

Figure 4.2. Optical images of CVD graphene patterned into squares of lateral dimension 20 μm x 20 μm, leaving 1 μm gap between two consecutive squares, scale bar: 20μm.

To deposit titanium/gold (Ti/Au) at the graphene edges to form contact pads for two-terminal devices (as discussed in chapter 8), a dual-layer of PMMA (A8 and A2) are spin-coated followed by another EBL exposure and development procedure, as described above. The metal deposition is carried out by loading the masked graphene/substrate into an Edwards Auto 305 thermal evaporator. At a typical deposition rate of 0.30-0.45 nms^{-1}, a Ti/Au (10/100 nm) bilayer is deposited and left for several minutes to cool down to room temperature. To remove the excess metal and unexposed PMMA, the substrates are immersed in acetone at T = 60°C for ~ 1-3 hours and rinsed with IPA and gently dried by a pressurised nitrogen gas stream. Finally, graphene is cleaned by thermal annealing in argon: hydrogen ($Ar:H_2$ = 95:5) atmosphere at T = 300°C for 3 hours. Similarly, for vertical graphene/InSe/graphene heterostructures (as discussed in chapters 6 and 7) on bare SiO_2/Si substrates, Ti/Au is deposited by thermal evaporation using a commercially available pre-designed mask to form contact pads.

4.1.3. All-dry deterministic transfer

A deterministic all-dry transfer set-up based on the technique detailed by Castellanos-Gomez *et al.* [131] was used to control the position and alignment of the exfoliated vdW nanosheets. Typically, mechanically exfoliated nanosheets on PDMS film adhered to a glass microscope slide are examined under an optical microscope to locate the desired nanoflake. A scheme of the transfer set-up used in our experiments is shown in **Figure 4.3**. A pre-patterned substrate is mounted using double-sided tape onto a copper plate on top of a transitional (x,y) stage (M-511.HD stages from Physik Instrumente) with a precision of up to 1 μm. The microscope slide is attached with a transfer arm onto a three-axis (x, y, z)

micromanipulators with the nanosheets facing towards the target substrate. As both the PDMS stamp and the microscope slide are transparent, the chosen nanoflake can be relocated and positioned at the desired location of the substrate.

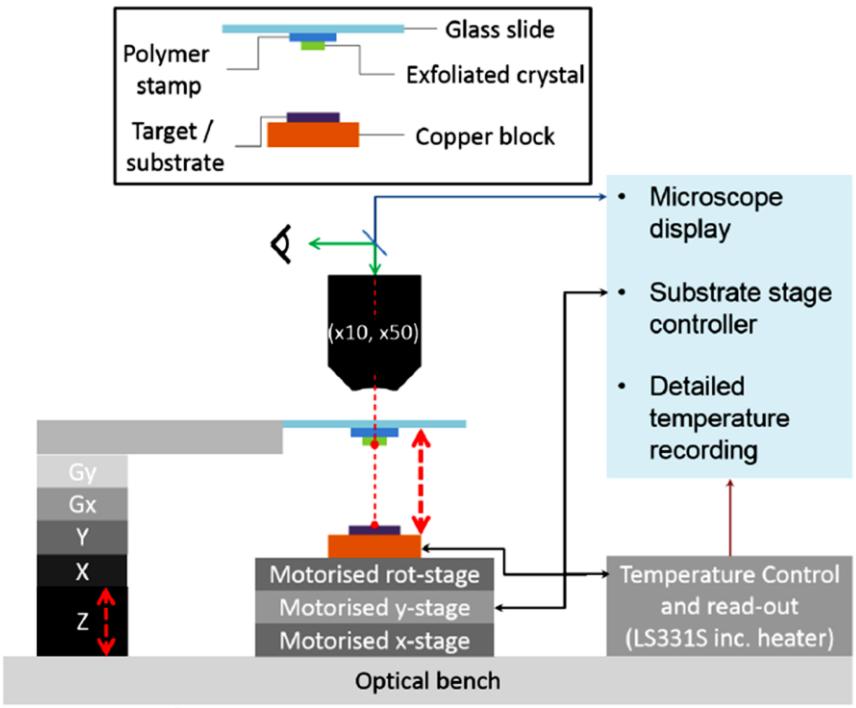

Figure 4.3 Schematic diagram of the all-dry deterministic transfer set-up of exfoliated flakes onto arbitrary substrates**.** The figure is reproduced from Ref. [45].

The copper block on the stage can also be rotated to aid the alignment. The *z*-micrometre is handled slowly to bring the flake nearer to the substrate and finally peeled onto it by controlled adjustments while monitoring the optical microscopic image on the computer screen continuously. The temperature of the copper block (hence, the substrate) can be controlled in the range 300 K< T < 500 K by a ~20 W heater and PT100 temperature sensor connected to a LakeShore-331S temperature controller. However, for the InSe flake transfer, the temperature is strictly kept under 373K, as Se-vacancies can form at high temperatures, leading to surface oxidation in air.[48]

4.1.4. Needle-assisted transfer of graphene microsheets

Inspired by Bie *et al.*[132], a site-specific transfer technique of individual graphene microsheets to arbitrary substrates was developed by our group. This development involved a research visitor, Mr Quanshan Lv, from the Institute of Semiconductors (Chinese Academy of Sciences, Beijing, China), Dr. Zakhar Kudrynskyi and myself. In this method, several graphene microsheets with a lateral dimension of 10 μm x 40 μm are tailored by EBL using commercially available CVD graphene on 300 nm thick SiO_2 on Si, as described in section 4.1.2.

Following the EBL processing, the resultant PMMA-graphene stack on SiO_2/Si is etched in a solution consisting of Buffered Oxide Etch (BOE) and Hydrofluoric acid (HF) at a ratio of 5:2. After a few minutes, PMMA/graphene film floats on the top of the etching solution surface, which is sieved using a plastic boat and transferred into DI water. The film is washed several times with DI water, following which a copper grid is used to remove it carefully. After drying in an inert atmosphere overnight, the PMMA/graphene film is used for the transfer of individual graphene microsheets onto a target substrate deterministically. **Figure 4.4** shows the step by step transfer process of graphene microsheets.

The copper grid containing the PMMA/graphene microsheets is attached to the copper block in the transfer set-up, as described in section 4.1.3. A glass fiber with a tip diameter of ~500 nm is attached with the transfer arm of the set-up. Using three-axis (*x*,*y*,*z*) micromanipulators, one corner of a microsheet is touched gently with the needle tip. The microsheet is torn apart from the base membrane and adhered to the needle for transfer onto a target substrate. After a

successful transfer, the substrate containing graphene microsheet is heated on a hot plate at T = 180 °C for 30 minutes and dissolved in acetone for 30 mins to remove the PMMA.

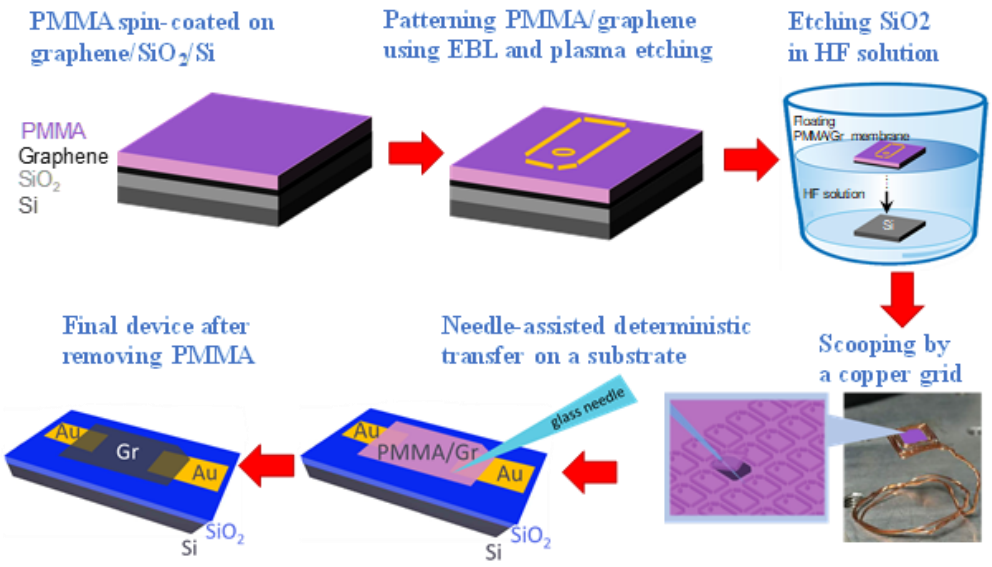

Figure 4.4. Schematic diagram of step by step procedure of needle-assisted transfer of graphene microsheets.

4.2. Topographical studies

The unique properties of 2D layered materials result from the significant changes in their band structures compared to their bulk counterpart. For example, the layer thickness of 2D materials modifies the crystal symmetry and atomic distances, which affects the physical properties of 2D materials, such as the band gap, phonon vibration frequencies *etc.*[29,133] Moreover, mechanical strain causes topographical variations at a nanoscale, which can further modify these properties.[134,135] We used scanning electron microscopy (SEM) and Atomic force microscopy (AFM) for a detailed analysis of the surface properties, layer thickness *etc.* of the layers and heterostructures studied in the thesis.

4.2.1. Scanning electron microscopy (SEM)

A scanning electron microscope (SEM) can image the topography of low dimensional materials with high-spatial resolution. **Figure 4.5a** shows the schematic diagram of the SEM.

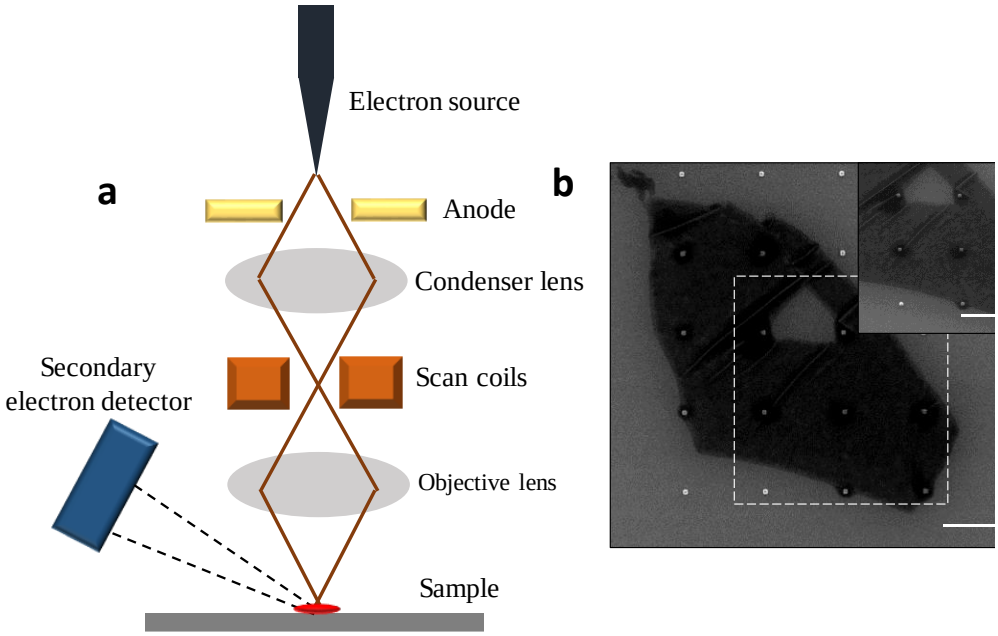

Figure 4.5.(a) Schematic diagram of a Scanning Electron Microscope (SEM). **(b)** SEM image for an InSe flake on Si-pillars. Scale bar: 3 μm.

In this technique, a sample is sealed inside a holder and mounted on a three-axis transitional and semi-rotational (up to an angle 40°) stage. Under high vacuum conditions (~ 10^{-8} mbar), an electron beam is accelerated by the anode voltage up to 15 kV and directed towards the sample. The beam is narrowed by condenser lenses and is focussed by objective lenses on a tiny spot (~ 5 nm diameter) on the sample. The spatial resolution of the spot size can be further modulated by an array of lenses and by optimizing the accelerating voltage. The focused beam of electrons probes the interaction between high energy electrons and atoms on the sample surface, causing the emission of secondary electrons, which are collected by the detector. These signals are amplified to produce high-

resolution topographical images of the surface or near-surface features of the sample.

Scanning electron micrographs were obtained using a JEOL 7100 Field-Emission Gun Scanning Electron Microscope (FEG-SEM) at the nmRC, the University of Nottingham by Dr. Nigel Neate and myself. **Figure 4.5b** shows a typical example of SEM image for an InSe nanoflake on Si-pillars (see also the detailed discussion in chapter 5).

4.2.2. Atomic force microscopy (AFM)

Atomic force microscopy (AFM) was used to study the surface topography and to determine the layer thickness of the nanoflakes. A typical AFM system contains a piezoelectric transducer, a cantilever with a sharp tip and a detector along with feedback electronics. The tip interacts with the sample and the feedback system precisely senses the interaction between the tip and sample using a laser-bouncing optical-lever technique, which utilizes a fast position-sensitive photodetector (PSPD), as shown in **Figure 4.6a**. Atomic forces between tip and sample depend on the sample morphology and are detected by the PSPD. Upon receiving the signal from the PSPD, a current is fed back to the system. Thus, the topography of the surface is directly measured by the deflections of the cantilever. Generally, AFM can be performed using different scanning modes, *viz.* contact mode and non-contact or tapping mode. In the contact mode, the setpoint is kept constant while the tip and sample interact with each other. Thus, the lateral force exerted on the sample can be quite high, resulting in sample damage or the movement of loosely attached objects. In contrast, in the tapping mode, the tip oscillates at a given resonance

frequency near the sample surface. The tip-sample distance is controlled by keeping either the amplitude or the phase of the oscillating cantilever constant using feedback electronics.

For our experiments, AFM measurements were conducted by myself in the tapping mode using a MFP-3D system (Asylum Research: Oxford Instruments) with Windsor Scientific Multi 75Al-G AFM probes. This AFM system has a sub-angstrom resolution in the *z*-direction and nanometer resolution in the *xy*-plane. A Tap300AL-G tip was used with a cantilever resonant frequency $f \sim 300$ kHz, force constant $k \sim 4$ Nm^{-1} and tip radius of ~ 7-10 nm. **Figure 4.6b** shows a typical AFM image and corresponding *z*-profile of an exfoliated InSe nanoflake of thickness $t \sim 28$ nm on a SiO_2/Si substrate.

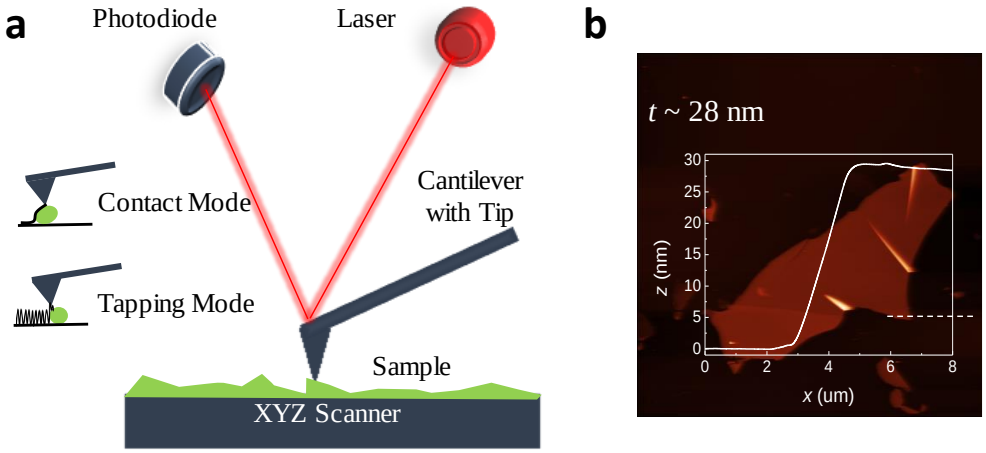

Figure 4.6.(a) Schematic diagram of an AFM system with tip-sample interaction in contact and tapping mode. **(b)** Acquired AFM image and corresponding *Z*-profile of an exfoliated InSe nanoflake on a SiO_2/Si substrate.

4.3. Optical studies

2D layered materials have extraordinary optoelectronic properties owing to their distinct electronic band structures and quantum confinement of charge carriers.[7,33] Several spectroscopy techniques, such as micro-photoluminescence

(μPL), micro-Raman (μRaman) and imaging ellipsometry were extensively used in this thesis to study the fundamental light-matter interaction in 2D materials. This is essential to probe their properties and exploit them in optoelectronic applications.

4.3.1. Micro-Photoluminescence and Raman spectroscopy

Photoluminescence (PL) is the radiative emission of photons by a material after light excitation. In a PL experiment, a laser with energy (E) higher than the band gap (E_g), *i.e.* $E = h\nu > E_g$ is focused on the surface of the material, leading to photon absorption and generation of electron-hole pairs. An electron excited onto a state in the conduction band (CB) relaxes and eventually recombines with a hole in the valence band (VB) by emitting a photon of energy smaller than $h\nu$ via different recombination processes. In the single-particle approximation and for an ideal crystal with no impurities, electrons and holes recombine from the edge of the conduction and valence bands, thus generating photons of energy equal to the band gap energy E_g, as shown in **Figure 4.7a**. However, due to the Coulomb interaction between carriers or excitonic interaction,[136] the energy of the emitted photon is smaller than E_g by an amount corresponding to the exciton binding energy. Furthermore, optical transitions can involve both free and bound excitons, and the recombination of carriers from states due to defects and impurities, resulting in multiple additional optical transitions, as shown in **Figure 4.7b-e**.

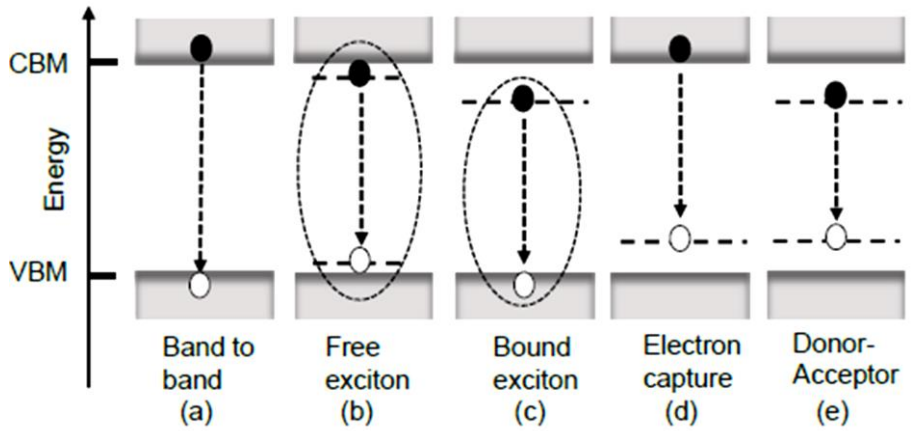

Figure 4.7. Schematics of the carrier recombination processes in photoluminescence for **(a)** band-to-band; **(b)** free exciton; **(c)** bound exciton; **(d)** electron capture onto an acceptor and **(e)** donor-acceptor transitions. Figure reproduced from Ref [136].

PL experiments can be used to gather useful information about the band gap energy and states in the forbidden gap due to impurities and defects.[136] For example, the PL linewidth and peak energy can reveal information about impurity type (acceptor or donor) and concentration, as well as thickness and composition of low-dimensional materials.[137] Experiments can be conducted at different temperatures and with temporal resolution (time-resolved PL) and used to extract useful information about radiative lifetimes[12] and density of states.[136]

The Raman spectroscopy technique is based on the inelastic scattering of light by lattice vibrations (phonons). **Figure 4.8** shows the diagrammatic representation of the Raman scattering process. In a first-order Raman process, a photon of energy $h\nu_i$ and wave vector k_i is scattered by one phonon of energy $E_q = \hbar\omega_q$ and wave vector q, which is either excited or absorbed. Since energy and momentum are conserved, the energy and momentum of the scattered photon are given by

$$\hbar\omega_s = \hbar\omega_i \pm \hbar\omega_q, \tag{4.1}$$

$$\hbar k_s = \hbar k_i \pm \hbar q. \tag{4.2}$$

The positive and negative signs correspond to the phonon absorption (anti-Stokes component) and phonon excitation (Stokes component). Typically, the Stokes component is only detected as the probability of anti-Stokes processes is smaller. Raman spectroscopy can measure directly the vibrational energies. The intensity of the Raman signal is generally expressed as a function of the wavenumber difference between the incident and scattered photon. Raman spectroscopy has been widely used to study the vibrational mode intensities and effect of strain applied to a crystal and has become a standard characterization technique for TMDCs, graphene and other layered materials.[138]

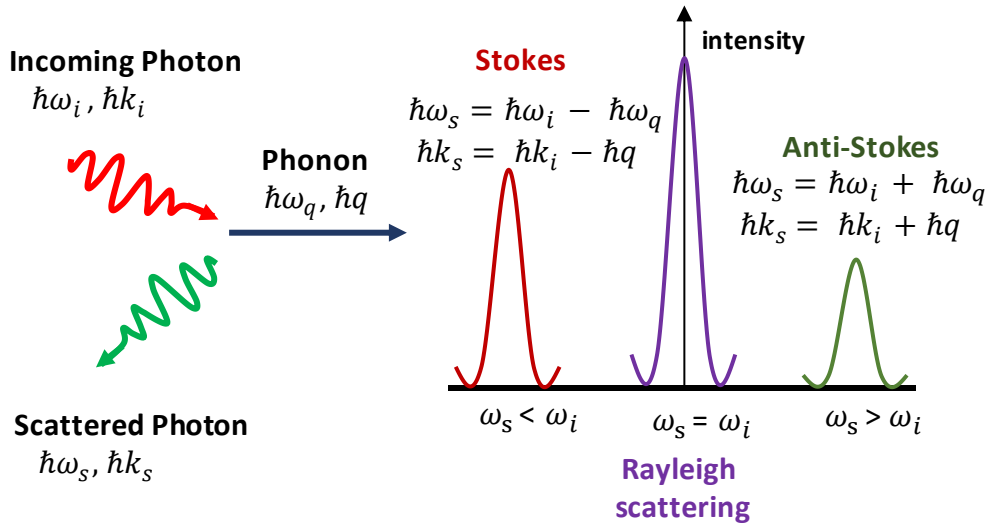

Figure 4.8. Representation of the Raman scattering process: phonon absorption (anti-Stokes component) and phonon excitation (Stokes component) conditions. Rayleigh scattering, which is the elastic scattering of light, is also shown.

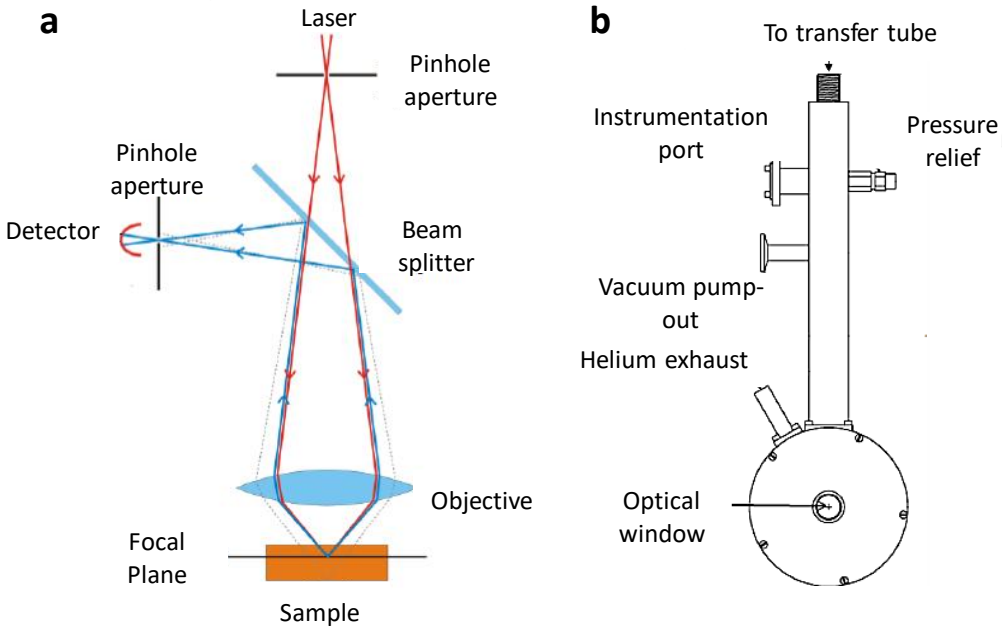

Figure 4.9. (a) Confocal microscope for μPL and μRaman spectroscopy studies. **(b)** Schematics of a cold finger optical cryostat used for low-temperature studies.

The PL and Raman experiments were conducted using a LabRAM HR-UV spectrometer equipped with a confocal microscope, excitation laser optics and an *XYZ* motorized stage. A schematic diagram of the confocal microscope is shown in **Figure 4.9a**. A laser beam (He-Ne, λ = 633 nm or frequency-doubled Nd: YVO4, λ = 532 nm) is used to excite the samples mounted on the stage. The focal length (*f*) and numerical aperture (*NA*) of 50x and 100x objectives are *f* = 3.6, 1.8 mm and *NA* = 0.55, 0.9, respectively, providing a focused beam diameter of ~1 μm (thus, μPL) on the sample surface. The PL signal is dispersed by a grating of either 150 g/mm or 1200 g/mm and is detected by a Si charge-coupled device (CCD) (detection range λ = 350 nm - 1100 nm). The pinhole aperture blocks stray light emitted due to the excitation by the laser beam outside the sampling area. A series of motorised neutral density filters are available to modulate the power of the lasers. Room temperature μPL and μRaman mapping are done with the help of the motorised stage with micrometre precision.

For low-temperature μPL studies, the samples are held in vacuum and mounted inside a cold finger optical cryostat with a sapphire window of 1 cm diameter (**Figure 4.9b**). The samples are mounted on a copper plate by silver paint. The temperature within the cryostat is controlled by a continuous helium flux via a transfer tube from a He dewar with an external pressure regulator and is continuously monitored. By balancing the level of He flux against the output of the internal cryostat heaters (controlled by a Lakeshore LS331S temperature control unit), temperatures between T = 8 K and 300 K can be reached. For low temperature studies, the DuoScan mode is used as the sample is mounted inside a cryostat that cannot be moved precisely.The microscope is equipped with a mirror that can be motorized. This enables to scan the laser beam over the sample. This imaging mode (DuoScan) differs from the imaging mode in which the laser and mirror are kept fixed and the sample is scanned by using a motorized stage. Both imaging modes can be used. A smaller mapping area (~ 5 x 5 μm^2) is chosen to minimize the loss of focus due to changes of the optical path during the mapping.

4.3.2. Spectroscopic imaging ellipsometry

Spectroscopic ellipsometry is a powerful, non-destructive technique that enables to study the complex dielectric function of thin films. Imaging ellipsometry combines the conventional ellipsometry with the lateral resolution of microscopy, making it ideal for studying 2D materials. The basic principle behind ellipsometry is the change in the polarized state of light following its reflection from a sample. The reflection from a material at a particular wavelength λ is characterized by two ellipsometric angles, psi (Ψ) and delta (Δ), which are defined as

$$\tan\psi = |\frac{r_p}{r_s}|, \tag{4.3}$$

$$\Delta = \delta_p - \delta_s, \tag{4.4}$$

where r_p and r_s are the Fresnel reflection coefficients and δ_p and δ_s are phase differences for *p*- and *s*-polarized light. The collected data usually go through different mathematical modelling of the reflected beam, from which it is possible to extract the real (η) and imaginary (κ) parts of the complex dielectric function ($N = \eta \pm i\kappa$) of the material. Thus, optical absorption (α), which is defined as $\alpha = \frac{4\pi\kappa}{\lambda}$, can also be obtained.

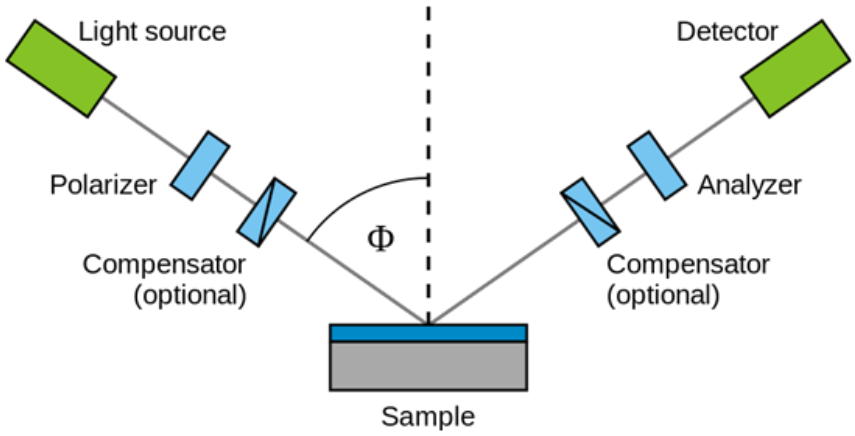

Figure 4.10. Schematic diagram of the spectroscopic ellipsometry setup.

Ellipsometry measurements were performed using a variable angle spectroscopic ellipsometer (VASE) at the School of Physics and Astronomy, the University of Nottingham by Dr. Christopher Mellor, Dr. Richard Cousins and myself. **Figure 4.10** shows the scheme of the ellipsometry measurement set-up. Typically, a sample is placed onto a motorized stage and illuminated with collimated light. The goniometer mainly consists of two parts, a polarizer and an analyzer equipped with a CCD camera, which enables the visualization of the sample surface in real-time. By the rotation of the polarizing components and

wavelength of the incident light, Δ and Ψ are measured. The collected data is processed by software using different mathematical modelling to extract the corresponding optical constants.

Optical absorption is a direct measurement of the electron-photon interaction in a material. For exfoliated 2D materials with a few microns lateral dimensions, optical absorption spectroscopy is generally challenging due to the incident beam diameter being larger than the flake size. Thus, the enhanced spatial resolution of an imaging ellipsometer in the range of ~ 2 μm can enable important investigations of 2D materials. Ellipsometric contrast micrographs, psi (Ψ) and delta (Δ) maps, as well as spectra, have been reported in the literature for multilayer graphene/graphite stacks and TMDCs.[139-141] In this thesis, this technique is used to study InSe.

4.4. Transport studies

2D layered materials and their heterostructures have been explored widely to study carrier dynamics and electronic transport. For these systems, electronic transport measurements can probe inherent properties, including band structures, their dependence on thickness and external fields, valley polarization, scattering mechanisms, electrical contacts, and doping.[142] In this thesis, transport measurements were used to study vdW heterostructure devices based on InSe.

4.4.1. Current-voltage measurements

The electrical transport properties of the heterostructures are measured using two probe configurations inside a cryostat attached to a turbo-molecular pump to set the pressure down to 10^{-6} mbar. At first, the devices are measured in absence of light. For DC measurements of currents > 1 nA, we use Keithley 2400

source meters and Keithley2010 DC voltmeters. An additional source meter is used to apply a gate voltage through the SiO_2/Si substrate. The devices are also investigated under illumination to measure the photoconductivity, which corresponds to a change in the conductivity of the material system caused by the excess carriers generated by the absorbed photons. The dark electrical conductivity (σ) and the photoconductivity ($\Delta\sigma$) of a material can be defined as

$$\sigma = q\,(n\mu_n + p\mu_p) \tag{4.5}$$

$$\Delta\sigma = q\left(\Delta n\mu_n + \Delta p\mu_p\right) \tag{4.6}$$

where q is the electron charge, n and p are the free electron and hole concentrations, and μ_n and μ_p are electron and hole mobilities, respectively.

For photocurrent measurements, the lid of the cryostat is replaced by a sapphire window of 1 cm diameter. The device is exposed to an unfocused laser source (λ = 633 nm or λ = 405 nm) with powers (P) of up to 10 mW. The photoresponsivity of the heterostructures can also be measured at different P by regulating the incident laser power on the devices. A series of neutral density filters are available to modulate the power of the lasers.

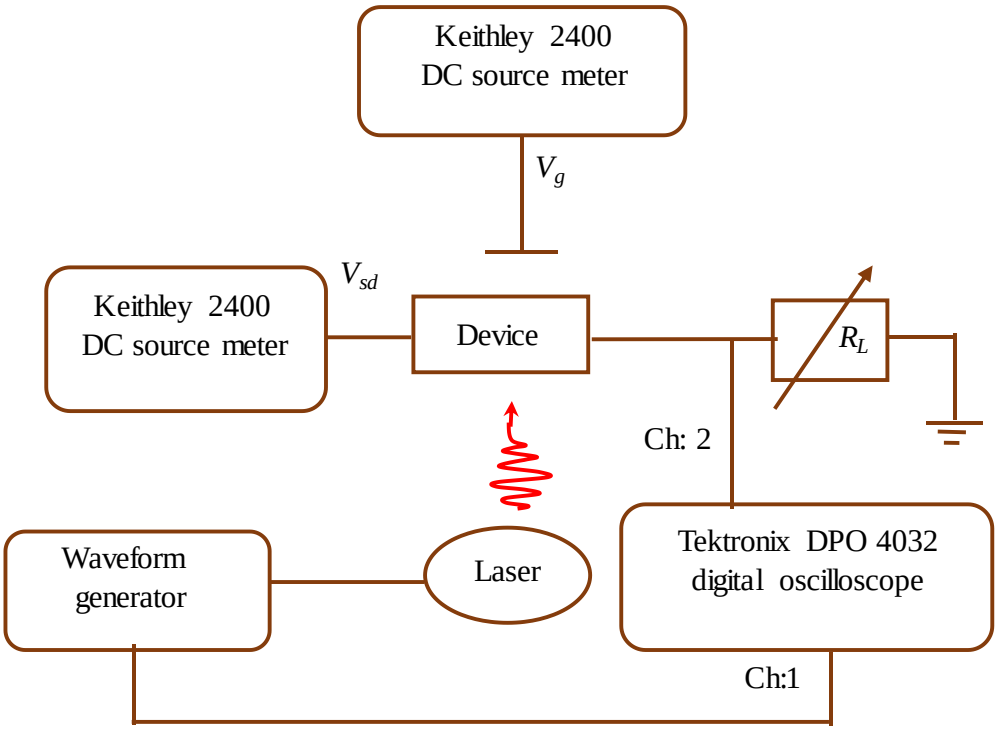

Figure 4.11. The set-up used for temporal studies of the photocurrent.

The temporal response of the photocurrent was also studied. **Figure 4.11** shows the schematics for these studies. The device is connected in series with a load resistor and with Keithley 2400 delivering the source (V_{sd}) and gate (V_g) voltages. An arbitrary waveform generator (TTi TGA 1241) is used as a source to a chopper to modulate a laser source (λ = 633 nm or λ = 405 nm). The source waveform is recorded by a Tektronix DPO 4032 digital oscilloscope. The laser source, modulated by the chopper, generates an AC signal from the devices due to photocurrent. This signal is measured simultaneously across the load resistor using a digital oscilloscope. The photocurrent signal is investigated in the frequency range f = 1 - 400 Hz.

4.4.2. Photocurrent spectroscopy

Spectral photoconductivity provides a powerful technique for probing optical transitions and measure the band gap energy. Photocurrent studies can be

carried out by modulating the incident light with a chopper. The modulated (AC) conductivity rejects the contribution of high dark current, revealing information about the photogeneration of carriers and its influence on the transport properties.

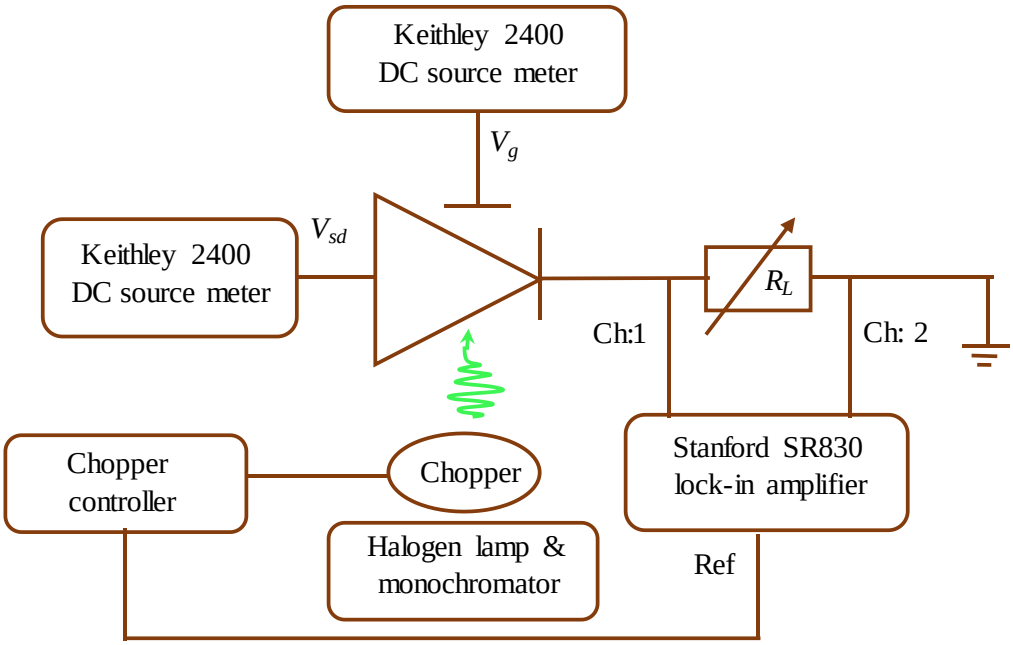

Figure 4.12 Photocurrent spectroscopy set-up.

Figure 4.12 shows the scheme for the photocurrent spectroscopy set-up used in the experiments. Photocurrent spectroscopy at variable photon wavelengths can be conducted using a lock-in amplification technique. The device is connected to a Keithley 2400 voltage source and a variable load resistor (1 - 100 MΩ) in series. A quartz halogen lamp (250 W) dispersed through a 0.25 m monochromator is employed as a photon source. The photoinduced current is measured by observing the voltage drop across the load resistor using a Stanford SR830 lock-in amplifier.

For photocurrent maps, the device is mounted inside a vacuum cryostat and place on a motorised stage with micrometre precision. A confocal

microscope system is used to focus the laser excitation (continuous, λ = 405 nm, P up to 1 mW) onto the sample with a diameter d ~1 μm. The device is connected to a Keithley 2400 voltage source. The laser beam scans across the surface of the devices by using the motorised stage, and the corresponding photocurrent spatial maps, highlighting the light-sensitive regions, are recorded.

Chapter 5

Enhanced optical emission from two-dimensional InSe bent onto Si-nanopillars

This chapter reports on the controlled modulation of optical signals by exploiting the inherent optical anisotropy and mechanical flexibility of atomically thin 2D vdW semiconducting InSe layers. This enhancement is achieved by straining and bending InSe nanoflakes onto a periodic array of Si nanopillars. We explain these findings by first-principles calculations of the electronic band structure of 2D InSe.

Si nanopillars were provided by Prof. Diana Huffaker and her group at the University of California, Los Angeles. Sample fabrication, topographical (AFM and SEM) and optical (μPL and μRaman) studies were conducted by myself at the University of Nottingham. The modelling of the data involved a collaboration with Prof. Lijun Zhang of Jilin University, China, and his master student Jiahao Xie, who conducted first-principles calculations of the electronic band structure of 2D InSe. The results presented in this chapter were published in *Advanced Optical Materials* **8**, 2000828 (2020).

5.1. Introduction

Controlling the propagation and intensity of an optical signal is central to several technologies ranging from quantum communication to signal processing. These require a versatile class of functional materials with tailored electronic and optical properties, and compatibility with different platforms for electronics and optoelectronics. Several recent works have focused on

atomically thin 2D vdW materials and their heterostructures as these offer opportunities to exploit a wide range of quantum phenomena.[7,143] Amongst these, an exciting and rapidly growing development involves InSe, with recent breakthroughs emerging from its unique electronic band structure. This differs qualitatively from that of many other 2D materials, such as the widely studied TMDCs.[39] The conduction band (CB) edge states of InSe arise from antibonding In *s*-states, whereas the top valence band (VB) consists of Se p_z-like orbitals.[34,39,98] Thus, band-edge excitons tend to couple preferentially to light polarized along the *z*-direction (or *c*-axis), rather than along the *xy*-plane as for TMDCs.[39] Furthermore, mechanical strain can modify these properties.[55,144-146] 2D vdW crystals can sustain high strain due to their large mechanical flexibility.[12,147,148] In particular, InSe is one of the most flexible systems with a small Young's modulus (23.1±5.2 GPa)[149] and band gap energy that is very sensitive to strain.[40] Thus, InSe represents a promising system to explore and exploit the effects of strain on electronic and optical properties.

In this chapter, we report on the modulation of the optical properties of atomically thin InSe layers under controllable bending conditions achieved by exfoliation and transfer of InSe flakes onto a periodic array of Si-nanopillars. We show a site-specific, reproducible bending of individual flakes onto the pillars and corresponding enhancement of the Raman and photoluminescence signals. By first-principles calculations of the electronic band structure of 2D InSe, we demonstrate that the measured effects arise from the orbital symmetry of the electronic states and light polarization selection rules, which are both dependent on the geometrical shape of the bent layers and their layer thickness.

5.2. Topography of InSe layers bent on Si-nanopillars

Figure 5.1a shows our fabrication method to bend thin InSe layers onto a periodic array of Si-nanopillars. The Si-nanopillars were fabricated by electron-beam lithography (EBL) and dry etching on 4-inch Si(100) wafers. The pillars are equally spaced by a distance d = 3 μm and have a width w = 100 nm. The average height, h, of the nanopillars in different arrays is 120 nm and 60 nm. **Figure 5.1b** shows SEM images of a typical Si nanopillar array and a single pillar of h = 120 nm and w = 100 nm (inset). Several samples were prepared by deterministic positioning of individual InSe flakes of different thicknesses t onto Si-nanopillars by all-dry viscoelastic transfer method, as described in section 4.1.3.

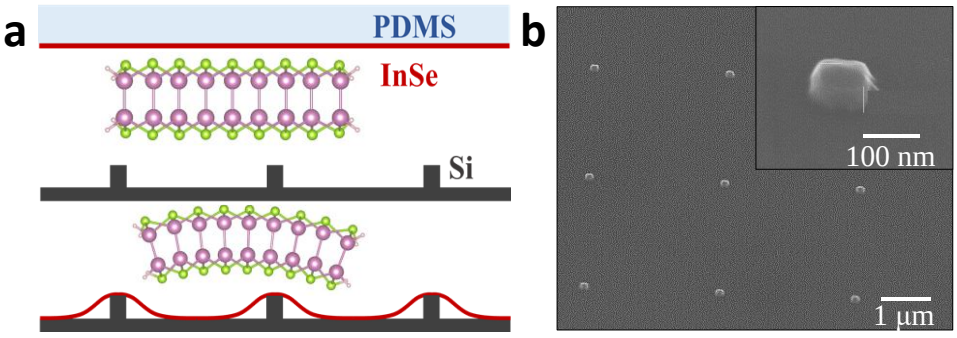

Figure 5.1. (a) The fabrication method of bending InSe layers onto Si-nanopillars with the InSe crystal structure before and after bending. **(b)** SEM images of a bare Si nanopillar array (inset: single pillar with h = 120 nm, w = 100 nm).

The thickness of the InSe flakes, t, was determined before the transfer onto Si-nanopillars by μPL spectroscopy. As discussed in chapter 2, the room temperature (T = 300K) PL peak energy of InSe, E_{PL}, is due to the band-edge exciton and is very sensitive to the layer thickness. It increases from E_{PL} = 1.25 eV for t > 20 nm to E_{PL} = 1.72 eV for t ~ 2 nm; correspondingly, the intensity of

the PL signal decreases markedly as t is decreased below t ~ 10 nm due to a direct-indirect band gap crossover.[26,33] **Figure 5.2a-b** shows the SEM images of a bulk InSe flake (t > 20 nm) over a periodic Si-pillar array, revealing brighter spots at the location of the pillars, suggesting strain around the pillar. SEM images acquired by viewing the InSe flake at a tilt angle of 40° to the electron beam (**Figure 5.2c**) indicates that the flake is tensed over each pillar with a bending extended over a radial distance (r) of approximately ~ 500 nm. We observed similar SEM images for atomically thin InSe layers, as shown in **Figure 5.2d-f** for an InSe flake with t = 5 nm.

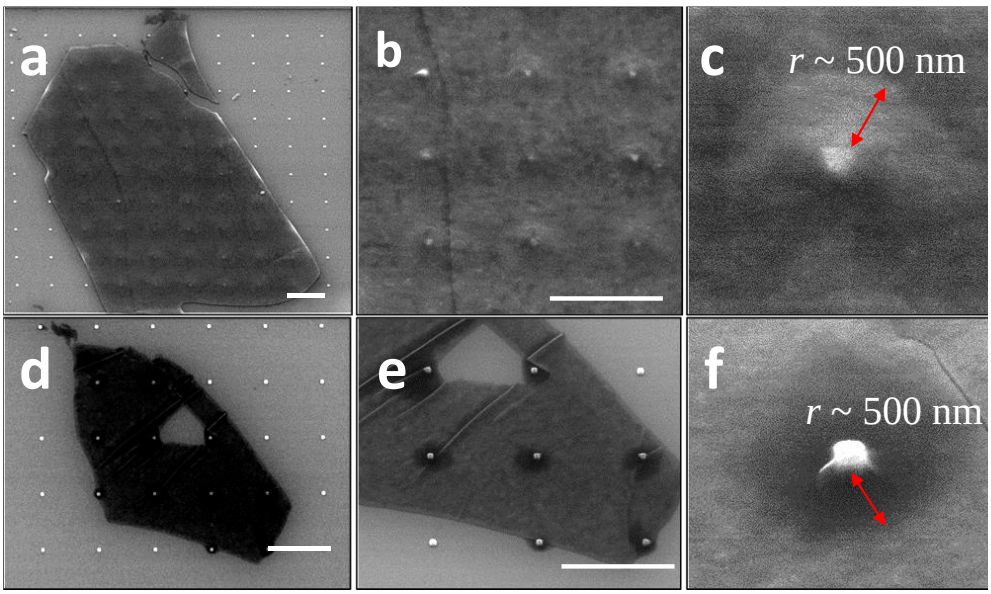

Figure 5.2. (a-c) SEM images of a bulk InSe flake (t > 20 nm) on Si-pillars (h = 120 nm, w = 100 nm). Scale bar: 3 μm. **(d-f)** SEM images of an InSe flake (t ~ 5 nm) on Si-pillars (h = 120 nm, w = 100 nm). Scale bar: 3 μm.

We obtained the topography of the bent layers by AFM. **Figure 5.3a** shows the three dimensional AFM image and height line profile (**Figure 5.3b-c**) for the InSe flake (t = 5 nm), which was imaged by SEM in Figure 5.2d-f. The bent flake had a nearly round base; its maximum height, z_0, is reached at the centre (r_0) of the pillar, corresponding approximatively to the pillar height h.

The height line profile is well reproduced by a Gaussian profile, *i.e.* $z = z_0 e^{-(r-r_0)^2/2b^2}$, where b = 425 nm and $z_0 = h$ = 118 nm.

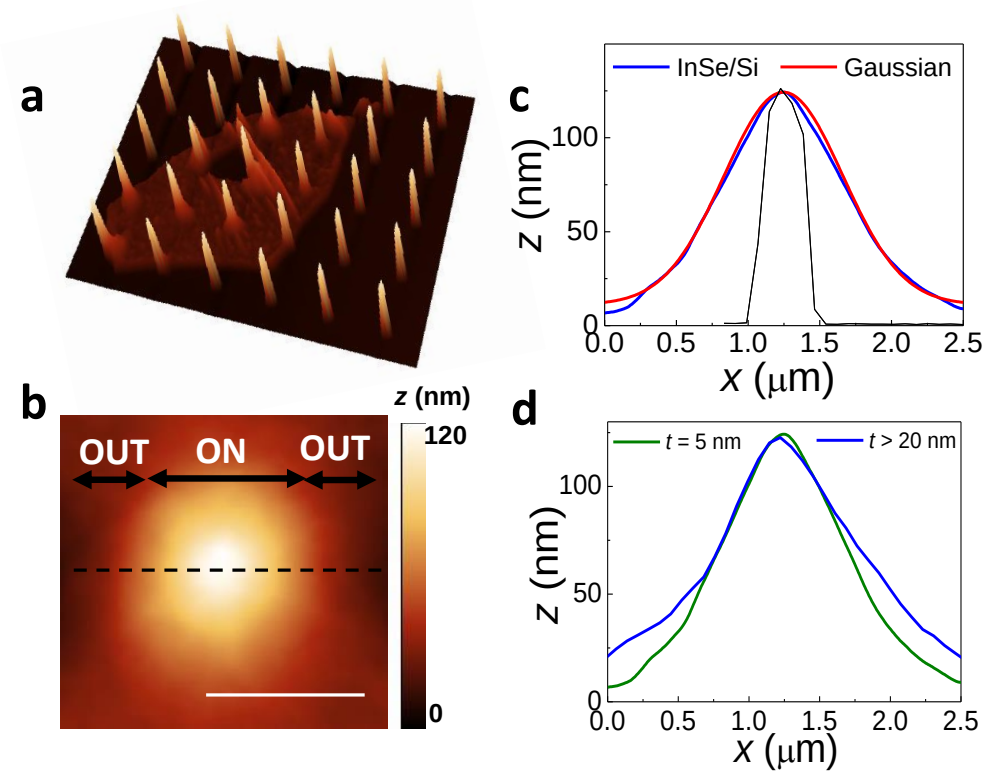

Figure 5.3. **(a)** Three-dimensional AFM image and height line profile **(b-c)** for an InSe flake with t = 5 nm over a Si-pillar. The area inside(ON) and outside(OUT) the pillar is marked. Scale bar: 1 μm. For comparison, the height profile for a Si-pillar is also shown (black). **(d)** Comparison of InSe flakes of different thickness (t > 20 nm and t = 5 nm) transferred onto nanopillars with h = 122 nm and w =100 nm.

Figure 5.3d compares the AFM profiles of bulk (t > 20 nm) and thin (t = 5 nm) flakes transferred onto an array of Si-nanopillars with the same h and w. For the bulk InSe flake with t > 20 nm (Figure 5.2a-c), the height profile is well reproduced by a Gaussian profile, *i.e.* $z = z_0 e^{-(r-r_0)^2/2b^2}$, where b = 480 nm and $z_0 = h$ = 118 nm. The height line profiles reveal a similar bending for thick and thin layers, corresponding to a bending angle of up to $\theta \sim 9°$.

The bending of the flakes was further probed in arrays with Si-pillars of different heights. **Figure 5.4a-b** shows the three dimensional AFM image and the height line profile of a bulk InSe flake (t >20 nm) transferred onto nanopillars of nominal height h = 60 nm and width w = 100 nm. The AFM z-profile shows a different bending of the flake (bending angle of up to $\theta \sim 5°$): this is described by a Gaussian profile, *i.e.* $z = z_0 e^{-(r-r_0)^2/2b^2}$, where b = 260 nm and z_0 = h = 64 nm. The reproducible topography of the bent flakes on different pillars within the array demonstrates that the method of fabrication is reliable. It also suggests that the shape of the bent flakes is determined primarily by the elastic properties of InSe and its excellent adhesion to Si due to attractive vdW interactions.

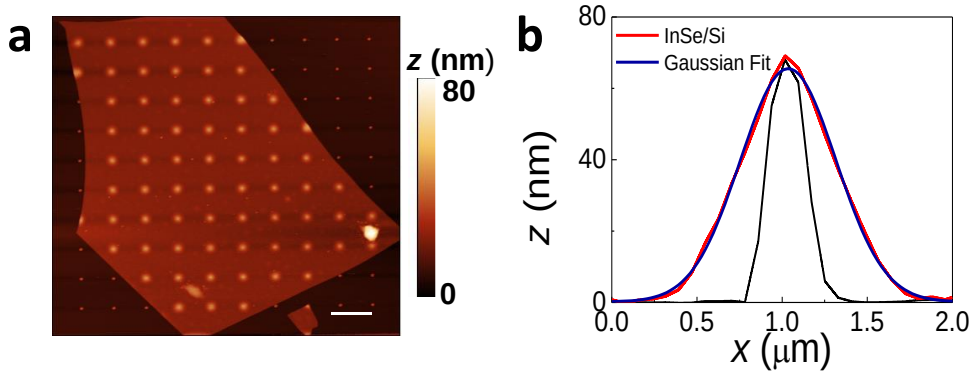

Figure 5.4. (a-b) Two-dimensional AFM image (a) and z-profile (b) for an InSe flake (t > 20 nm) over pillars of height h = 64 nm. Scale bar: 3 μm. For comparison, the height profile for a Si-pillar is also shown (black).

5.3. Nanoscale spatial modulation of μPL and Raman signals

To study the effect of bending InSe onto Si-nanopillars on optical properties, we conducted μPL studies on InSe nanoflakes of different thicknesses t. These experiments were conducted with incident light polarized in the layer plane, *i.e.* for an electric field dipole **E** perpendicular to the c-axis (**E**⊥***c***). The resonances in the absorption spectrum of InSe are broad. We used a laser

excitation energy of E_{exc}= 2.33 eV (λ = 532 nm) close to the energy of the interband optical transition (E_2 ~ 2.4 eV) between the $p_{x\text{-}y}$-like orbitals in the VB and the *s*-like CB states of bulk γ-InSe to probe the optical response near resonance condition.[150] Compared to the band-edge exciton energy, E_g, the energy of the E_2 transition depends less strongly on the layer thickness and increases only when *t* is reduced below *t* ~ 5 nm.[150]

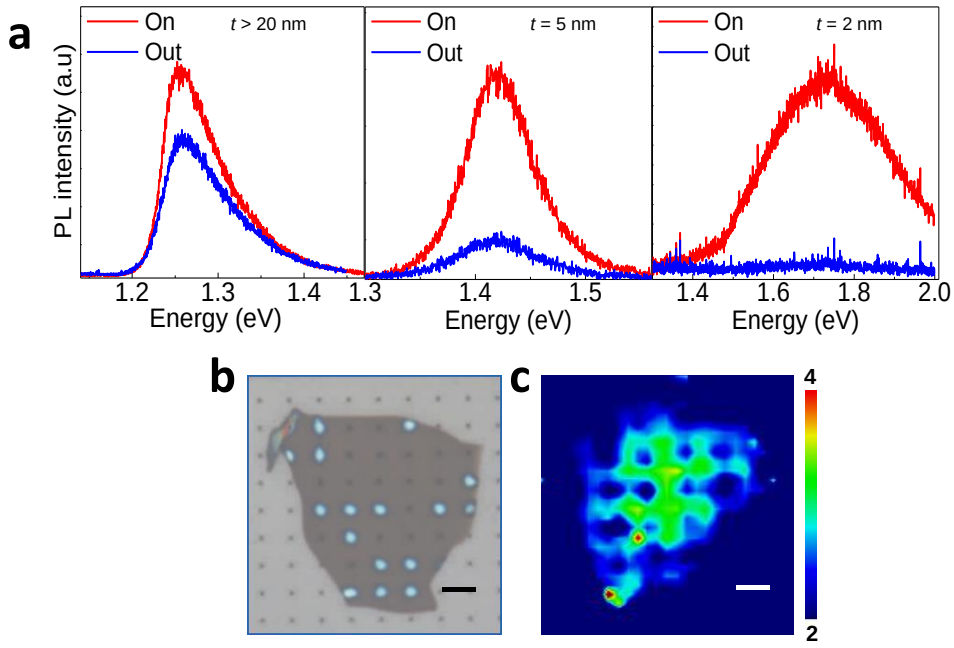

Figure 5.5 (a) Room temperature (*T* = 300K) µPL spectra inside and outside a Si-nanopillar for flakes of thickness from *t* = 2 nm to *t* > 20 nm (λ= 532 nm, *P* = 10^{-6} W). **(b-c)** Optical image of an InSe flake (*t* > 20 nm) after its transfer over the pillars (b) and the corresponding colour map of the µPL intensity (c). Scale bar: 3 µm.

Figure 5.5a shows representative room temperature µPL spectra inside and outside a Si-pillar for InSe flakes of thickness from *t* = 2 nm to *t* > 20 nm. The enhancement of the µPL signals is seen at the location of the Si-pillar. The PL emission is only slightly red-shifted (< 5 meV) at the site of the pillar and its linewidth does not change significantly.

Figure 5.5b-c shows the optical image of an InSe flake (t > 20 nm) transferred on the pillars and the corresponding colour map of the μPL intensity. Although the μPL is always enhanced on the pillars, the PL enhancement varied across the array. The pillars are well separated from each other and the width of each pillar is smaller than the wavelength of the emitted photons. Thus, an InSe layer bent onto a pillar acts effectively as a point-like source whose submicron size is limited by light diffraction (Figure 5.5c).

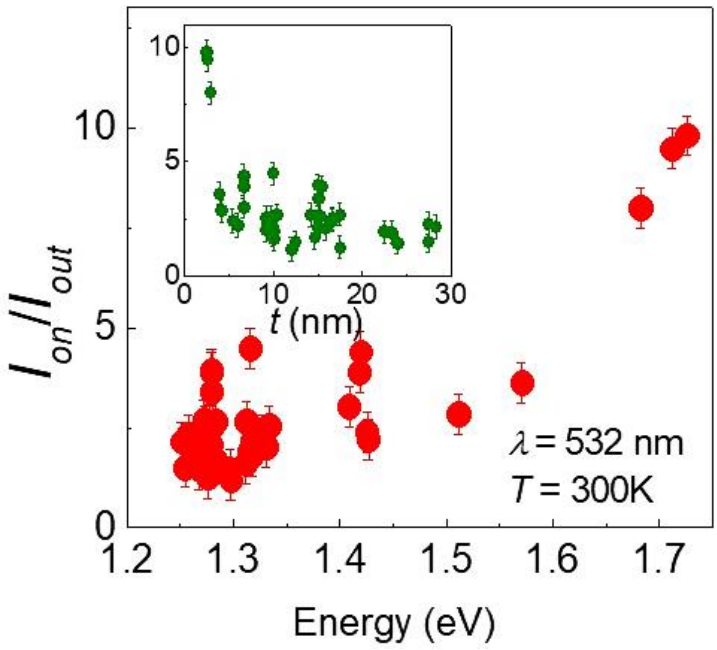

Figure 5.6. Ratio I_{on}/I_{out} of the PL intensities in and outside Si-pillars of average height h = 120 nm versus the PL peak energy for InSe flakes of different thicknesses t (T = 300K, λ = 532 nm, P = 10^{-6} W). Inset: Dependence of I_{on}/I_{out} on t.

Figure 5.6 shows data for the ratio between the PL intensity within (I_{on}) and outside (I_{out}) a pillar, I_{on}/I_{out} , versus photon energy (Figure 5.6) and t (Figure 5.6, inset), as obtained for InSe layers bent on single pillars. The PL intensity enhancement ratio, I_{on}/I_{out}, varies with the thickness of the flake: it is significantly enhanced for t < 5 nm (or PL peak energy E > 1.6 eV) and is larger

than 10 for t = 2 nm. The scatter in the data of Figure 5.6 suggests that the PL properties of the bent flakes are also influenced by crystal defects (*e.g.* ruptures, wrinkles, *etc*…) and/or surface roughness.

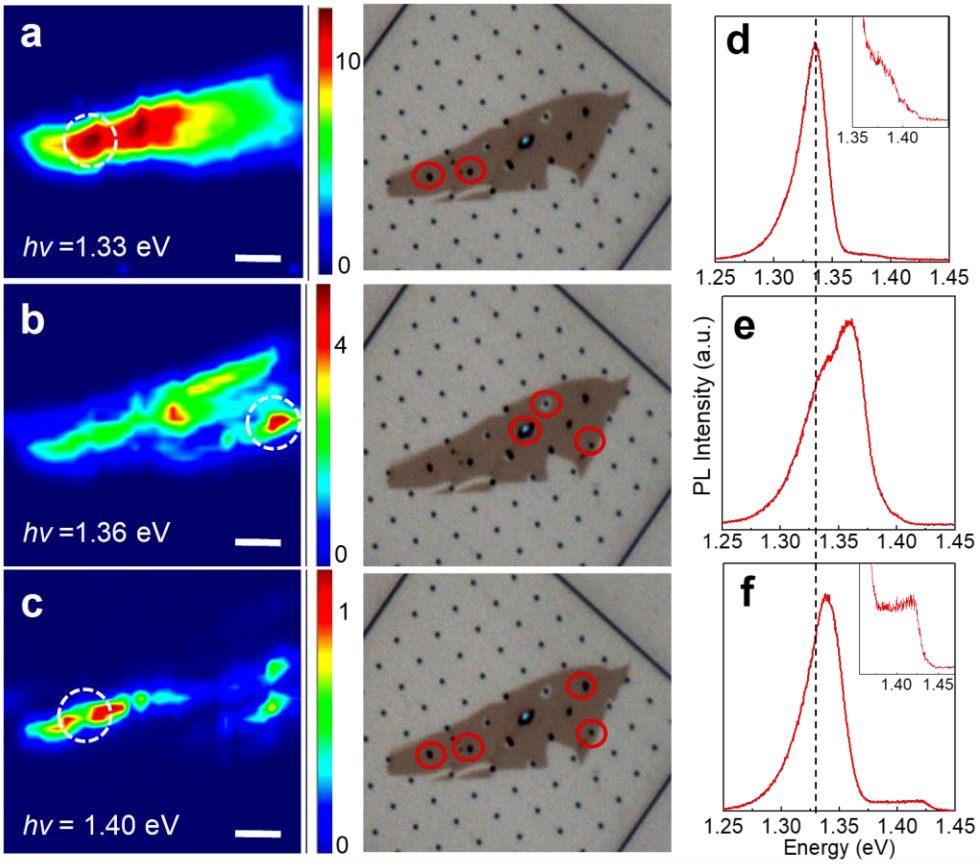

Figure 5.7 (a-c) Colour maps of the low temperature (T = 8K) μPL intensity at energies (a) E = 1.33 eV, (b) E = 1.36 eV and (c) E = 1.40 eV for an InSe flake of thickness t = 9 nm. Scale bar = 5 μm (λ= 532 nm, P = 10^{-5} W). The circles identify spots with strong μPL at specific energies. The right insets show optical images of the flake and specific pillars (circles). **(d-f)** μPL spectra at positions corresponding to the white circles in the colour map of parts (a-c). The dashed line illustrates that the PL lines are centred at different energies in different regions of the flake.

To explore the contribution of disorder and exciton localization phenomena to the PL emission, we measured the μPL spectra and μPL maps of InSe flakes at low temperature (T = 8K). **Figure 5.7a-c** shows the colour maps

of the PL intensity acquired at energies E = 1.33, 1.36 and 1.40 eV for an InSe flake with t = 9 nm. Representative PL spectra at specific positions (marked with white circles in the colour maps) are shown in **Figure 5.7d-f**.

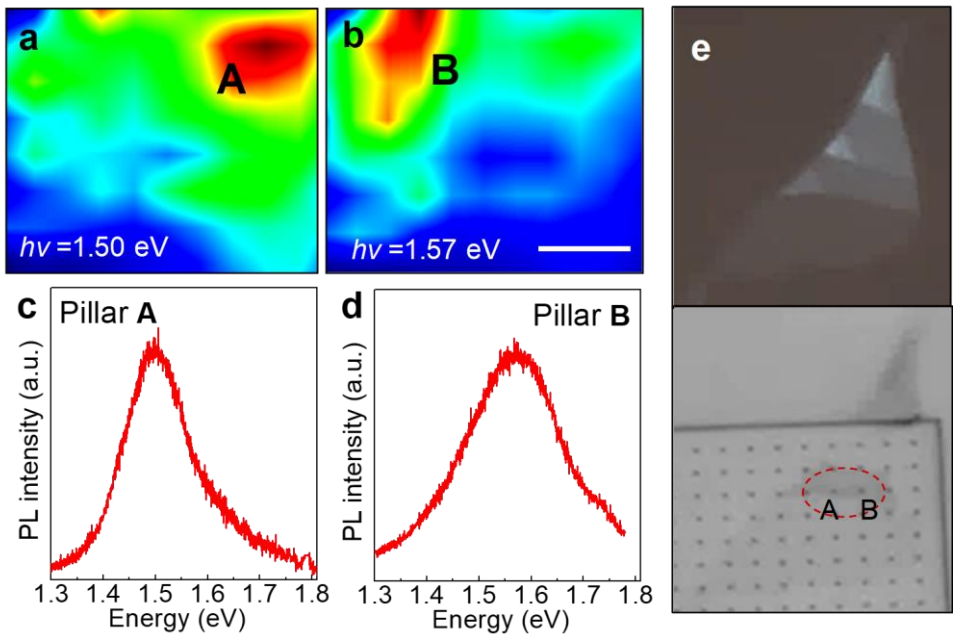

Figure 5.8 (a-b) Colour maps of the low temperature (T = 8K) μPL intensity at hv = 1.50 eV and 1.57 eV showing an enhanced μPL on two pillars labelled A and B for an InSe flake of thickness t = 3 nm. Scale bar: 2 μm (λ = 532 nm, P = 10^{-4} W). **(c-d)** PL spectra for the pillars A and B mapped in parts (a-b). **(e)** Optical images of the InSe flake before and after its transfer on the Si-pillars. The red dashed region demarks a section of the flake mapped by μPL in parts (a) and (b).

An enhancement of the PL emission can be observed at the location of the pillars (Figure 5.7a), but this is less strong than at RT. For different positions on the flakes, the PL emission remains always broad and does not reveal isolated narrow PL lines. However, for a few spots around particular pillars, the PL spectra reveal additional weak bands at energies of E~ 1.4 eV (Figure 5.7f). The energy position of the main low T PL emission (~1.33 eV) does not differ significantly from that (E = 1.31 eV) measured at RT on the same flake. This

weak *T*-dependence of the PL peak energy arises from the contribution of carrier recombination from localized states due to native dopants and donor-acceptor pairs that become ionized at high temperatures.[32,151,152] We observed similar behaviour for flakes of thickness down to t = 2 nm (**Figure 5.8a-b**).

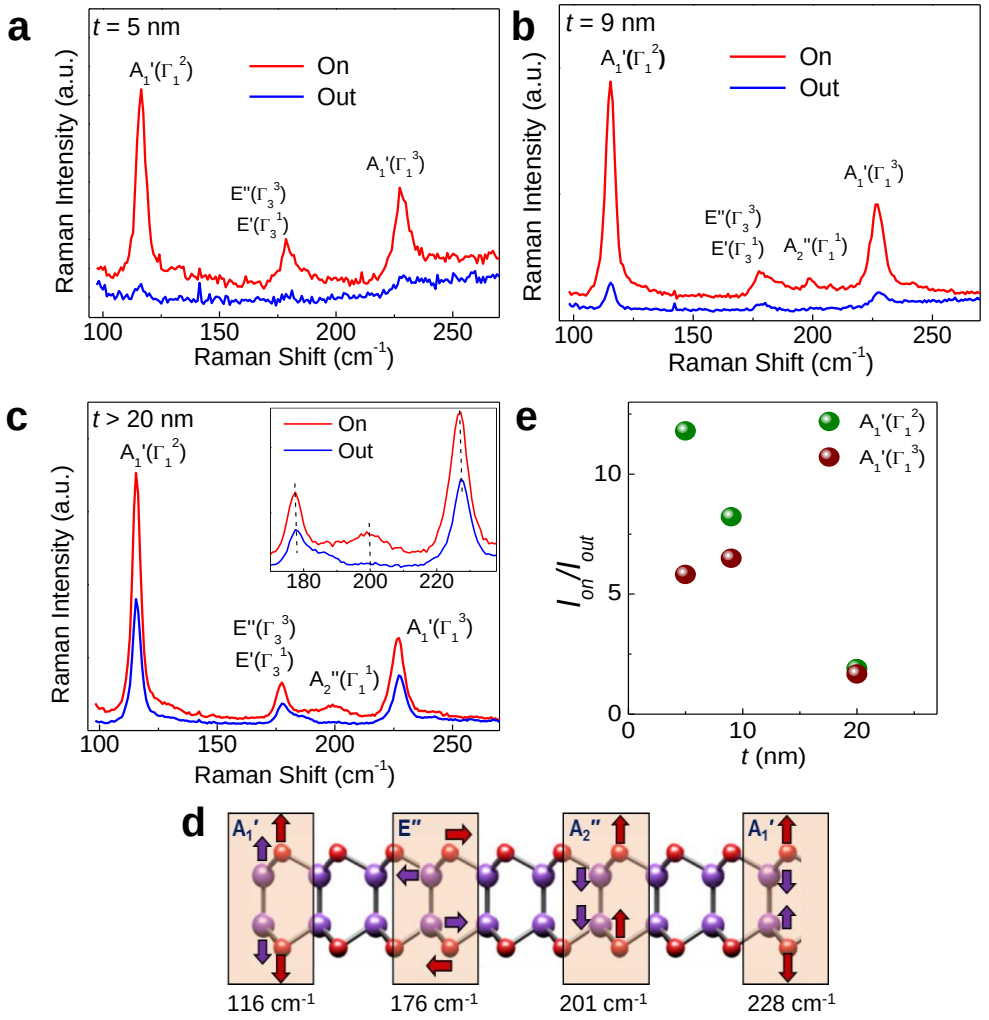

Figure 5.9. (a-c) Room temperature (T = 300K) Raman spectra inside and outside a Si-pillar of average height h = 120 nm for InSe flakes of thickness t = 5 nm (a) t = 9 nm (b) t > 20 nm (c). The inset illustrates three Raman modes. **(d)** Sketch of the Raman vibrational modes. **(e)** Ratio I_{on}/I_{out} of the Raman intensities in and outside Si-pillars of average height h = 120 nm versus the InSe flakes thickness t (T = 300K, λ= 532 nm, P = 10^{-6} W).

The spatial modulation of the PL signal is accompanied by a corresponding variation of the Raman signal. **Figure 5.9a-c** shows

representative Raman spectra for flakes of thickness t = 5 nm, t = 9 nm and t > 20 nm at different locations, inside and outside a pillar. The Raman signal decreases with decreasing layer thickness due to a reduced absorption coefficient, and no Raman signal can be detected for t < 5 nm. The Raman spectra reveal distinctive modes peaked at 116 cm^{-1}, 176 cm^{-1}, 201 cm^{-1} and 228 cm^{-1}. These correspond to the $A_1'(\Gamma_1^2)$, E′ (Γ_3^1)-TO /E″ (Γ_3^3), A_2'' (Γ_1^1)-LO, and $A_1'(\Gamma_1^3)$ vibrational modes of InSe, respectively, as shown in **Figure 5.5d**. **Figure 5.9e** shows that the enhancement of the Raman signal on the pillars is stronger in the thinnest layers and is of a similar order of magnitude as observed in PL (Figure 5.6a). In particular, the $A_2''(\Gamma_1^1)$-LO mode at 201 cm^{-1} is strongly enhanced (inset, Figure 5.9c). We observe a small shift to lower frequencies (by up to 1 cm^{-1}) of specific Raman modes (*e.g.* E′ (Γ_3^1)-TO /E″ (Γ_3^3) at 176 cm^{-1}, A_2'' (Γ_1^1)-LO at 201 cm^{-1}, $A_1'(\Gamma_1^3)$ at 228 cm^{-1}) at the location of the pillars (Figure 5.9c-inset). These modes involve out-of-phase vibrations of the In-Se bond within each vdW layer. Thus, we assign this shift to a change of the In–Se intralayer bonds, as shown in Figure 5.9d.

5.4. Modelling the enhanced optical emission

We performed density functional theory (DFT) based calculations using the plane wave pseudopotential approach as implemented in the VASP code to examine the role of the geometrical shape of the flake and strain on the electronic states and light polarization properties. As discussed in section 5.2, our InSe layers are tensed over the pillars with a well-defined profile described by a Gaussian with a maximum curvature $\kappa = z_0/b^2 \sim 7\times10^{-4}$ nm^{-1}. The corresponding shift of the Raman peaks (Figure 5.9) suggests a strain-induced change of vibrational and electronic properties.[12,34,55,144-149,153,154] To assess the

contribution of strain on the optical properties of the bent flakes, we simulated the electronic band structure of InSe layers bent along one direction with a curvature corresponding to the maximum curvature observed experimentally. The curvature is so small that it is difficult to see any difference between bent and flat layers at the atomic scale (**Figure 5.10**). The calculated band structure of the bent layers reveals a small band gap reduction of about 8 meV, which is in line with the measured energy shift (< 5 meV) of the PL peak in the bent flakes. Thus, we conclude that the electronic band structure is only weakly affected by strain due to the small curvature of the bent flakes.

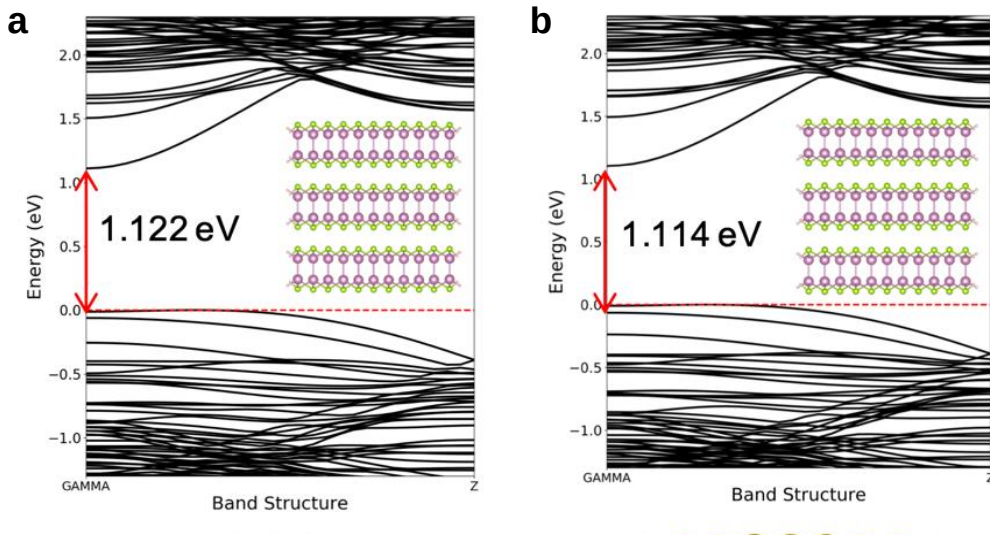

Figure 5.10 (a-b) Band structure of flat (a) and bent (b) tri-layer InSe, bent along one direction with a curvature corresponding to the maximum curvature observed experimentally. The band gap energy is marked by red arrows.

Furthermore, we examined the role of the geometrical shape of the flake on the strength of optical transitions. For unbent InSe, the band-edge absorption dipole couples only weakly with light polarized in the layer plane, *i.e.* for an electric field dipole **E** perpendicular to the *c*-axis (**E**⊥**c**).[39,40,98] Spin-orbit coupling (SOC) makes possible this coupling by mixing p_{xy}-orbitals with p_z-

orbitals in the valence band.[39] Hence, due to the preferential coupling of the electronic states to light polarized along the *c*-axis, *i.e.* for **E**||**c**, optical transitions are very sensitive to the bending of the flakes.

To account for this effect, we considered a simple model for the PL emission. The relationship between the intensity of the PL signal, I_{PL}, at the band gap energy E_g and that of the exciting radiation of intensity I_{ex} and energy E_{exc} can be written as

$$I_{PL}(E_{exc}, E_g) = P_{abs}(E_{exc}) \cdot P_{rel}(E_{ex}, E_g) \cdot P_{em}(E_g) \cdot I_{ex}(E_{exc}). \qquad (5.1)$$

Here, $P_{abs}(E_{exc})$ is the probability that a photon of energy E_{exc} is absorbed by the InSe layer; $P_{rel}(E_{exc}, E_g)$ is the probability that photogenerated electron-hole pairs relax towards the band edge states giving rise to the emission of photons of energy E_g, and $P_{em}(E_g)$ is the probability that photons of energy E_g are emitted after relaxation. We assume $P_{rel}(E_{exc}, E_g) = 1$. Since $P_{abs}(E_{exc})$ and $P_{em}(E_g)$ are proportional to the absorption coefficient $\alpha(E_{exc})$ and $\alpha(E_g)$, we calculated the dependence of α on the photon energy, *E*, and on the orientation of the electric field dipole, *e.g.* **E**⊥**c** and **E**||**c**. We expressed the optical absorption coefficient as $\alpha(E) = \frac{2\pi Im\varepsilon(E)}{\eta\lambda}$, where $Im\varepsilon$ is the imaginary part of the dielectric function, η is the refractive index and λ is the photon wavelength.

We calculated $Im\varepsilon$ using first-principles calculations of the electronic band structure at highly dense *k*-points in the Brillouin zone with the inclusion of spin-orbit coupling (SOC) *i.e.* the interaction between particle's spin and orbital motion. **Figure 5.11a-b** shows the *E*-dependence of $Im\varepsilon$ for **E**⊥**c** (Figure 5.11a) and **E**||**c** (Figure 5.11b) for InSe layers of different thicknesses. For **E**⊥**c**, $Im\varepsilon$

increases with increasing E, more strongly for $E > 4$ eV; only a weak increase of $Im\varepsilon$ can be seen at the band gap energy, E_g. For **E**||**c** (Figure 5.11b), the value of $Im\varepsilon$ is significantly enhanced compared to **E**⊥**c**.

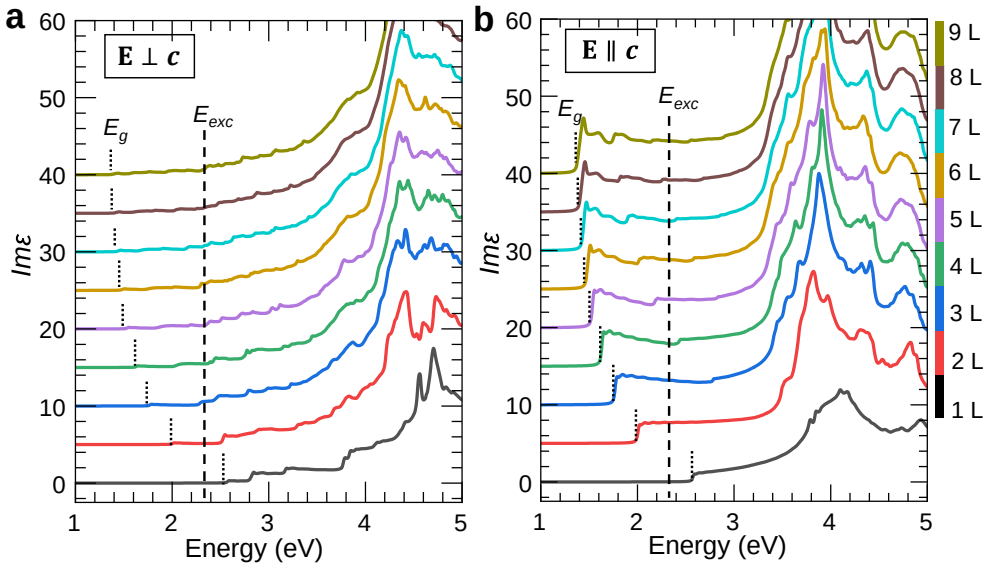

Figure. 5.11. (a-b) Imaginary part of the dielectric function, $Im\varepsilon$, for an electric field dipole **E** perpendicular **(a)** and parallel **(b)** to the c-axis. Different curves correspond to InSe layer thicknesses from t = 1 layer to t = 9 layers. The band gap energy and excitation energy are labelled as E_g and E_{exc}, respectively.

Figure 5.12a sketches the orientation of the layers with respect to the incident light. The component of the absorption coefficient coupled to light polarized in the layer plane is defined as α^{eff}. The value of α^{eff} within (α_{on}^{eff}) and outside (α_{out}^{eff}) a pillar can be expressed as $\alpha_{on}^{eff} = cos\theta\alpha_{\perp} + sin\theta\alpha_{\parallel}$ and $\alpha_{out}^{eff} = \alpha_{\perp}$, where $\alpha_{\perp}$ and $\alpha_{\parallel}$ are the absorption coefficients for **E**⊥**c** and **E**||**c**, respectively, and θ is the bending angle. The value of θ for the bent flakes in Figure 1 varies from 0 to ~ 9°. Correspondingly, the ratio $\alpha_{on}^{eff}/\alpha_{out}^{eff}$ increases from 1 for θ = 0 to ~3 for θ ~ 9°. We used equation (5.1) to model the PL enhancement (I_{on}/I_{out}) on the bent flakes and calculated I_{on} by integrating

α_{on}^{eff} over the curved surface of the flakes. For the unbent flake, we calculated I_{out} by integrating α_{out}^{eff} on a flat surface with an area equals to that of the bent one. Thus, we obtain:

$$I_{on}/I_{out} = C_1 + C_2 R(E_g) R(E_{exc}) + C_3[R(E_g) + R(E_{exc})], \qquad (5.2)$$

where, $R(E_g) = \alpha_{\parallel}(E_g)/\alpha_{\perp}(E_g)$, $R(E_{exc}) = \alpha_{\parallel}(E_{exc})/\alpha_{\perp}(E_{exc})$ and C_1, C_2 and C_3 are numerical coefficients.

Figure 5.12b shows the thickness *t*-dependence of $R(E_g)$ and $R(E_{exc})$. For E_{exc} = 2.33 eV, the largest enhancement of $R(E_{exc})$ is observed for *t* = 2 layers (*R* ~ 20), significantly larger than for *t* = 9 layers (*R* ~ 6). This indicates a stronger photon absorption in the bent flakes, which is in agreement with the enhanced Raman signal observed in our experiment. In contrast, $R(E_g)$ tends to increase with increasing *t* from $R(E_g)$ ~ 8 for *t* = 2 layers to $R(E_g)$ ~ 21 for *t* = 9 layers. Using equation (5.2) and the calculated energy dependences of $R(E_{exc})$ and $R(E_g)$, we derived the dependence of I_{on}/I_{out} on *t* for E_{exc} = 2.33eV (as used in the experiment) and a range of layer thicknesses *t* ranging from 2 to 9 layers, as shown in **Figure 5.12c**.

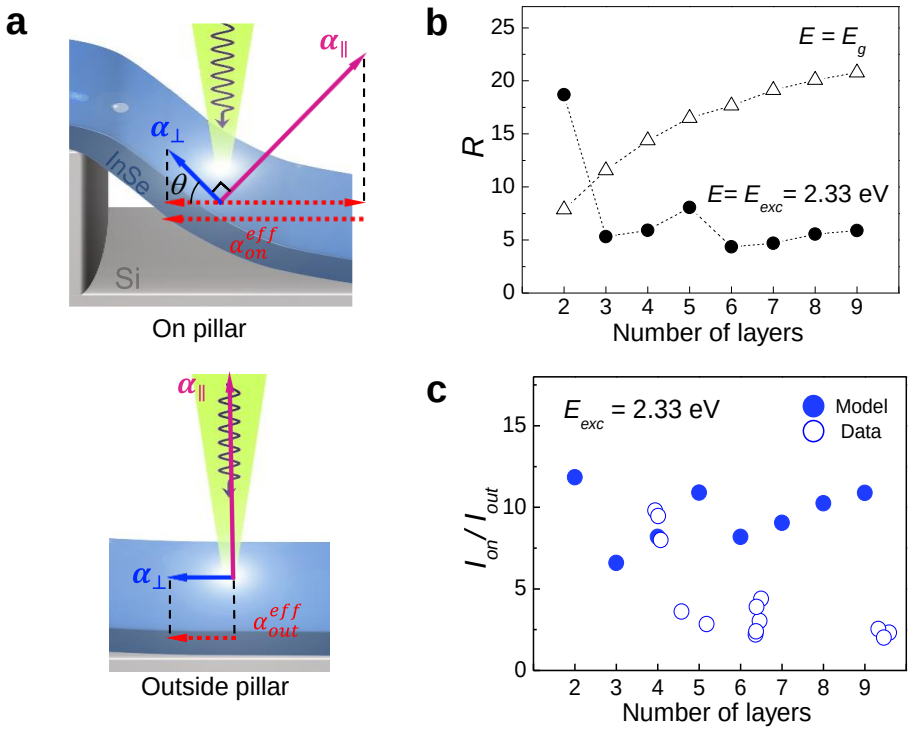

Figure 5.12 (a) Schematic of how the effective absorption coefficient α^{eff} for light polarized in the layer plane (*ab*-plane of the crystal lattice, *i.e.*, $\boldsymbol{E}\perp\boldsymbol{c}$) is enhanced on the pillar region (α_{on}^{eff}) compared to the region outside the pillar (α_{out}^{eff}). The values of α for $\boldsymbol{E}\perp\boldsymbol{c}$ and $\boldsymbol{E}\parallel\boldsymbol{c}$ are $\alpha_{\perp}$ and $\alpha_{\parallel}$, respectively. **(b)** Thickness *t*-dependence of $R(E_g)$ and $R(E_{exc})$. **(c)** Calculated and measured dependence of the photoluminescence enhancement ratio, I_{on}/I_{out}, on the number of InSe layers (E_{exc} = 2.33 eV).

Due to the small curvature of the bent flakes (*i.e.* the bending angle, θ, for our bent flakes is always less than 9°), in the analysis of the PL intensity, we neglect any change of collection efficiency of the emitted photons compared to that for unbent layers. Our model predicts an enhancement of the PL signal, which is of the same order of magnitude as measured in our experiment. Furthermore, the corresponding enhancement of the Raman signal is in line with the larger optical absorption in the bent layers (Figure 5.9d). The deviation of the model from the data for larger *t* may arise from the contribution of light

scattering around the edges of the pillars and limitations of our model, which does not consider disorder effects. In particular, the band edge recombination is very sensitive to the layer thickness due to quantum confinement and strong interlayer coupling in the InSe nanosheets.[28,31]

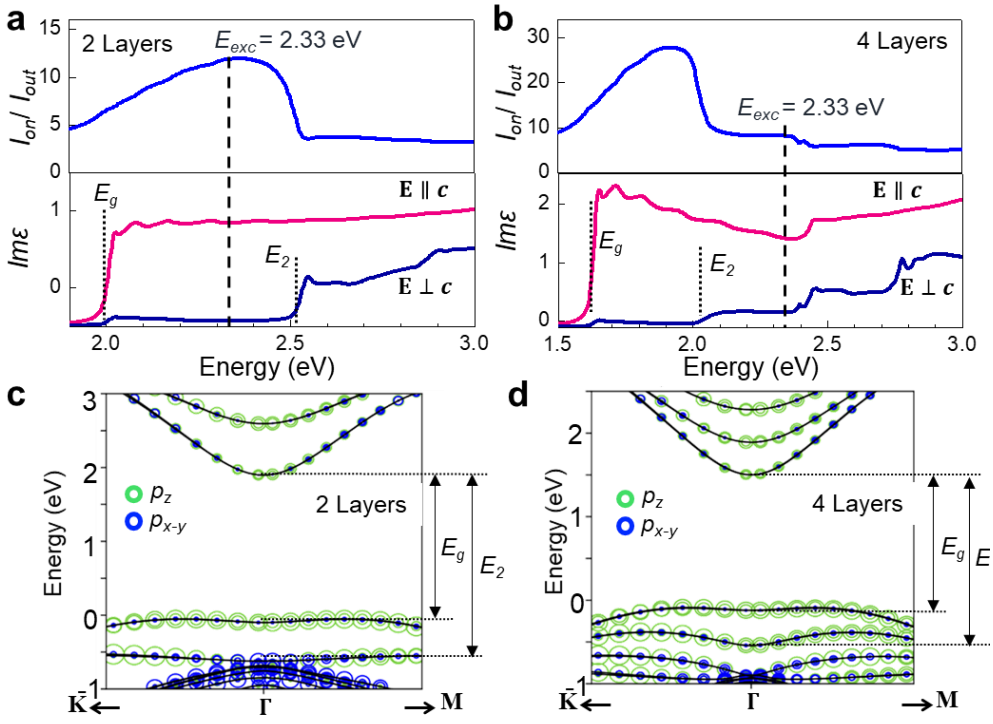

Figure 5.13 (a-b) Calculated photoluminescence enhancement, I_{on}/ I_{out}, as a function of the photon excitation energy for 2 (a) and 4 (b) InSe layers and corresponding dependence of $Im\varepsilon$ for **E**||**c** and **E**⊥**c** in the same energy range. The band gap energy, E_g, and the energy of the optical transition between the conduction band minimum and the second valence band edge, E_2,are indicated by black vertical dash lines. The excitation energy E_{exc} = 2.33 eV used in the experiment is indicated by a vertical dash line crossing all curves. **(c-d)** Projected band structure with p_z and p_{x-y} orbitals of 2 (c) and 4 (d) InSe layers. The p_z and p_{x-y} orbital components are represented in green and blue, respectively. The E_g and E_2 transitions are marked by arrows.

The PL enhancement on the bent flakes, I_{on}/ I_{out}, depends on the photon excitation energy, E_{exc}. This can be understood by considering the dependence

of I_{on}/ I_{out} on E_{exc} for different layer thicknesses. **Figure 5.13a-b** shows the calculated dependence of I_{on}/I_{out} on E_{exc} for 2 and 4 InSe layers and the corresponding values of $Im\varepsilon$ for **E**||**c** and **E**⊥**c** within the same energy range. It can be seen that a strong PL enhancement is observed over an energy range between the band gap E_g, and E_2. As shown in **Figure 5.13c-d**, E_2 corresponds to the energy of the optical transition between the CB minimum and the second VB maximum. Whereas the states of the VB maximum are made predominantly of p_z-orbitals, states from the deeper VB comprise of p_{x-y}-orbitals. Thus, optical transitions with $E_g<E_{exc}<E_2$ are most favourable for **E**||**c** and hence most affected by bending the layers. In particular, excitation energy from E_g to E_2 results in the strongest PL enhancement. This is realized experimentally in our 3 layers ($t \sim 2$ nm) InSe flake revealing a large value of $I_{on}/I_{out} \sim 10$ for $E_g<E_{exc}<E_2$.

5.5. Comparing InSe with TMDCs

The spatial modulation of the PL emission from InSe over the Si-pillars is qualitatively different from that reported for single and bi-layer TMDCs.[155-163] In TMDCs sharp emission lines were observed at low-temperature and assigned to the recombination of excitons from localized states. These arise from crystal defects, non-homogeneous strain and/or nano wrinkles intentionally created by exfoliating and/or transferring the TMDCs onto nanopillars, rough metallic surfaces coated with dielectrics, and/or created by intentionally structural damage of the layers. As shown in Figure 5.5, for InSe the modulation of the PL signal over the pillars occurs at room temperature, but the PL peak energy and linewidth do not change significantly. Thus, we exclude a dominant localization of the exciton in the layer plane due to the pillars and/or an exciton funnel effect, as observed in TMDCs.[155]

Also, we exclude that our observations arise from a photonic cavity effect, as reported in WSe_2 layers coupled to dielectric nano-antennas.[164] Optical resonances can occur when light interacts with sub-wavelength dielectric cavities and were reported in vertical, small aspect-ratio and subwavelength Si-pillars.[165] To probe photonic cavity effects, we measured the μ-Raman scattering intensity of the Si-line (~ 520 cm^{-1}). The μ-Raman spectra within and outside individual Si-pillars within the array were acquired under the same excitation conditions as used for InSe. The Raman scattering enhancement was found to be 1.3 ± 0.5. Representative spectra are shown in **Figure 5.15a.** Futhermore, we have examined the PL enhancement ratio for InSe flakes transferred onto nanopillars of different height h = 60 and 120 nm (**Figure 5.15b**). The PL enhancement for flakes transferred on shorter nanopillars tend to become weaker due to the reduced bending angle.

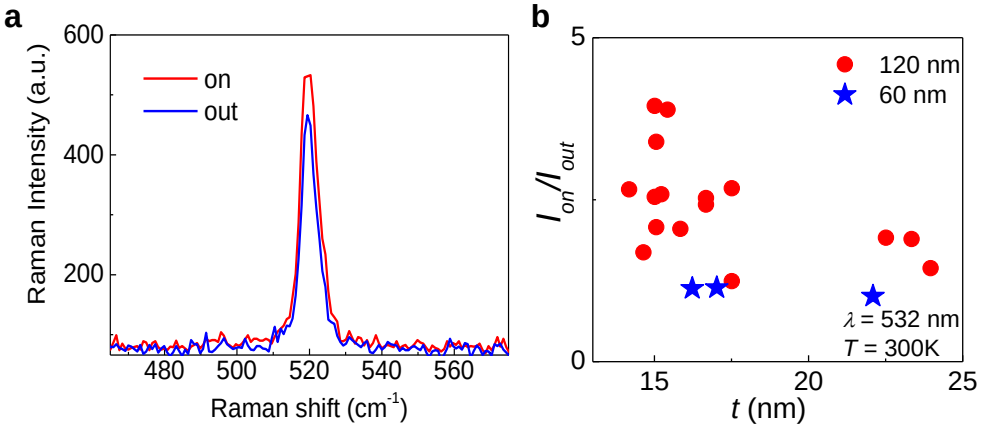

Figure 5.15 (a) Room-temperature (T = 300K) Raman spectra inside and outside a representative Si-pillar within the array (λ = 532 nm, P = 10^{-6} W). **(b)** PL enhancement ratio for InSe flakes transferred onto pillars of different height (h = 120 nm and 60 nm).

In previous work, Gisbert *et al.* reported an enhanced optical emission from InSe flakes exfoliated onto agglomerates of SiO_2 nanoparticles.[40] The

measured enhancement of the optical emission was explained by the combined effect of light scattering by the nanoparticles and anisotropic light-matter interactions. Although this surface texturing approach represents a promising strategy for controlling optical signals, the use of randomly distributed nanoparticles to texture a 2D layer is difficult to reproduce and quantify. Our data and analysis for InSe layers bent onto Si-pillars reveal that the orbital symmetry of the band-edge states and light polarization dipole selection rules play the main role in the enhancement of the optical signal. This is a reproducible effect that is strongly dependent on the geometrical shape and thickness of the bent layers.

5.6. Summary

We have demonstrated the deterministic positioning of 2D InSe flakes of different thicknesses onto a periodic array of Si-pillars. We have shown a reproducible bending of the layers, which causes a nanoscale spatial modulation of the Raman and photoluminescence signals across the array. Density functional theory-based calculations were used to model the measured effects and account for the role of the geometrical shape and strain of the flake on the electronic states and light polarization properties. While the strain plays a negligible role in our flakes due to their small curvature, the geometrical shape significantly modifies the integrated light emission intensity, which can be understood by taking into account the orbital symmetry of the band-edge states and light polarization dipole selection rules. Our data and analysis indicate a route towards the controlled modulation of optical properties by bending the flakes, which is dependent on the layer thickness, optical excitation energy and

light polarization. The proposed integration of 2D InSe with Si nanostructures for optoelectronics exploits the flexibility of InSe and its compatibility with Si.

Chapter 6

Resonant tunnelling into the two-dimensional subbands of InSe layers

This chapter reports on a novel type of tunnel field-effect transistor (TFET) based on a two-dimensional (2D) InSe van der Waals (vdW) crystal sandwiched between two multi-layered graphene (MLG) electrodes. This type of vertical FET exhibits multiple regions of negative differential conductance (NDC) peaks in the current-voltage characteristics and differs in several essential aspects from TFETs based on vdW crystals reported earlier. Furthermore, intersubband transitions of individual InSe layers or repeated multi-layered stacks could be exploited in photon sources and detectors, as discussed in Chapter 7.

For the experiments, InSe based TFETs were fabricated by Dr. James Kerfoot and Dr. Zakhar Kudynskyi. Transport measurements and optical studies (further described in chapter 7) of the devices were performed by Dr. Zakhar Kudynskyi, Dr. E.E. Vdovin, and myself. Dr. Mark Greenaway and Prof. Amalia Patanè developed theoretical models to describe the transport properties of the devices. The results presented in this chapter were published in *Communications Physics* **3,** 16 (2020).

6.1. Introduction

Despite the transformative success of Si-based devices, there are limits to their miniaturization and functionalities. Thus, 2D vdW crystals have attracted considerable interest for digital electronics beyond Si-based CMOS

technologies. Heterostructures based on 2D vdW crystals[7,103,143] such as graphene, hexagonal boron nitride (hBN), and metal mono- (*e.g.* InSe, GaSe…) and di-chalcogenide (*e.g.* $SnSe_2$, MoS_2…) layers have physical properties that may overcome some of the technological limitations of traditional covalent semiconductors.[166] Beyond their versatility for a wide range of band structure-engineered devices by stacking and/or twisting the layers, these structures can also be readily transferred onto substrates that are compatible with the well-established CMOS device fabrication processes used in modern integrated circuits for digital logic, image sensors, transceivers, *etc*. In recent years, different types of TFETs based on vdW crystals have emerged, stimulating research of fundamental and applied interest.[66,105,119-121,125,167-169] These devices include the graphene/insulator/graphene TFET with a region of NDC in the current-voltage characteristics due to resonant tunnelling.[105] Similar TFET structures based on TMDCs rather than graphene layers have also been suggested and studied theoretically, revealing improved transport characteristics due to qualitative differences in the band structure of these materials compared to graphene.[119] Furthermore, Esaki-type tunnel diodes[125] have demonstrated the potential of 2D materials for transistors with a low threshold swing and NDC by band-to-band tunnelling of carriers through the forbidden energy gap of a vdW heterojunction.[167-169]

Here we report on a different type of TFET that exhibits multiple regions of NDC. These device structures exploit the tunnelling of charge carriers from a source of electrons into the distinct 2D subband states of an InSe vdW crystal a few atomic layers thick. The energy of the 2D subbands can be tuned by the thickness of the InSe layer due to the strong quantum confinement of the light

effective mass electrons.[31] By applying a voltage, V_{sd}, across two multi-layer graphene (MLG) electrodes, which serves as the source (*s*) and drain (*d*) electrodes to the InSe layer, the chemical potential in the source can be tuned in and out of resonance with a given 2D subband, leading to a peak in the current-voltage (I-V_{sd}) characteristics and a region of NDC. Multiple regions of NDC can be thus induced by tunnelling into consecutive 2D subbands of InSe, whose number increases with the number of InSe layers. In addition to their potential use for digital electronics, InSe-based TFETs could aid the development of optical emitters and detectors by the exploitation of intersubband transitions of individual InSe layers or repeated multi-layered stacks.

6.2. Resonant tunnelling transistors with negative differential conductance

Figure 6.1a illustrates the schematic of a typical device fabricated by sequential stamping of hBN, MLG, InSe and MLG flakes by an all-dry viscoelastic transfer technique, as described in chapter 4. The top hBN flake encapsulates the whole heterostructure and prevents it from contamination during long-term exposure to air. An optical image of a typical device is shown in **Figure 6.1b.** In this particular device, the InSe layer has an in-plane area of about 100 μm^2 and thickness $t \sim 8$ nm (10 layers). Several TFETs were fabricated by varying the thickness of the sandwiched InSe layer. A voltage (V_{sd}) is applied to the top MLG-electrode relative to the bottom to align different 2D subbands of InSe to the chemical potential in the source. The Si-substrate serves as a gate electrode and the gate voltage, V_g, is used to adjust the chemical potential in the adjacent/bottom MLG. The quality of the surface and underlying interfaces were characterized by AFM. **Figure 6.1c** shows an AFM image of the TFET shown

in Figure 6.1b, including layers of MLG/InSe/MLG/hBN. Following the transfer, small quantities of PDMS residues are found at the surface of each transferred flake, including MLG on hBN. Surfaces exhibit a root mean square roughness of 0.31 nm.

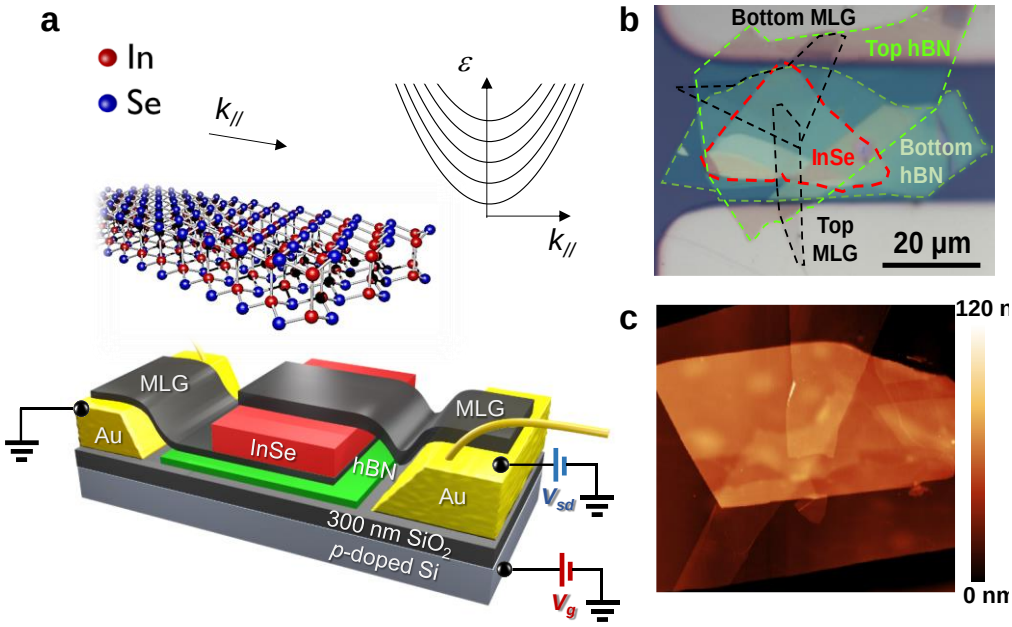

Figure 6.1(a-b). Schematic diagram and optical image of an InSe-based TFET constructed by dry transfer of individual layers of InSe, hBN and MLG onto a SiO_2/Si substrate. The top insets show the crystal structure of single-layer InSe and the in-plane energy dispersion of the two-dimensional (2D) InSe subbands. **(c)** AFM image of a typical device demonstrating the quality of the surface and interfaces.

Figure 6.2a shows the current-voltage I-V_{sd} curve at a measurement temperature, T = 2.0 K, and V_g = 0. For $|V_{sd}| \lesssim 0.5$ V, the tunnel current remains small (< 10 pA) for both positive and negative applied voltages. However, for $V_{sd} > 0.5$ V, the current increases rapidly and the I-V_{sd} curve reveals a sequence of resonant features. Pronounced peaks in the I-V_{sd} can be seen over an extended range of V_{sd} and are followed at a higher bias ($|V_{sd}| > 1.1$ V) by weaker

resonances. These resonances are labelled as S_1, S_2... in Figure 6.2a and can be seen more clearly in the differential conductance plot, $G = dI/dV_{sd}$, shown in **Figure 6.2b**.

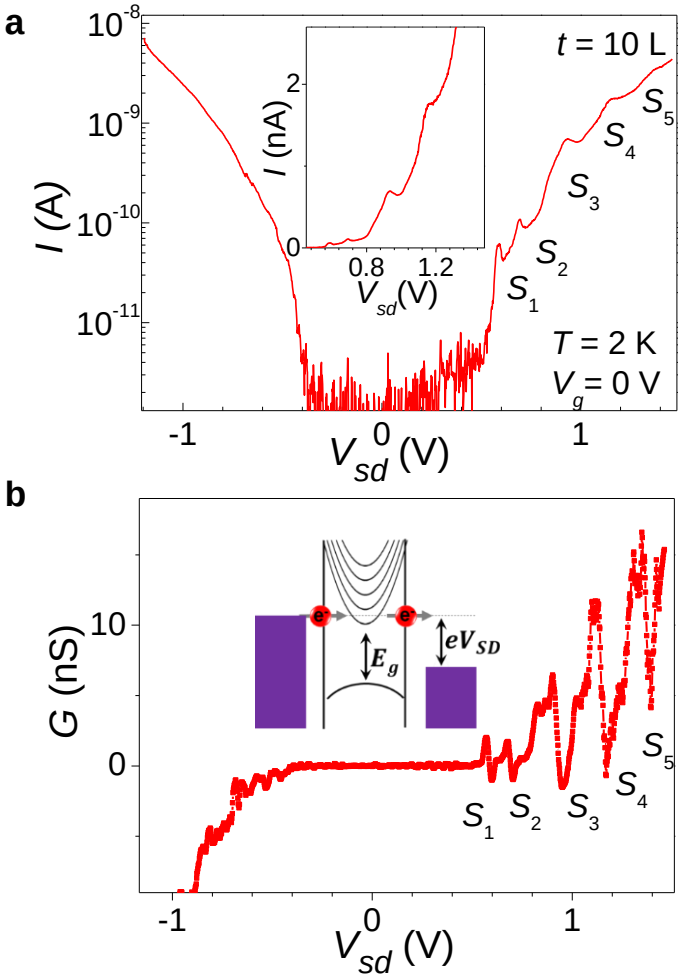

Figure 6.2(a) Current-voltage, I-V_{sd}, characteristics of a TFET with 10-layers (10L) InSe at a gate voltage V_g= 0 V and temperature T = 2 K. Inset: Zoom in of the I-V_{sd} curve in forward bias. **(b)** Differential conductance, G-V_{sd}, curve at V_g= 0 V and T = 2 K. The inset sketches the tunnelling of electrons from a MLG-electrode (source) into the 2D subbands of InSe.

We attribute each resonance to the threshold of resonant tunnelling through a quantized 2D subband of the InSe layer when the energy of the subband minimum aligns with the chemical potential of the MLG-source

electrode (inset Figure 6.2b). The asymmetry of the I-V_{sd} curve with respect to positive and negative voltages suggests that the two interfaces of the InSe with the two MLG-electrodes are different. The resonances can be observed more clearly when electrons tunnel from the bottom to the top MLG ($V_{sd} > 0$), suggesting that the InSe layer forms a cleaner interface with the bottom MLG. This asymmetry is likely to arise from the lower quality of the top surface of InSe, which tends to be more contaminated than the bottom surface due to the use of polymer stamps for the exfoliation of InSe. The resonances are observed over a wide temperature range, as shown in **Figure 6.3a-b**. On increasing the temperature from T = 2K to 300K, they shift to lower values of V_{sd} and tend to broaden; they cannot be resolved clearly at T = 300K (inset of Figure 2a). This phenomenon is further discussed in section 6.5.

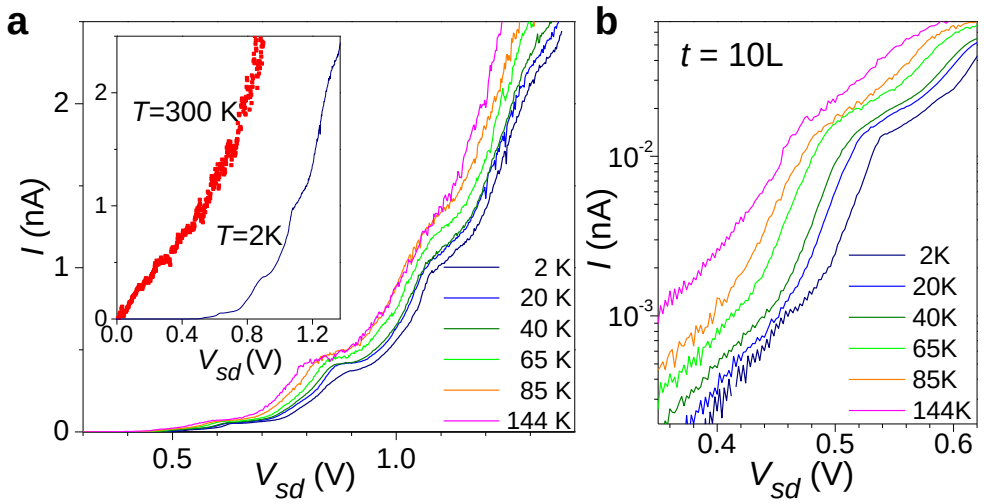

Figure 6.3.(a) Current-voltage characteristics, I-V_{sd}, of a TEFT with 10-layers InSe at a gate voltage V_g = 0 V and at different temperatures T. The inset compares the I-V_{sd} curves at T = 300 K and 2 K. **(b)** I-V_{sd} curves in the low voltage region.

6.3. Tunnelling into the two-dimensional subbands of InSe

InSe-based devices can be fabricated with different thicknesses, *t*, of the InSe layer and hence with different subband energies. **Figure 6.4a** shows the *t*-dependence of the energy minima of the InSe subbands assuming that the electrons are confined by a square quantum well (QW) potential of infinite height, *i.e.* $E_n = n^2h^2/8t^2m_c^e$, where *n* is an integer, m_c^e= 0.08 m_e is the electron effective mass for motion along the *c*-axis in bulk InSe,[53] and m_e is the free electron mass. The calculated energy separation, $\Delta E_{2\text{-}1}$, between the lowest two subbands decreases from hundreds of meV to a few meV with increasing *t* from 2 to 20 layers. **Figure 6.4b** shows the corresponding *t*-dependence of the band-edge exciton recombination energy, *i.e.* $E_X = E_X^{3D} + h^2/8t^2\mu_c^{ex}$, where E_X^{3D} = 1.25 eV is the value of E_X for bulk InSe at *T* = 300 K, $\mu_c^{ex} = 1/[1/m_c^e + 1/m_c^h]$ is the reduced exciton mass, and m_c^h= 0.17 m_e is the hole effective mass.[152] Similar dependences of E_X and $\Delta E_{2\text{-}1}$ on *t* were predicted by density functional theory (DFT),[33,40,170] with larger deviations from the QW model observed at smaller *t*.[26] We measured the I-V_{sd} characteristics of three devices with different InSe layer thicknesses, as estimated from the photoluminescence (PL) spectra of these three samples at *T* = 300K (inset of Figure 6.4b). The PL peak energy is due to the band-edge exciton[26,38,171] and is very sensitive to the layer thickness. **Figure 6.4c** shows the I-V_{sd} and G-V_{sd} curves of these three devices, revealing that the current and voltage spacing between consecutive resonances increases with decreasing *t*. We note that no resonances were observed in the TFET with *t* = 19 layers or in other TFETs with thicker layers.

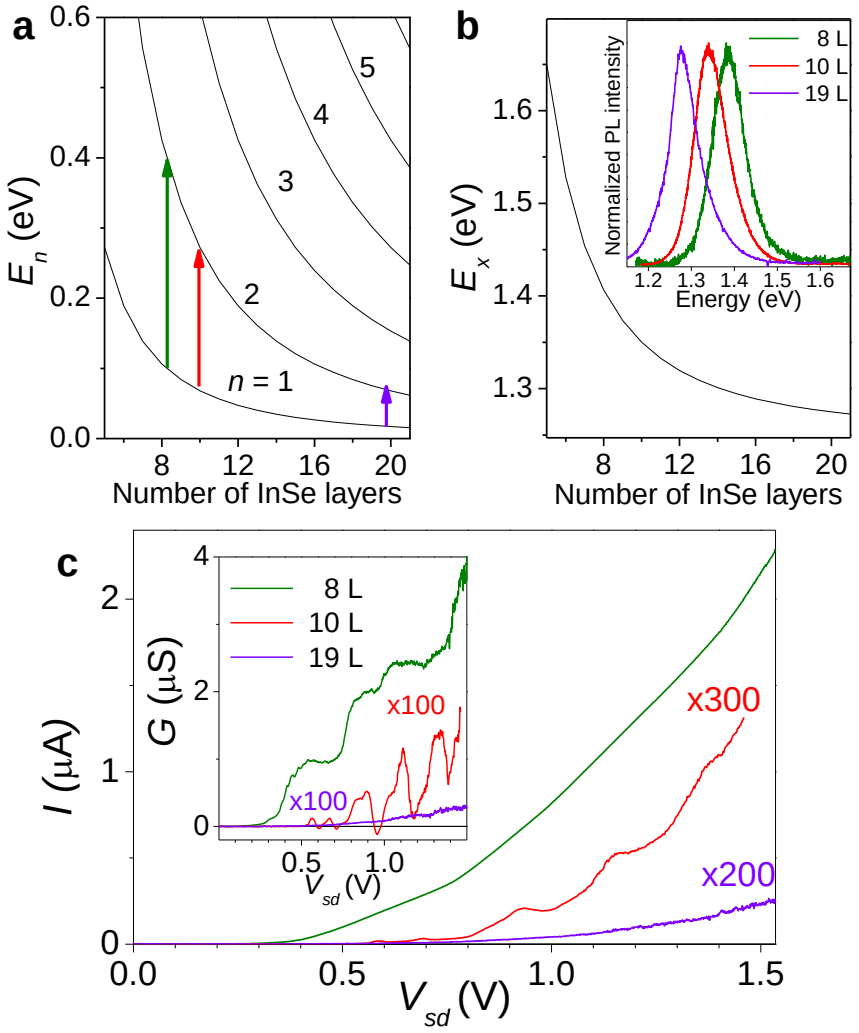

Figure 6.4(a-b). Dependence of the subbands and exciton recombination energies on the number of InSe layers. The arrows in part (a) show the energy spacing between the lowest two subbands for three specific layer thicknesses (t = 8, 10 and 19 layers). The inset in part (b) shows the normalized photoluminescence (PL) spectra of TFETs at T=300 K. **(c)** I-V_{sd}, characteristics of TFETs with different InSe layer thickness at the gate voltage V_g = 0 V and T = 2 K. Inset: differential conductance, G-V_{sd}, plots.

Figure 6.5a shows the current-voltage characteristic for a device with a relatively thicker InSe layer (t = 22 layers). It demonstrates a distinct temperature dependence: the current exhibits a thermally activated behaviour. **Figure 6.5b** shows the dependence of I on T for T > 100K. The fit to the data by an Arrhenius-

like plot gives an activation energy E_a ~ 0.04 eV. This is close to the binding energies of native shallow donors and acceptors states in bulk-InSe, suggesting a thermal emission of electrons from localized states as the mechanisms for the increase of I with increasing T.[151,172]

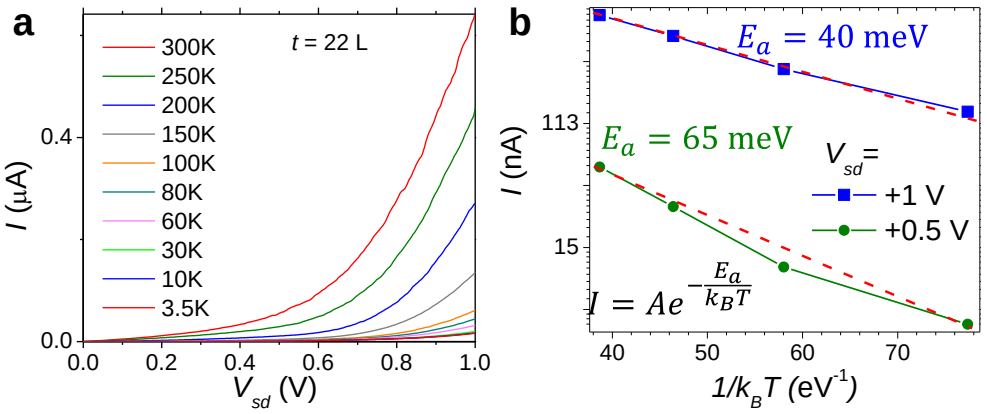

Figure 6.5 (a) Current-voltage characteristics, I-V_{sd}, of a TEFT with 22-layers InSe at a gate voltage V_g = 0 V and different temperatures T. **(b)** Dependence of the current I on T at high temperatures (100-300K) and V_{sd} = 1V and +0.5 V.

6.4. Probing the energy spacing between 2D subbands

To estimate the energy spacing between the 2D subbands, we examine the V_g-dependence of the main conductance peaks S_1, S_2, S_3… in the device with 10-layers InSe. As shown in **Figure 6.6a**, an increase of V_g decreases the V_{sd}-position of these peaks. This behaviour can be seen more clearly in the $G(V_{sd}, V_g)$ colour map of **Figure 6.6b**. Here, the dashed black lines illustrate that for sufficiently large applied gate voltage, all the S_n-resonances exhibit a similar shift (*e.g.* dV_{sd}/dV_g ~ 0.005).

As shown in Figure 6.6a for the TFET with t = 10 layers, at V_g ~ +20 V, a narrow resonance, R, emerges at V_{sd} ~ +0.5 V. This can be seen more clearly in the $G(V_{sd}, V_g)$ colour map of Figure 6.6b. Here the white lines highlight the

shift and splitting of the narrow *R*-resonance. The emergence of this additional narrow feature in the transport characteristics of our devices is similar to recent observations of resonant electron tunnelling through localized states due to defects in hBN.[171] The stronger dependence of R on V_g ($dV_{sd}/dV_g \sim 0.05$) compared to that of S_n ($dV_{sd}/dV_g \sim 0.005$) suggests that R arises from carrier tunnelling into the states of a localized defect close to the bottom gate electrode. Similar narrow resonances can be seen in the same device under negative applied gate voltages and $V_{SD} \sim +1.0$ V.

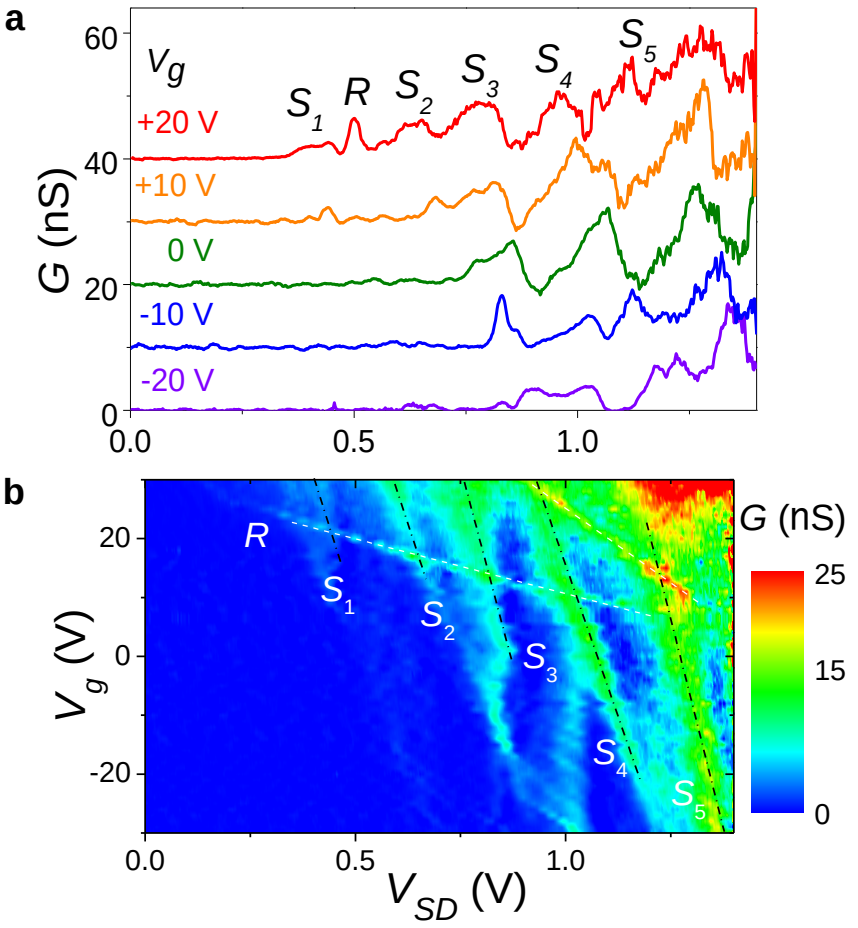

Figure 6.6 (a) Differential conductance, G-V_{sd}, curves at different gate voltages, V_g, at a temperature T = 2K for a TFET with 10-layers InSe (curves are offset for clarity). **(b)** Colour map of G versus V_{sd} and V_g at T = 2K. Black and white lines identify different resonances.

The spacing between the first two resonances S_1 and S_2 is ΔV_{sd} ~ 0.2 V at V_g = + 30V and coincides with the calculated energy spacing $\Delta E_{1\text{-}2}$ between the lowest electron energy subbands of InSe (Figure 6.4a). Decreasing the layer thickness from 10 to 8 layers increases ΔV_{sd} from ~ 0.2 V to ~ 0.3 V (Figure 6.4c). As can be seen in Figure 6.4a, this is in agreement with the calculated energy spacing $\Delta E_{2\text{-}1}$, which increases from $\Delta E_{2\text{-}1}$ = 0.20 to 0.32 eV with decreasing t from 10 to 8 layers. Thus, our data suggest a leverage factor $f = e(dV_{sd}/dE) \approx 1$, where dV_{sd} is the incremental change of the applied voltage corresponding to a change in energy dE. This is in agreement with an estimate of the leverage factor as derived from a simple capacitance (C) model.

To estimate the leverage factor, $f = e(dV_{sd}/dE)$, we use $C = e[dn/dV_g] = \varepsilon\varepsilon_0/d$, which is the "classical" capacitance per unit area of the graphene/SiO_2/Si heterostructure, e is the elementary charge, d = 300 nm is the SiO_2 layer thickness, ε =3.9 is the relative dielectric constant of SiO_2, ε_0 is the permittivity of free space, and n is the carrier density in the MLG electrode. We relate the chemical potential E_F to n using the relation for graphene, *i.e.* $E_F = v_F h\sqrt{n/4\pi}$, where v_F =10^6 m/s is the Fermi velocity and E_F is measured relative to the Dirac point. Using this model, we derive:

$$f = \frac{4\sqrt{\pi}e^2 d}{\varepsilon\varepsilon_0 v_F h}\,\frac{dV_{sd}}{dV_g}\,\sqrt{n} \quad . \tag{6.1}$$

As shown in **Figure 6.7**, the leverage factor increases with increasing n and acquires a value of f = 1 for n ~ 10^{12} cm^{-2}. This value of the carrier density corresponds to an applied gate voltage of V_g= +15V (inset of Figure 6.7). We assume that this model can be applied to MLG as the energy dispersions of MLG are similar to those of graphene at high energy.[173]

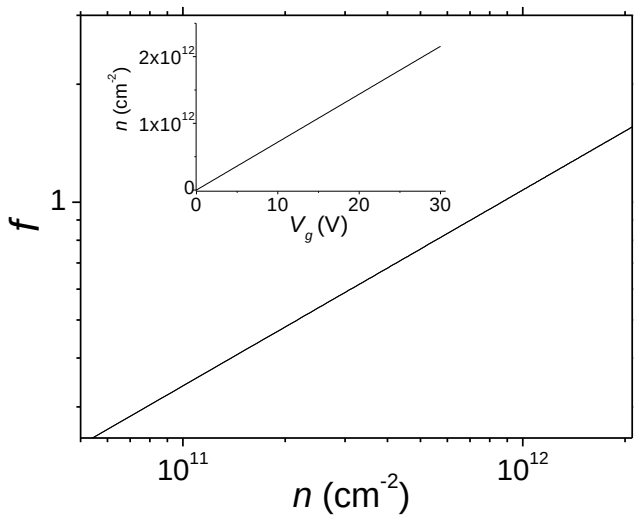

Figure 6.7. Leverage factor, *f*, versus the carrier density, *n*. The inset shows the dependence of *n* on the applied gate voltage V_g for single-layer graphene on conventional 300 nm SiO_2/Si substrate.

The InSe-based TFETs exhibit electroluminescence (EL) emission under a sufficiently large applied voltage V_{sd}. When a bias voltage, V_{sd}, is applied across the MLG-electrodes, the negative MLG-electrode fills with electrons and the positive MLG-electrode with holes. Above a critical bias, $V_{sd} > E_g/e$, where E_g is the energy gap of the InSe layer, electrons and holes are injected simultaneously into the conduction and valence bands of the optically active InSe region from the oppositely-biased electrodes, thus producing EL. **Figure 6.8a-b** show a typical EL spectrum (Figure 6.8a) and a colour map of the EL intensity versus voltage, V_{sd}, and photon energy, hv (Figure 6.8b). The EL emission is observed for $V_{sd} > 1.6$V. This corresponds to an energy separation between the chemical potentials in the MLG-source and MLG-drain of ΔE_F = 1.60 eV, close to the measured band gap energy of the InSe layer (E_g = 1.27 eV at T = 300K), as derived from the peak energy of the EL and PL spectra (Figure 6.8a).

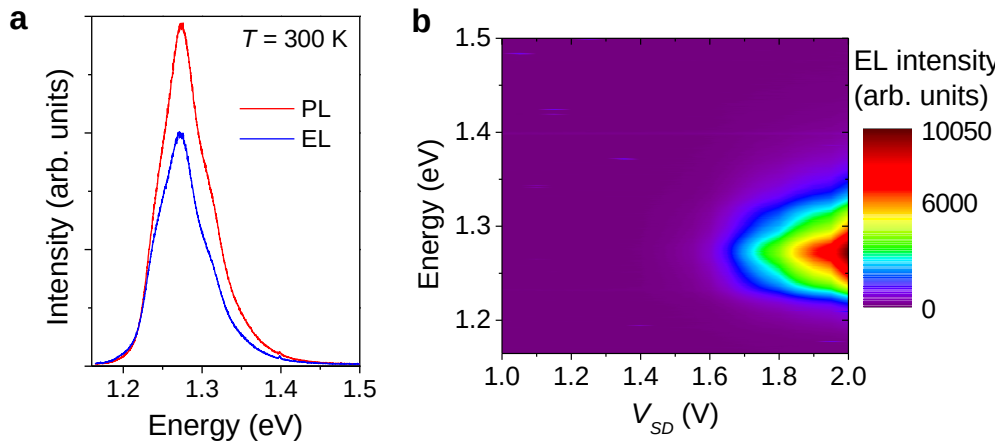

Figure 6.8 (a) PL and EL spectra of a TFET with 20-layers InSe at T=300 K (λ = 405 nm, P = 0.1 mW). The EL spectrum was measured at V_{sd} = 2 V. **(b)** Colour map of the EL intensity versus voltage, V_{sd}, and photon energy, hv, at T=300 K.

6.5. Modelling resonant tunnelling in TFETs based on InSe

Our TFETs with a few layers of InSe between two MLG electrodes differ in several important aspects from the well-established resonant tunnelling diodes based on heterostructures in which the crystal lattices of the component layers are aligned and lattice-matched. A typical example is the resonant tunnelling diode (RTD) in which two (AlGa)As tunnel barriers enclose a GaAs quantum well with the source and drain contacts composed of doped GaAs.[174] The GaAs-AlGaAs RTDs devices are ideally suited to conserve both the energy and momentum of the tunnelling carriers so that strong resonant peaks and extended regions of NDC with high peak-to-valley ratios are observed. A peak to valley ratio up to 3.8 is observed for these devices at room temperature (RT).[175] In our devices, the hexagonal lattices of InSe (a = 4.002 Å) and graphene (a = 2.46 Å) are strongly mismatched (~ 60%) and are not intentionally aligned. Furthermore, in undoped graphene and MLG the occupied states are located around the K and

K' points of the hexagonal Brillouin zone, whereas the conduction band edge of InSe is at the *Γ*-point (**Figure 6.9**).

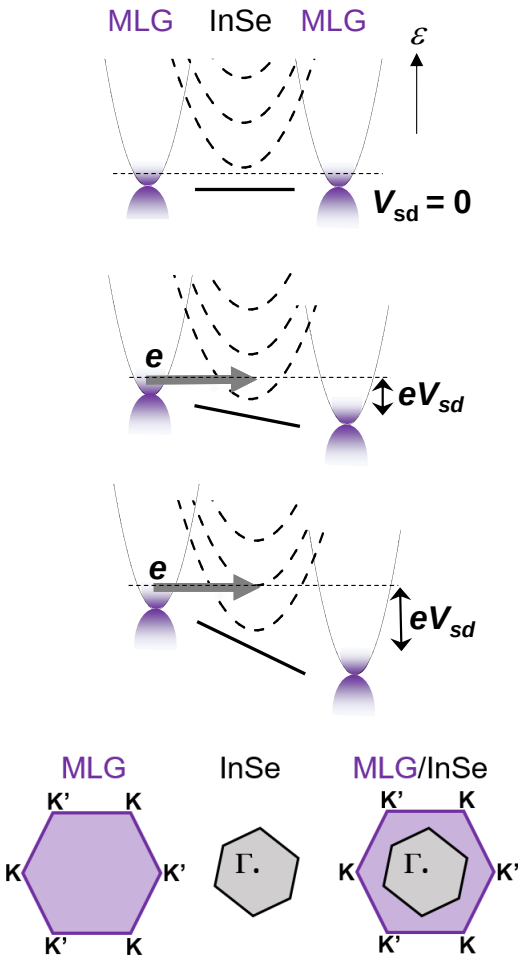

Figure 6.9 Schematic of tunnelling of electrons from a MLG-electrode (source) into the 2D subbands of InSe and into MLG (drain) for an increasing source-to-drain voltage, V_{sd}. Bottom inset: Brillouin zone of InSe and MLG.

Our devices also differ from graphene/hBN tunnel diodes in ref. [105]. The 2D InSe has much smaller band gap energy than hBN. The band alignment of InSe and hBN with respect to the Dirac points of graphene (or the conduction band of MLG) is also quite different. Whereas the energy of graphene's Dirac point lies almost in the middle of the band gap of hBN, it is positioned closer to the conduction band edge of InSe.[35] A MLG-InSe-MLG heterostructure, therefore, has a band alignment that takes the form shown

schematically in the inset of Figure 6.2b. By reducing the thickness of the InSe layer the energy gap of InSe can be increased, increasing the effective height of the InSe tunnel barrier. This also changes the number of 2D subbands and their energy spacing. Thus, in these TFETs the InSe layer thickness can control both the tunnelling rate of the charge carriers and the resonant enhancement of the current through 2D subbands whose energy position are very sensitive to quantum confinement. An additional feature of interest is that, despite the absence of a real tunnel barrier between the MLG and InSe layers, the subband states of the InSe layer are sufficiently well-defined to produce prominent resonant features in the current-voltage characteristics.

We now examine in more detail our MLG-InSe-MLG devices. For electron tunnelling from MLG to InSe, an electron must overcome the large momentum difference between the K-(K'-) and Γ-points. This can be provided by the scattering potential at the InSe-graphene interface due to the large lattice mismatch of the InSe and graphene layers, and/or disorder in the layers. This is analogous to the situation encountered in the previous studies[105] of almost-lattice matched graphene-hBN-graphene tunnel transistors in which the lattices of the graphene electrodes were misaligned. This misalignment gives rise to a difference between the in-plane momenta of the initial and final states of electrons tunnelling between the two graphene layers. In this case, the in-plane scattering allows energy-conserving resonant tunnelling to occur even when the wavevectors of the tunnelling electrons in the collector and emitter are different.[105] A moire` pattern potential for controlled twisted layers has the potential for engineering the tunnelling current in these devices.

Our measured region of NDC in the MLG–InSe–MLG heterostructures can be explained in terms of a similar model that uses a transfer matrix Hamiltonian formalism.[175] We consider the conservation of the energy and in-plane momentum of the tunnelling electrons. In the MLG layer the carriers around the Fermi energy are located close to the K-points of the Brillouin zone (BZ), whereas the conduction band minimum of InSe is at the Γ-point of its BZ. In order for the electrons to tunnel between the layers, they must overcome the large momentum difference between these two points. This momentum is provided by the scattering potential at the InSe-graphene interface due to the large lattice mismatch of the InSe and graphene layers, and/or disorder in the layers.

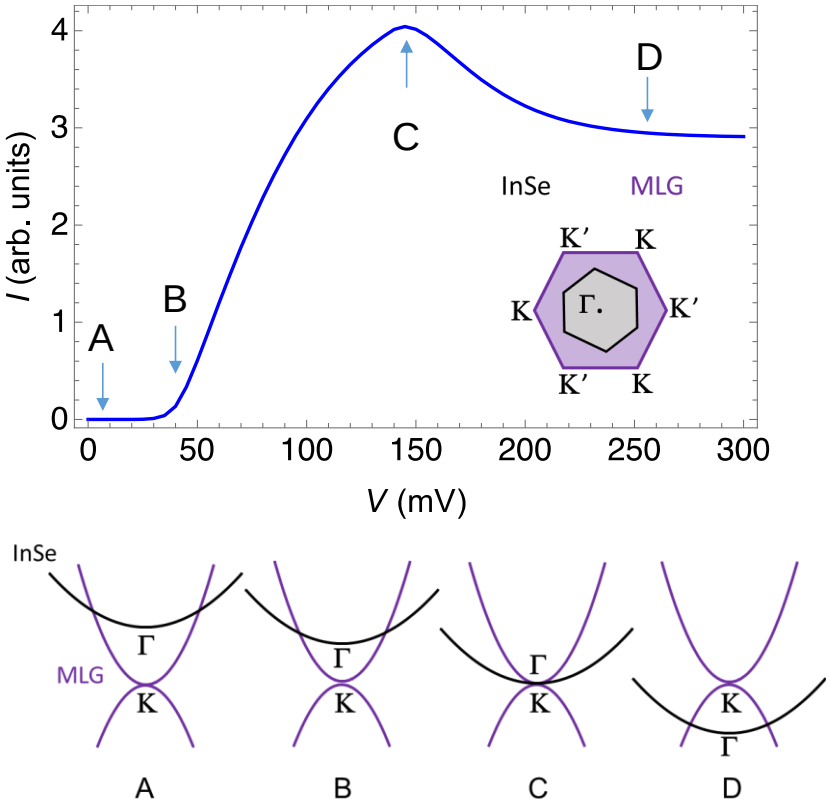

Figure 6.10. A model for negative differential conductance (NDC). Points A-B-C-D in the calculated *I*-*V* correspond to different bias conditions and therefore energetic alignments between the bands of the InSe and MLG. Inset: The Brillouin zones of angular misaligned InSe and MLG.

Figure 6.10 shows the calculated *I-V* curve and NDC region. The points A-B-C-D in the calculated *I-V* correspond to different bias conditions and therefore energetic alignments between the bands of the InSe and multi-layer graphene (MLG). In each plot at the bottom of Figure 6.10, the K-point of MLG is shifted to be at the same point in **k**-space as the Γ-point. Where the bands cross in this plot **q** = 0 and the tunnelling matrix element has a maximum. Here **q** is defined as $\mathbf{k_g} - \mathbf{k_I}$, where $\mathbf{k_I}$ is the electron wavevector in InSe measured with respect to Γ and $\mathbf{k_g}$ is the electron wavevector in MLG measured with respect to K. A detailed calculations can be found in ref [174].

The calculated *I-V* shows a region of NDC in qualitative agreement with our measurements. At low voltages (labelled A in Figure 6.10) the current is zero since the energy of a particular subband of the InSe layer lies above the chemical potential of the MLG source contact. Increasing *V* lowers the subband energy. When the subband is energetically aligned with the chemical potential of the MLG, a conduction channel opens and electrons can tunnel through the InSe barrier (B). A further increase of the voltage increases the number of states that can tunnel with $q \sim 0$, thus increasing the current. The states with the highest probability of tunnelling correspond to those in the schematics of Figure 6.10 where the MLG and InSe bands cross. At point C, the bottom of the InSe subband is energetically aligned with the bottom of the MLG conduction band. At this point the number of electrons that can tunnel from the MLG band into the InSe band with $q \sim 0$ is maximal and thus the current also has a peak at this voltage. Increasing the bias further decreases the number of tunnelling electrons with $q \sim 0$ and the current approaches a constant value (D) since there are always some electrons that can tunnel where the InSe and MLG bands cross. Thus,

electrons tunnel through the states of distinct InSe subbands or states with increasing in-plane momentum within the same subband. With increasing bias the tunnelling channel through a 2D subband remains open until a second subband becomes available. Although each 2D subband should produce a distinct peak in I-V_{sd}, the overlapping contributions from different subbands increase the valley current, giving rise to a steadily increasing monotonic background current. Thus, with increasing voltage above the first few 2D subband peaks, the resonances in I-V_{sd} become less well-resolved.

Finally, we attribute the temperature dependence of the differential conductance peaks (Figure 6.3) to the thermal broadening of the electron distribution around the Fermi energy in the MLG-source and to phonon-assisted tunnelling. The energy of the optical phonon modes in InSe is in the range 14-30 meV.[176] When these lattice vibrations are thermally activated, they inelastically scatter the tunnelling electrons. In turn, this broadens the resonances and shifts their position to lower voltages with increasing T (Figure 6.3). Elastic scattering mechanisms also influence the tunnel current. This can vary from sample to sample due to inhomogeneous scattering sites, local electric fields arising from surface dipoles due to the local atomic structure and charge distribution at the surface of the layers.

6.6. Summary

We have realized vertical tunnel transistors with an InSe layer between two multi-layer graphene contacts. Within the extensive family of vdW crystals, InSe provides an ideal conduction channel due to the strong dependence of its 2D energy subbands on quantum confinement and high mobility,[33] offering a route to the modulation of electrical properties. Charge tunnelling into

consecutive 2D subbands of InSe leads to multiple regions of negative differential conductance that can be tuned by electrostatic gating. Our devices could provide the foundation for further technologies, such as low-power consumption transistors and broad-band sources and detectors compatible with existing photonic and CMOS technologies. Recent observations of intersubband transitions by near-field optics in TMDs[177] have demonstrated the potential of 2D intersubband transitions for optoelectronics. The InSe-based TFETs demonstrated in this work has the potential for a broad spectral range with intraband transitions tuneable from the near-infrared in a bilayer InSe to the far-infrared/terahertz range in thicker InSe films. In particular, by suitable design of the layer thicknesses, it may be possible to engineer population inversion between the subbands and tune the photon emission, as done in quantum cascade lasers based on traditional semiconductors.[178]

Chapter 7

Enhanced UV detection with InSe/graphene heterostructures

This chapter reports on graphene/InSe/graphene vertical heterostructures as ultraviolet-visible (UV-VIS) detectors. The optoelectronic transport characteristics of these devices suggest a favourable band alignment between InSe and graphene, which facilitates the efficient extraction of photogenerated charge carriers. Optical absorption studies of InSe by spectroscopic imaging ellipsometry are also presented. Preliminary ellipsometry measurements on bulk InSe indicate strong resonances in the UV range of the absorption spectrum. Theoretical modelling is in good agreement with the experimental findings and unveils the origin of these resonances.

The devices studied in this chapter were fabricated by Dr. James Kerfoot and Dr. Zakhar Kudynskyi at Nottingham. Transport measurements and optical studies of the devices were performed by Dr. Zakhar Kudynskyi and myself. Ellipsometry studies of bulk InSe were carried out by Dr. Christopher Mellor, Dr. Richard Cousins and myself. Prof. Lijun Zhang (Jilin University, China) has supported this work with theoretical modelling of the band structure and absorption spectrum of InSe.

7.1. Introduction

Despite being a few atoms thick, 2D vdW materials exhibit an extraordinary optical response compared to their bulk 3D counterparts due to their strong electron-photon interactions.[179-181] Since its discovery, graphene has

been extensively exploited for various optoelectronic applications including photodetection.[9,59,182] However, due to the absence of a band gap and due to its linear dispersion around the Dirac point, it absorbs only 2.3% of the incident photons, which is not suitable for many applications.[183,184] Beyond graphene, the library of semiconducting 2D materials is ever-expanding, enabling a photoresponse over a wide range of the electromagnetic spectrum from the ultraviolet (UV) to the visible (VIS), infrared (IR), and terahertz (THz).[7,135] Moreover, the quantum confinement along the direction perpendicular to the layer plane of these semiconductors can lead to strong excitonic effects and sharp peaks in the density of states (DOS) near the conduction and valence band edges, increasing light absorption efficiency.[185] Hence, these 2D layers with naturally passivated surfaces[186] enable the construction of a new generation of photodetectors.[187]

Within the diverse range of photodetectors, there is a significant interest in UV detection as it is becoming increasingly important for security, advanced communication, situational awareness *etc*.[188] Traditional UV photodetectors based on Si face the major challenge of a low photoresponsivity (typically, less than 0.1 AW^{-1} for $\lambda < 400$ nm) due to the high reflection coefficient and shallow penetration depth of UV light in Si.[189,190] Other alternatives, such as photomultiplier tubes (PMTs), charge-coupled devices (CCDs) and wide band gap semiconductor photodiodes, are limited by high power consumption and/or low efficiency.[191-193] To date, several layered 2D materials based UV photodetectors have been reported using graphene, hBN, BP, TMDCs *etc.*, reporting UV photoresponsivity of up to $9x10^4$ AW^{-1}.[194] However, these devices generally exhibit a slow response time (~1s).[195,196] Recent breakthroughs within

the family of 2D materials include the exploitation of InSe, which has a direct band gap E_g = 1.26 eV at T = 300 K in its bulk form.[31,33] The band gap of InSe can be tuned by reducing the number of atomic layers in the crystalline sheet due to quantum confinement.[31,33] Recent reports of bendable photodetectors[58], large-scale image sensors,[57] electroluminescence in p-n junctions,[48] and FETs with large current on/off ratios (~10^8) and high carrier mobilities (μ = 0.1 $m^2V^{-1}s^{-1}$) at room temperature[33] have demonstrated the great potential of InSe for future technologies. This burgeoning research field is still in its infancy and offers exciting opportunities for discoveries and the realization of functional devices that implement InSe in combination with other vdW crystals.

Here, we report optoelectronic studies of vertical graphene/InSe/graphene encapsulated by hBN. In these devices, InSe forms a good ohmic interface with the graphene electrodes and acts as an optically active absorbing channel. Due to its high electrical conductivity and weak optical absorption[10,197], graphene is well suited as a transparent electrode. While the tunnelling transport in these devices is already reported in chapter 6, this chapter focuses on their behaviour under optical illumination and exploits its suitability as ultraviolet-visible (UV-VIS) detectors. Optical absorption studies by spectroscopic imaging ellipsometry on bulk InSe reveal enhanced absorption in the UV range. Theoretical modelling based on first-principle studies of the electronic band structure of InSe accounts for the role of atomic orbitals in UV absorption. Our InSe-based UV photodetectors have high responsivity and are compatible with Si-based complementary metal-oxide-semiconductor technology and optical waveguides, revealing the potential use of InSe for UV

detection relevant for environmental monitoring, astronomical studies, missile detection *etc.*[188,198,199]

7.2. Photosensing with InSe/graphene heterostructures

Figure 7.1a illustrates the schematic and the optical image of a typical device fabricated by sequential stamping of hBN, graphene (MLG), InSe, graphene (MLG) and hBN flakes on a SiO_2/Si substrate (300 nm-thick SiO_2) by an all-dry viscoelastic transfer technique, as described in chapter 6. In this particular device, the InSe layer has an in-plane area of about 100 μm^2 and thickness t ~ 8 nm (10 layers). Different devices were fabricated by varying the thickness (8 - 19 layers) of the sandwiched InSe layer, thus effectively varying the channel length between the graphene electrodes. The top and bottom hBN flakes act as ideal electrical insulators with a close lattice match to graphene.

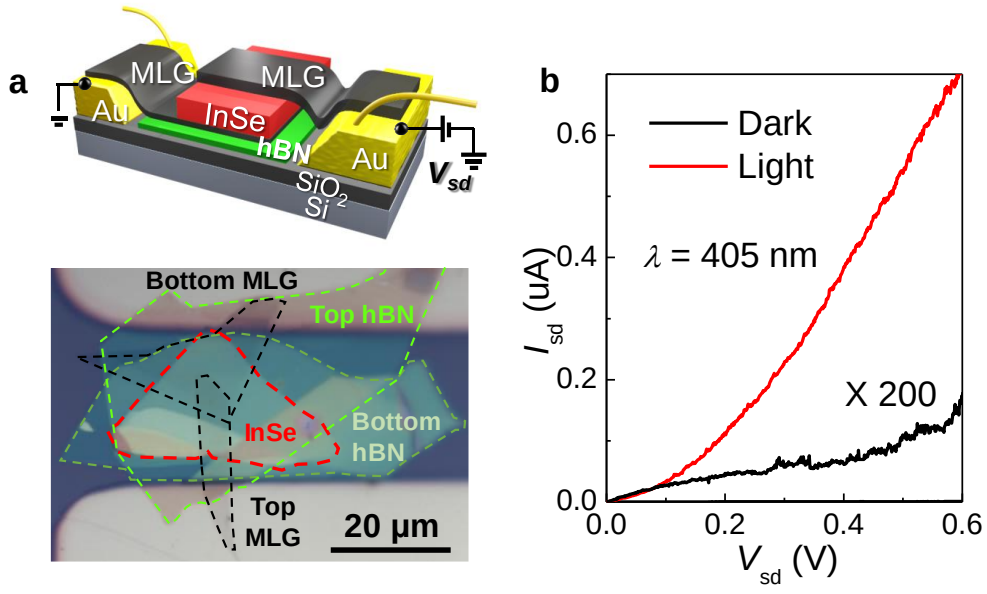

Figure 7.1. (a) Schematic diagram and optical image of an InSe-based vertical detector constructed onto a SiO_2/Si substrate. **(b)** I_{sd}-V_{sd} characteristics of this device in the dark and under optical illumination conditions (λ = 405 nm, P = 50 μW).

Under light illumination, the carriers photogenerated in InSe are swept by the electric field and extracted at the graphene electrodes, thus causing a photocurrent. The mechanism for the photoresponse is discussed in detail later in this chapter. **Figure 7.1b** shows the room temperature (T = 300 K) current-voltage I_{sd}-V_{sd} characteristics for the particular device shown in Figure 7.1a i) in the dark and ii) with the device uniformly illuminated by an unfocused laser with λ = 405 nm (photon energy hv = 3.06 eV). In the dark, I_{sd} is relatively small, increasing weakly with increasing V_{sd}. Under illumination, I_{sd} increases significantly in comparison to dark conditions.

The injection and extraction of charge carriers to and from InSe layers are strongly dependent upon the band alignment at the graphene-InSe interface. For electrons, this is facilitated by the vicinity of the conduction band edge of InSe to the Dirac point of graphene: the electron affinity of graphene (χ_{gr} = 4.5 eV) is only slightly smaller than that of bulk InSe (χ_{InSe} = 4.6 eV).[60] Also, the work function of graphene (ϕ_g) can be tuned by field-effect electrostatic gating and/or light intensity[61] relative to that for *n*-type InSe (ϕ_{InSe} = 4.8 eV).[48] Under optical illumination, an optical window is created in the overlapping region of the two graphene electrodes and the InSe layer, enabling the generation of excess electron-hole pairs. Electrons and holes are then swept by the electric field of the junction due to the applied bias, V_{sd}, resulting in a photocurrent. We have examined several device structures with different thicknesses t of the InSe layer. Our study on these devices has not revealed any systematic dependence of the photoresponse on t. Although our fabrication process is reliable and reproducible (detailed discussion in chapter 6), the presence of residual polymer at the

graphene-InSe interface can introduce an additional contact resistance, reducing the current. Here, we focus on our best device structures with t ~ 8-10 layers.

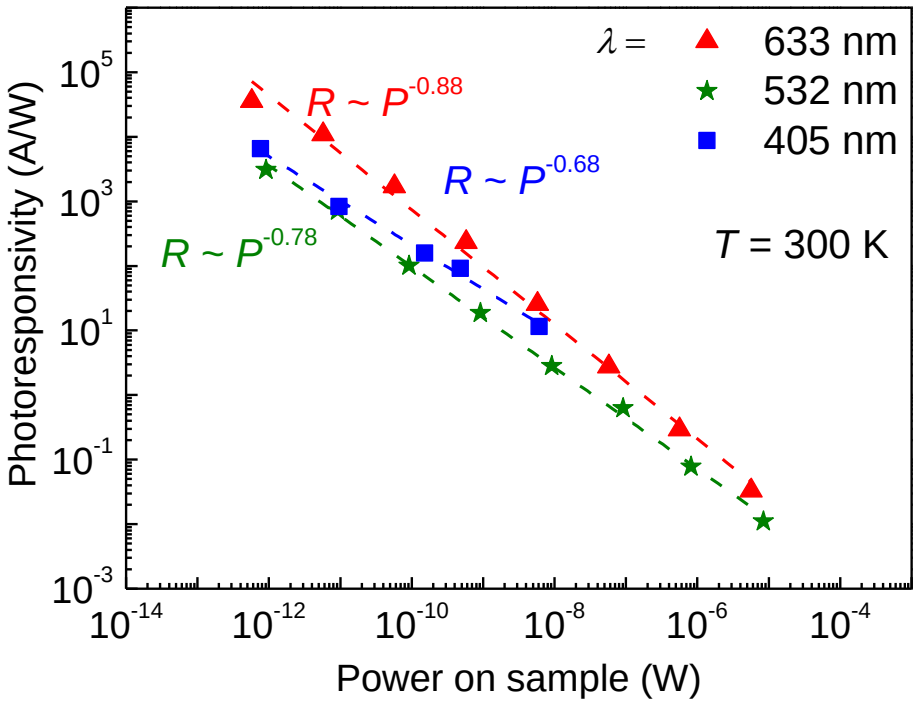

Figure 7.2. Photoresponsivity versus incident laser power at T = 300 K and λ = 633 nm, 532 nm and 405 nm for a graphene/InSe/graphene vertical heterostructure (t ~ 10 layers of InSe) at V_{sd} = 0.25 V. The dashed lines represent a power law of the form $R = CP^{-y}$, where y ~ 0.88 for λ = 633 nm, y ~ 0.78 for λ = 532 nm and y ~ 0.68 for λ = 405 nm, and C is a constant.

Figure 7.2 shows that a device with t ~ 10 layers of InSe is highly photosensitive over a broad-band (NIR-to-VIS) range at room temperature (T = 300 K). The photoresponsivity R, which is defined as the ratio of the photocurrent (ΔI_{sd}) to the incident light power (P), reaches the largest values at the lowest powers: R ~ 10^5 A/W for λ = 633 nm and R ~ 10^4 A/W at λ = 405 nm and λ = 532 nm. Data of R versus P in Figure 7.2 are well described by a power law of the form $R = CP^{-y}$, where y ~ 0.88 for λ = 633 nm, y ~ 0.78 for λ = 532 nm and y ~ 0.68 for λ = 405 nm, and C is a constant (see dashed lines). The

decrease of R with increasing P is analogous to the P-dependence reported previously for the photoresponsivity of other graphene-based photodetectors.[59,184,200] The values of R for our devices are significantly higher than those previously reported for similar InSe/graphene vertical heterostructures (R ~10^3 A/W at P ~ 10^{-12} W, λ = 633 nm), which did not have any hBN encapsulating layer.[35] The encapsulation of InSe by hBN leads to increased absorption of light by the InSe layer due to the reduced reflection of the laser light at the interface between air and hBN (refractive index η_{hBN} = 1.8),[59] compared to air (η_{air} = 1) and InSe (η_{InSe} = 2.1).[200]

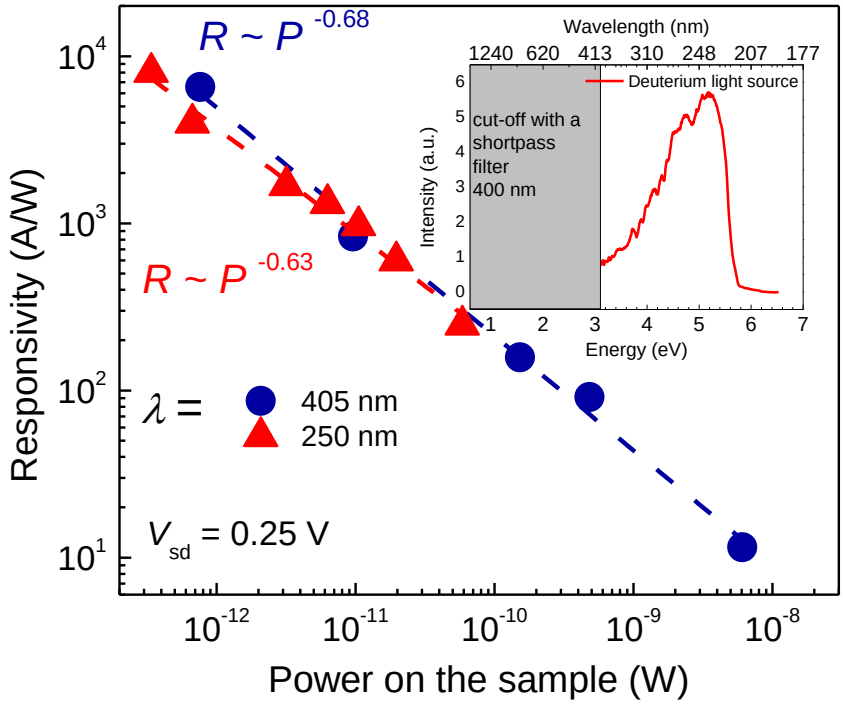

Figure 7.3. Comparison of the photoresponsivity for a device with 10 layers of InSe under illumination with light of λ = 405 nm and λ = 250 nm. The dashed lines represent a power law of the form $R = CP^{-y}$, where y ~ 0.63 for λ = 250 nm and y ~ 0.68 for λ = 405 nm, and C is a constant. Inset: Intensity versus photon energy curve for a deuterium lamp, passed through a short-pass filter at λ = 400 nm. The intensity is maximum around λ = 250 nm.

As shown in **Figure 7.3**, a good photoresponse was also measured by illumination of our devices with a deuterium lamp. Using a short-pass filter at 400 nm, the spectrum of the lamp is centred at λ = 250 nm (hv = 4.96 eV), as shown in Figure 7.3 (inset). Under this broad-band excitation, our device with t ~ 10 layers shows a similar high photoresponsivity (up to $R \sim 10^4$ A/W at $P = 10^{-12}$ W) compared to light illumination at λ = 405 nm (hv = 3.06 eV). Data of R versus P are well described by a power law of the form $R = CP^{-y}$, where $y \sim 0.63$ for λ = 250 nm and $y \sim 0.68$ for λ = 405 nm, and C is a constant (see dashed lines). No significant difference in the photoresponsivity at λ = 250 nm and λ = 405 nm was observed. This observation is discussed in section 7.3.

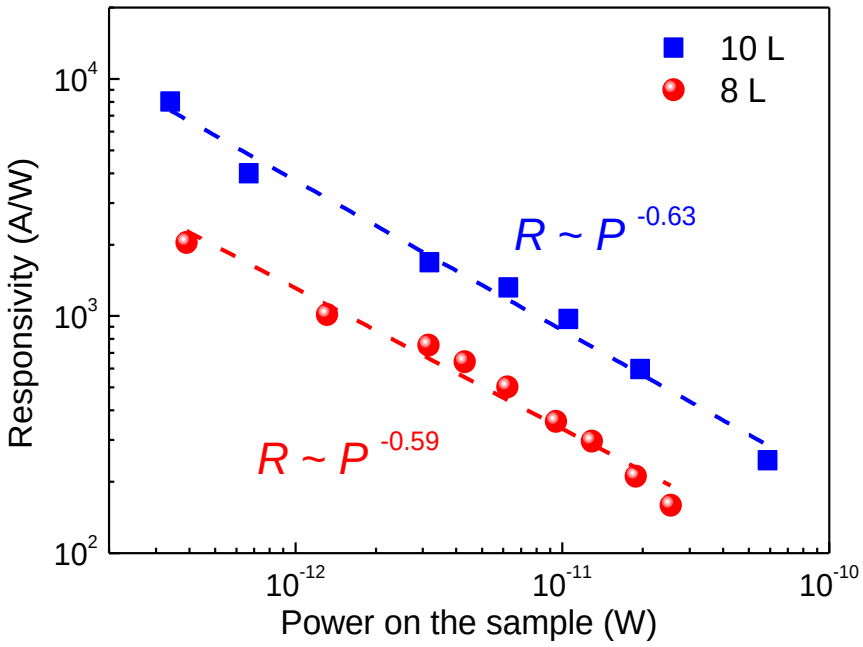

Figure 7.4 Comparison of the photoresponsivity of graphene/InSe/graphene vertical heterostructures with an active InSe channel of thickness t = 10 layers and 8 layers under illumination with light from a deuterium lamp (centred at λ = 250 nm). The dashed lines represent a power law of the form $R = CP^{-y}$, where y ~ 0.63 for t = 10 layers nm and y ~ 0.59 for t = 8 layers, and C is a constant.

Figure 7.4 compares the photoresponsivity of devices with 10 and 8 layers of InSe under illumination by light from a deuterium lamp (centred at λ = 250 nm). For the device with 10 layers of InSe, we observe a higher photoresponsivity: for $P \sim 10^{-13}$ W, $R \sim 10^{4}$ A/W for t = 10 layers and $R \sim 10^{3}$ A/W for t = 8 layers. The dashed lines represent a power law of the form $R = CP^{-y}$, where $y \sim 0.63$ for t = 10 layers nm and $y \sim 0.59$ for t = 8 layers, and C is a constant.

We have examined devices with different layer thicknesses and they do not always reveal a high photoresponsivity. For example, a similar InSe/graphene vertical heterostructure with an InSe layer thickness of 19 layers showed a weak photoresponse. We believe that this behaviour may be associated with the existence of charge traps for the majority carriers. These traps could be present within the InSe crystal and/or at the surface/interface. These could be introduced during the fabrication procedure.[35,58,201] This requires further investigations and improvement of the fabrication of both materials and devices.

7.3. Modelling the photoresponsivity and optical absorption

We first consider a simple model for the photoresponsivity. The *n*-type InSe channel has thickness *t*, width *w*, and length *l*. Under illumination with light of power *P* and energy *hv* larger than the band gap energy of InSe, electron-hole pairs are generated in InSe. The densities of photo-created electrons and holes are equal, *i.e.* $\Delta n = \Delta p$, and, at steady state, they can be expressed in terms of the minority carrier (hole) lifetime, τ_l, and the rate of carrier generation by light G,[202] such that

$$\Delta n = \Delta p = G\tau_l, \tag{7.1}$$

where $G = (t\alpha)(P/h\nu)(wtl)^{-1}$and α is the absorption coefficient of InSe at the photon energy $h\nu$. When a voltage (V_{sd}) is applied between the top and bottom graphene electrodes, photogenerated carriers are separated in the optically active InSe channel, resulting in a photocurrent along the *z*-direction, as shown in Figure 7.1b. The photogenerated current ΔI_{sd} can be written as

$$\Delta I_{\mathrm{sd}} = \Delta n e v_d (wl), \tag{7.2}$$

where $v_d = {}^{t}/_{\tau_l}$ and τ_l is the electron transit time across the thickness *t* of the InSe flake. Thus, taking into account the expression of v_d and ΔI_{sd}, we derive

$$\Delta I_{\mathrm{sd}} = (e\alpha)\left(\frac{P}{h\nu}\right)\left(\frac{\tau_l}{\tau_t}\right). \tag{7.3}$$

The photoresponsivity can be written as

$$R = \frac{\Delta I_{\mathrm{sd}}}{P} = \left(\frac{e\alpha}{h\nu}\right)\left(\frac{\tau_l}{\tau_t}\right). \tag{7.4}$$

Hence, the photoresponsivity depends primarily on the absorption α and a ratio of times, ${}^{\tau_l}/_{\tau_t}$. *R* is reduced with decreasing τ_l and/or increasing τ_t. This highlights a trade-off between the photogain and response speed,which is controlled by the lifetime of minority carriers within the semiconducting layer.

As discussed in chapter 3, the optical absorption coefficient α is directly proportional to ε_2, the imaginary part of the pseudo-dielectric function ($\varepsilon = \varepsilon_1 + i\varepsilon_2$). We calculated ε_2 using first-principles calculations of the electronic band structure at highly dense *k*-points in the Brillouin zone with the inclusion of spin-orbit coupling (SOC). **Figure 7.5** shows the energy ($h\nu$) dependence of ε_2 for InSe layers of different thicknesses and electric field **E** polarized in the layer plane, $\mathbf{E}\perp\boldsymbol{c}$ (detailed discussion in chapter 5). The dashed lines represent different energies used to excite the graphene/InSe/graphene heterostructures,

i.e. $h\nu$ = 1.96 eV (λ = 633 nm), $h\nu$ = 2.33 eV (λ = 532 nm), $h\nu$ = 3.06 eV (λ = 405 nm) and $h\nu$ = 4.96 eV (λ = 250 nm).

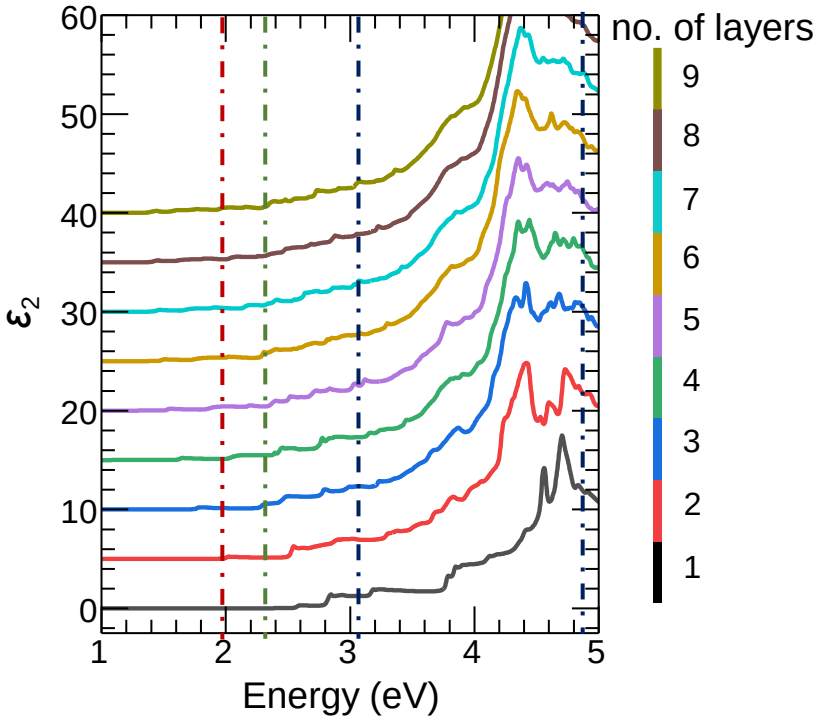

Figure 7.5 Imaginary part of the dielectric function for different InSe layer thicknesses (1-9 layers) and light polarized in the layer plane, i.e. **E**⊥***c***. Dashed lines represent different energies used to excite the graphene/InSe/graphene heterostructures: $h\nu$ = 1.96 eV (λ = 633 nm), $h\nu$ = 2.33 eV (λ = 532 nm), $h\nu$ = 3.06 eV (λ = 405 nm) and $h\nu$ = 4.96 eV (λ = 250 nm).

For **E**⊥***c***, ε_2 increases with increasing energy, revealing a significant enhancement in the near-UV range. Step-like features and resonances are also observed and their energy position depends on the thickness of the InSe layer. The broadband absorption spectrum for InSe layers of different thicknesses is in line with the broadband photoresponsivity revealed in our experiments. Figure 7.5 demonstrates that our devices exhibit a similar high photoresponsivity at different excitation energies, *viz*, 1.96 eV (λ = 633 nm), 2.33 eV (λ = 532 nm), 3.06 eV (λ = 405 nm) and 4.96 eV (λ = 250 nm). However, based on the enhanced

absorption predicted at 3.06 eV (λ = 405 nm) and 4.96 eV (λ = 250 nm), one would have expected a higher photoresponsivity in these two ranges (Figure 7.2 and 7.3). Thus, we conclude that a large absorption does not always translate into a high photoresponse.

To further understand the photoresponsivity, we consider additional mechanisms. According to equation 7.2, the photoresponsivity depends on the ratio of times, τ_l/τ_t . This dependence can account for the strong dependence of *R* on the optical power, as already reported for InSe based detectors.[57,58] With increasing power, the generation of a larger density of charge carriers can lead to enhanced carrier scattering, increasing the transit time τ_t.[203] Furthermore, a high population of charge carriers can also induce Auger-like recombination processes, thus decreasing τ_l. These processes are commonly enhanced in 2D vdW crystals due to stronger Coulomb interactions [35] and can also depend on the photon excitation, which requires further investigations.

Finally, we note that our photoresponsivity data and modelling of the optical absorption of InSe suggest that the optoelectronic properties of these devices can be modified by changes of the InSe nanosheet thickness *t* between the graphene electrodes. Further experimental work will be required to unlock the optimal thickness of the InSe layer to achieve a maximum photoresponse at a given wavelength.

7.4. Absorption measurements by ellipsometry

We have used the variable-angle spectroscopic imaging ellipsometry (VASE) technique to measure the absorption coefficient α of bulk InSe. We have used an M2000-DI instrument made by J.A.Woollam InC. and probed the

wavelength range from 1000 nm to 190 nm, corresponding to the energy range 1.25 eV - 6.47 eV. The collimated beam results in an elliptical spot with a minor axis of 2 mm on the sample. The major axis depends on the angle of incidence, which can be varied from 55° to 65°. The data acquired was analysed using the CompleteEase software version 5.19. Since VASE is an indirect technique, the components of the pseudo-dielectric function ε_1 and ε_2 and pseudo-refractive index η and κ are derived from the acquired data using the modelling software; thereafter, the absorption coefficient α is deduced using the relation: $\alpha = \frac{2\pi\varepsilon_2}{\eta\lambda} = \frac{4\pi\kappa}{\lambda}$, as discussed in chapter 3.

Figure 7.6a shows the spectra of the components of the pseudo-dielectric functions ε_1 and ε_2, and the components of the pseudorefractive indices η and κ. The data was taken at different areas of a sample of bulk InSe (thickness along the *c*-axis of ~ 1.5 cm) with the collimated beam at three different angles, 55°, 60° and 65° relative to the plane of incidence, *i.e. ab*-plane of InSe, at room temperature (T = 300 K). These curves overlay onto each other within the noise level. We have calculated the absorption from these parameters, as shown in **Figure 7.6b**. In the low energy region (< 3 eV) of the absorption spectrum, the data indicate a broad absorption. We could not detect a clear sharp edge at the energy of the A transition ($h\nu$ ~ 1.26 eV),[33] *i.e.* the transition between the conduction band and valence band edges at the Γ point of the Brillouin zone.[33,99,154,204] This could be a limitation of the experimental setup in the NIR region.

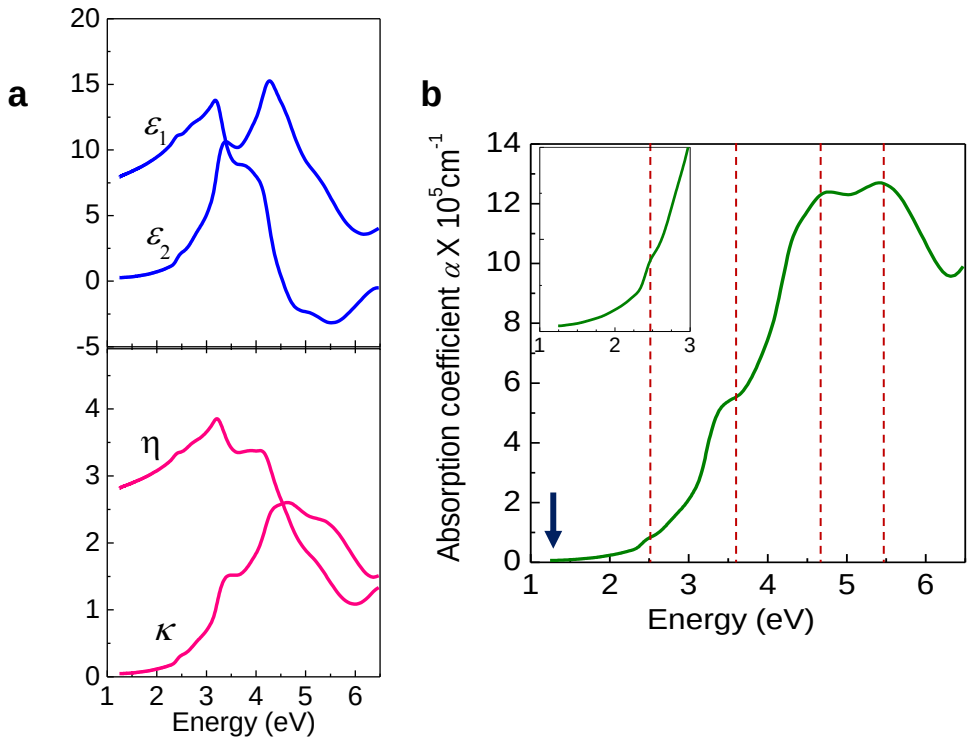

Figure 7.6. (a) Components of the pseudodielectric function $\varepsilon = \varepsilon_1 + i\varepsilon_2$ and of the pseudo-refractive index $N = \eta + i\kappa$ for bulk InSe, as modelled by the software based on the ellipsometry experiment. **(b)** The calculated absorption spectrum of bulk InSe, as derived from the data in part (a). The arrow and the dashed lines indicate the absorption at the band gap energy and the critical points near 2.4 eV, 3.5 eV, 4.5 eV and 5.5 eV. Inset: Absorption spectrum near 2.4 eV, with a resonant feature corresponding to the B transition.

We note that the spectra do not reveal near the absorption edge any excitonic absorption peak, which should be centred at an energy of E_g ~ 1.25 eV, lower than the band gap energy (E_g = 1.2635 eV, T = 300 K)[96] due to the exciton binding energy (E_B = 14.5 meV).[32,96] Excitonic effects are generally more pronounced at low temperature ($k_BT < E_B$), as reported earlier.[96] An excitonic band edge emission could instead be observed by PL studies, revealing a PL emission centred at 1.26 eV at 300K.[31,54] In general, the band gap derived from a PL experiment might not correspond precisely to that derived from ellipsometry for several reasons: for example, the disorder/thermalization of

carriers in PL produce a Stokes shift of the PL emission relative to the absorption. Furthermore, we note that the absorption coefficient α increases with increasing energy and is significantly enhanced in the UV range (E > 3 eV). Resonant features, *i.e.* the critical points (CP), are seen near 2.4 eV, 3.5 eV, 4.5 eV and 5.5 eV, which are in good agreement with the absorption spectra reported earlier based on transmission measurements.[205,206]

In the VASE technique, the incident beam falls obliquely on the sample, enabling a component of $\mathbf{E} \| \boldsymbol{c}$. Due to the preferential coupling of the electronic states to light polarized along the *c*-axis, *i.e.* for $\mathbf{E} \| \boldsymbol{c}$, the interband optical transition (B transition, 2.4 eV)[33] between the $p_{x\text{-}y}$-like orbitals in the VB and the *s*-like CB states of bulk InSe remains fully allowed,[39,54] as previously discussed in chapter 5. This explains the origin of resonances at the first critical point ~ 2.4 eV in Figure 7.6 (inset), which was not prominent in the ellipsometric spectra reported previously.[207] Our observation is in line with the theoretically calculated value of 2.2 eV[208] and other absorption studies based on transmission measurements.[205,206]

At energies above 2.4 eV, the absorption coefficient increases sharply and is significantly enhanced in the UV range ($h\nu$ > 3 eV). The origin of the critical points at 3.5 eV, 4.5 eV and 5.5 eV remains uncertain. Previous reports have claimed that the critical point near 3.31 eV is due to transitions from the valence band maximum to the third group of conduction bands at or near the Γ point.[205] Theoretical calculations reported previously have also predicted that critical points at 4.5 eV and 5.5 eV could be due to transitions from doubly degenerate pairs from the mixing of Se p_{xy} and In p_{xy} states and/or, bonding and

antibonding Se and In *s* and p_z states. [208,209] Further theoretical studies are required to unravel the origin of the UV resonant absorption features.

Previous studies on TMDCs have shown that the absorption usually increases with the layer number.[210] A layer dependent absorption is also predicted for InSe. However, a large set of samples with a controlled thickness of InSe is required to measure this dependence using different techniques. Absorption measurements based on transmission spectroscopy require the 2D nanoflakes to be suspended and/or be deposited on transparent substrates, which is challenging.[210] Alternatively, the VASE technique may provide an effective approach to determine the layer dependent absorption of InSe.

7.5 .Summary

In summary, we have used InSe for UV detection. Our photodetectors, based on graphene/InSe/graphene heterostructures show UV photoresponsivity of up to 10^4 A/W at room temperature. Spectroscopic imaging ellipsometry studies of bulk InSe indicate an enhanced UV absorption, which is confirmed by theory. Future ellipsometry studies of InSe layers of different thickness are required to probe the absorption coefficient and its dependence on the layer thickness. This information will be critical for the development of ultra-thin UV photodetectors with tunable absorption. However, other parameters can also affect the photoresponse of a photodetector, such as the carrier lifetime and mobility. Further optimization of the fabrication process and materials are needed to improve these parameters.

Chapter 8

Light-induced charge transfer at the interface of graphene and InSe

This chapter reports on a hybrid planar field-effect phototransistor based on a graphene-contacted InSe layer. This device is encapsulated by hBN and exhibits a fast, ultra-high photoresponsivity that exploits the exceptional electronic properties of InSe, hBN and graphene. In particular, the mechanism for photosensing is based on a light-induced charge transfer at the interface of InSe and graphene with the potential for high-photosensitive sensors and switches.

The devices described in this chapter were fabricated by myself and Dr. Zakhar R. Kudrynskyi at the University of Nottingham. Optical and transport studies were carried out by myself. These results were published in *Advanced Functional Materials* **29**, 1805491 (2019).

8.1. Introduction

Atomically thin layers of van der Waals (vdW) crystals and their heterostructures offer unique opportunities to explore and manipulate the transfer of electronic charge at the interface of different materials and to create high-performance multi-functional devices for integration with photonic and electronic technologies.[211] Amongst these 2D materials, the "post-transition" metal monochalcogenides, such as InSe, are receiving increasing attention,[26,41,45,212] as discussed in chapter 2. InSe can act as an electrically and optically active layer to "modulation-dope"[60] and photosensitize[213] an adjacent

graphene layer, and to induce a "giant" quantum Hall (QH) plateau in its magnetoresistance.[60,61] These phenomena involve a transfer of electronic charge at the InSe/graphene interface and offer opportunities to explore a diverse range of new electrical and optical devices. This chapter describes the effects of light on the transport properties of a hybrid field-effect phototransistor based on a graphene-contacted InSe layer encapsulated with hBN. It focuses on: i) the interface between the InSe and the graphene electrode; ii) the role of the hBN capping layer in the absorption/reflection of light by InSe; iii) mechanisms of the photoexcited charge transfer at the InSe/graphene interface. The high photoresponsivity of the InSe/graphene heterostructure described in this chapter arises from the sensitivity of the electrical conductivity of the graphene layer to electronic charges that are photogenerated in the InSe layer and transferred across the interface onto graphene.

8.2. Devices and interfaces

Figure 8.1a illustrates the schematic of a typical device fabricated by sequential stamping of InSe and hBN flakes onto two graphene contacts. These are based on commercially available CVD graphene on 300 nm thick SiO_2 on Si and are patterned by electron beam lithography (EBL), as described in Chapter 4. In these devices, the two graphene (G) layers serve as a source (*s*) and drain (*d*) electrodes to an InSe channel of length $l \sim 1$ μm and width $w \sim 20$ μm. The Si layer of the supporting SiO_2/Si wafer serves as a back-gate. The top hBN flake encapsulates the whole heterostructure and prevents it from contamination during long-term exposure to atmospheric conditions. An optical image of a typical device is shown in **Figure 8.1b**. In this device, the InSe layer has a thickness, $t > 20$nm. Previous reports suggest that the mechanical contact due to

attractive vdW forces at the graphene-InSe interface is atomically flat.[33,35,214] The interface has a low density of defects and is free from dangling bonds. Thus, graphene serves as an ideal electrode to InSe compared to conventional metals, such as Au.[33,35,200]

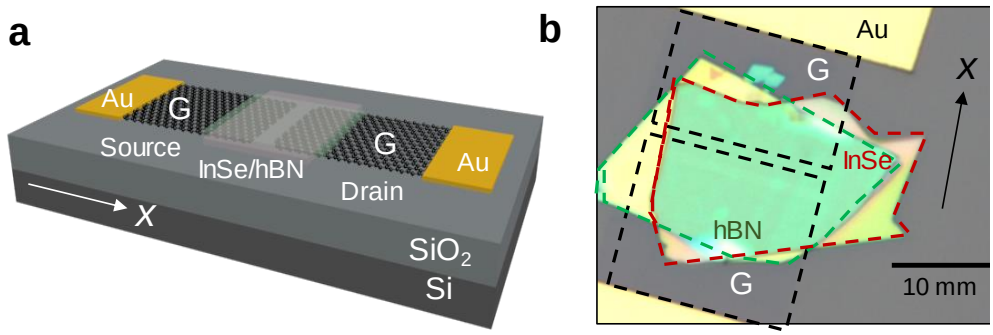

Figure 8.1.(a-b) Schematic diagram (a) and optical image (b) of a graphene-InSe/hBN-graphene planar device with regions of overlaps between the InSe (red line), hBN (green lines) and graphene (black lines) layers.

8.3. Charge transfer at the InSe/graphene interface

The graphene-InSe/hBN devices presented in section 8.2 are placed in a vacuum microscope cryostat and transport measurements are carried out using the technique discussed in Chapter 4. **Figure 8.2a** shows that the source-drain current, I_{sd}, through the graphene-InSe-graphene heterostructure (Fig. 8.1b) has a linear dependence on the applied source-drain voltage, V_{sd}, and increases with the increasing positive gate voltage (V_g). At $V_g < 0$ V, I_{sd} remains close to zero (black dashed line, Figure 8.2a), confirming the typical *p*-type behaviour of CVD graphene.[35,215] The linearity and symmetry of the I_{sd}-V_{sd} curve suggest that the graphene-InSe interface facilitates the formation of an Ohmic contact and that the two interfaces of the InSe with the two-graphene electrodes are symmetric. The linearity and symmetry of the I_{sd}-V_{sd} curve are preserved under optical illumination. **Figure 8.2b** shows the dependence of the photocurrent, ΔI_{sd}, on

V_{sd} while the device is illuminated with an unfocussed He-Ne laser (λ = 633 nm, spot diameter 1 cm) with P = 50 μW at V_g = 0 V. The photocurrent, ΔI_{sd} increases by a factor of ~ 10^2 under illumination at V_{sd} = 0.1 V. Interestingly, at V_{sd} = 0 V there is a measurable current $I_{sd} \neq 0$, indicating a photovoltaic effect, *i.e.* the presence of a built-in electric field that separates the photogenerated electron-hole pairs (inset, Figure 8.2b).

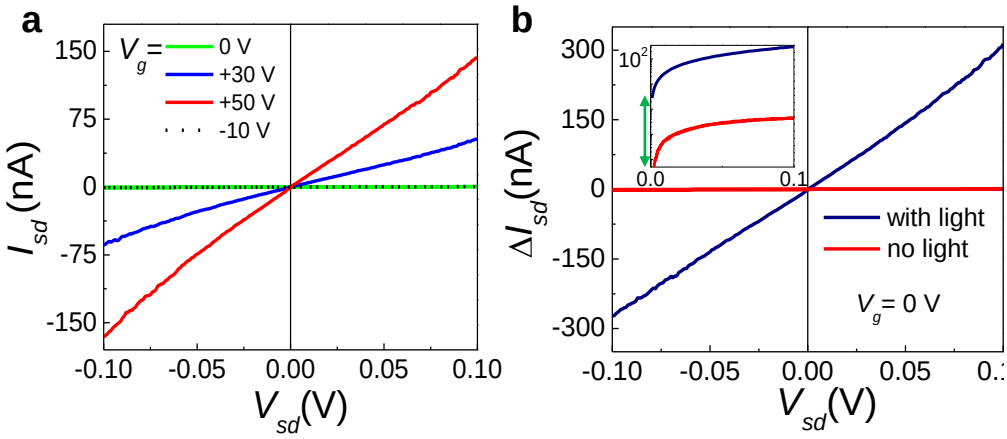

Figure 8.2.(a) Current-voltage characteristics of a SiO_2/Si back-gated, planar graphene-InSe-graphene heterostructure in the dark at T = 300 K for increasing gate voltages. **(b)** Photocurrent, ΔI_{sd}, versus V_{sd} at T = 300 K and V_g = 0 V under light illumination with an unfocused laser beam (λ = 633 nm) at P = 50 μW. **Inset**: I_{sd}-V_{sd} in logarithmic scale, indicating that $I_{sd} \neq 0$ at V_{sd} = 0 V.

To explore this photovoltaic phenomenon further, the room temperature photocurrent map is obtained by scanning a focused laser beam (λ = 405 nm and P = 50 μW) across the plane of the device with and without an applied source-drain bias voltage, V_{sd}, at V_g = 0 V. As shown in **Figure 8.3a**, for V_{sd} = 0 V, a photocurrent ΔI_{sd} is generated in the InSe-capped graphene layers (areas within the dashed lines in Figure 8.1b). This photocurrent is non-uniform, is enhanced at the graphene edges and has opposing polarities on the two graphene

electrodes. These data suggest that a built-in electric field is present at the graphene/InSe interface (Figure 8.3a) and that this field is stronger at those edges of the graphene electrodes that overlap with InSe.

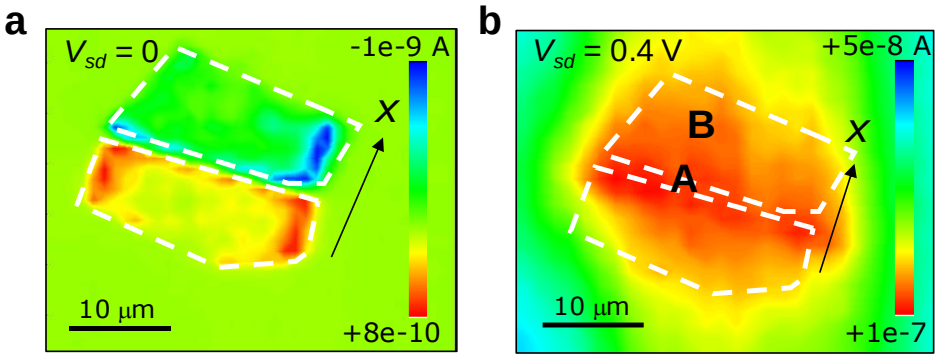

Figure 8.3. Photocurrent maps acquired at V_{sd} = 0 V **(a)** and V_{sd} = 0.4 V **(b)** with a scanning focussed laser beam, λ = 405 nm, P = 50 μW and T = 300 K. The gate voltage is V_g = 0 V.

Figure 8.3b shows that the photocurrent increases for V_{sd} > 0 V. The photocurrent is generated in two distinct regions: the area of the InSe flake between the two graphene electrodes (region A) and in the InSe-capped graphene layers (region B) of the device, shown in Figure 8.1b. No significant photocurrent is observed in graphene regions that are not capped by the InSe.

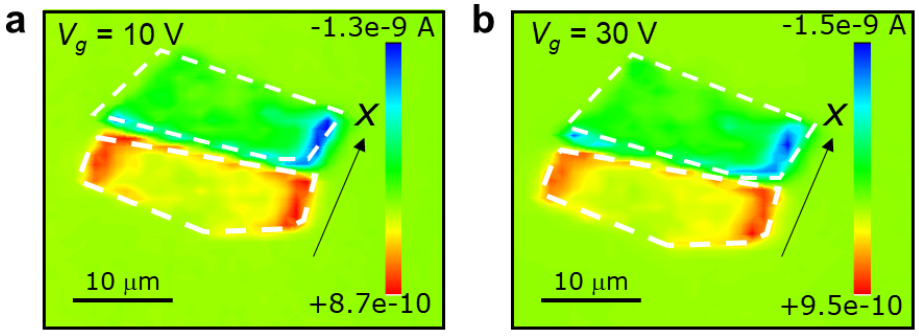

Figure 8.4 Photocurrent maps acquired at V_{sd} = 0 V with a scanning focussed laser beam (λ = 405 nm, P = 50 μW and T = 300 K) at gate voltage V_g = 10 V **(a)** and V_g= 30 V **(b)**.

Figure 8.4(a-b) shows the effect of electrostatic gating on the photocurrent maps acquired for V_{sd} = 0 V at V_g = 10 V (Figure 8.4a) and V_g = 30 V (Figure 8.4b). The photocurrent at the graphene edges bounding region A is enhanced with an increase in the gate bias V_g. μPL measurements are conducted on the same graphene-InSe heterostructure by using a confocal microscope system with a He-Ne laser (λ = 633 nm). A small laser power of 10 μW is used to avoid laser heating and photo-induced oxidation.[216] As can be seen in **Figure 8.5**, at V_g = 0 V and V_{sd}= 0 V, the PL signal is weaker around the edges of the graphene electrodes that overlap with InSe. This observation is in line with the photocurrent map of Figure 8.3a, showing a stronger PC signal in regions near the edges of graphene where a charge transfer from InSe onto graphene takes place.

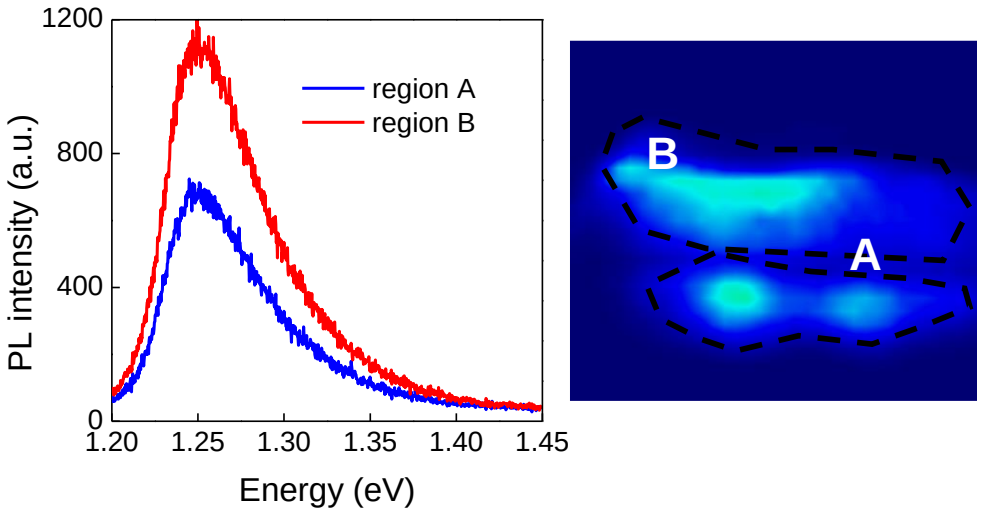

Figure 8.5. Photoluminescence (PL) spectra and integrated PL intensity map showing a weaker PL signal from InSe at the edges of the graphene electrodes (V_g = 0 V and V_{sd}= 0 V; λ = 633 nm, P = 10 μW and T = 300 K).

We explore further the effect of electrostatic gating on the PL signal. **Figure 8.6(a-b)** shows the PL maps acquired with V_{sd} = 0 V at V_g = 10 V (Figure

8.6a) and V_g = 30 V (Figure 8.6b). These maps reveal that the PL signal increases with increasing V_g following the corresponding increase of the photocurrent (Figure 8.4).

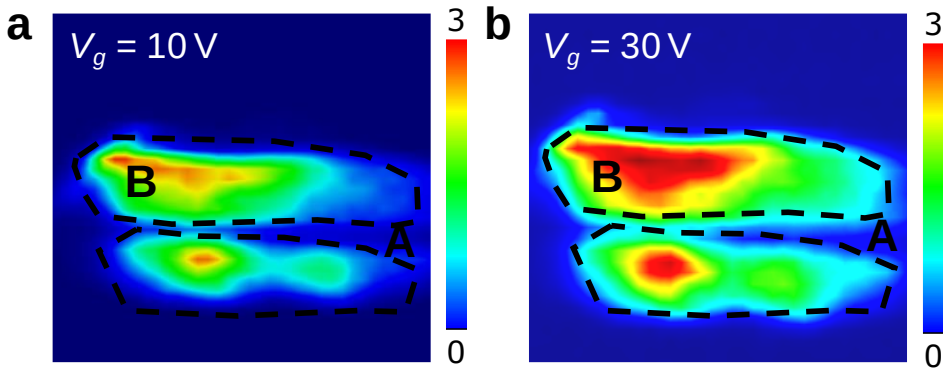

Figure 8.6. Photoluminescence maps acquired with V_{sd} = 0 V and T = 300 K at gate voltages V_g = 10 V **(a)** and V_g = 30 V **(b)** (λ = 633 nm and T = 300 K).

To explain these observations, we consider the band alignment at the interface of graphene and InSe (**Figure 8.7a-b)**. Both charge injection from graphene into InSe and the extraction of photogenerated carriers from InSe onto graphene depend on the band alignment at the interface. The linear and symmetric I_{sd}-V_{sd} of our devices (Figure 8.2a) suggest a high-quality interface between graphene and InSe. Thus, we neglect the contribution of impurities and/or defects at the interface when examining the alignment of the bands. The electron affinity of graphene (χ_g = - 4.5 eV)[217] lies closer to the vacuum level than that of bulk InSe (χ_{InSe} = - 4.6 eV)[218]. Also, the work function of graphene (ϕ_g) can be tuned by field-effect electrostatic gating and/or light intensity[61] relative to that for *n*-type InSe (ϕ_{InSe}= - 4.8 eV).[48] Under optical illumination and/or, electrostatic gating, the Fermi level of graphene can approach the InSe CB edge and its donor states, inducing a transfer of carriers between the layers.

In our photocurrent experiments, a focused laser beam with micrometre precision scans the whole device across the plane. At V_{sd} = 0 V, no photocurrent is observed between the graphene electrodes (region A) as the electric field is zero (**Figure 8.7a**). However, near each graphene electrode, the built-in electric field creates an electron current. The polarity of this current is different at each electrode. Thus, a photocurrent of opposite polarity is generated at the graphene edges (**Figure 8.7b**).

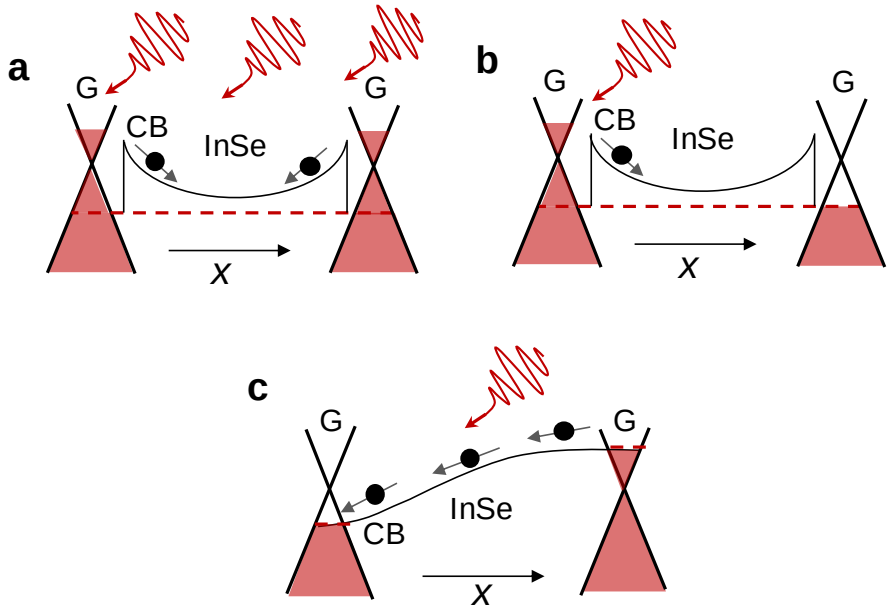

Figure 8.7. Photocurrent generation by the built-in electric field in region A **(a)** and the graphene/InSe interface **(b)** at V_{sd} = 0 V. **(c)** At V_{sd} > 0 V, photogenerated carriers drift (or thermal diffuse) along the InSe channel (Fig. 8.1b). For clarity, the band diagram in the inset shows the energy vs real space positions. The energy-wave vector dispersion of electrons in graphene is shown on top of the real space dependence.

At $V_{sd} \neq 0$ V, we ascribe the large photocurrent in region A to the drift of photogenerated carriers under the action of the applied electric field in the InSe gap between the graphene electrodes. We assign the smaller, but significant photocurrent in the InSe-capped graphene layers region B to thermal diffusion:

the photogenerated carriers diffuse in InSe and are extracted at the graphene electrodes by charge transfer (**Figure 8.7c**).

Under electrostatic gating, the bending of conduction band of InSe is reduced with respect to graphene, thus facilitating the transfer of charge between InSe and graphene, resulting an increase of the photocurrent (Figure 8.4). In addition, by reducing the electric field at the graphene/InSe interface, the applied gate facilitates the recombination of excitons, consistent with the general increase in PL with increasing V_g (Figure 8.6). These data demonstrate that a large photoresponse can be achieved in regions B with distinct light-absorbing (InSe) and conducting (graphene) layers, and regions A where the InSe layer acts simultaneously as a light-absorbing and conducting medium. The charge-transfer mechanism for photodetection in regions B is significantly different from that previously reported for InSe-graphene planar and vertical photodetector structures[35] and analogous to that demonstrated in pentacene-graphene heterostructures.[219]

8.4. Photoresponsivity

This section examines the photoresponsivity of our devices for different incident powers, *P*. For these studies, an unfocused laser beam with l cm diameter illuminates the whole area of the device. Figure 8.6a shows that for this planar graphene-InSe-graphene heterostructure, the measured responsivity is strongly dependent upon the incident optical power. A photoresponsivity $R = {\Delta I_{sd}}/{P}$ of up to $R \sim 10^6$ A/W is achieved at the lowest incident power $P \sim 10^{-5}$ W/m^2 (λ = 633 nm) with V_{sd} = 0.1 V (**Figure 8.6a**). The strong decrease of *R* with increasing *P* is a common characteristic of many other vdW photodetectors

and is attributed to the mechanism of photoconductive gain[35,213,220], as discussed in Chapter 7. The photocurrent map in Figure 8.3b shows that both regions A and B contribute to the photoresponse of the device when V_{sd} > 0 V. Also, the photoresponse is relatively faster than the InSe/graphene photodiodes reported earlier.[35] The rise and decay times of the photocurrent are less than 1 ms in both regions A and B (**Figure 8.6b**). By comparing the photocurrent signals in areas with the hBN layer (Figure 8.1b, InSe/hBN overlapping) and without hBN region (bare InSe, without hBN, Figure 8.1b), we find that the encapsulation of InSe by hBN induces a systematic increase of the photocurrent (by a factor of ~ 3). We attribute this behaviour, which is not observed when the hBN layer lies below the InSe layer,[221] to an increased absorption of light by the InSe layer due to the reduced reflection of the laser light at the interface between air and hBN (refractive index η_{hBN} =1.8),[59] compared to air (η_{air} = = 1) and InSe (η_{InSe}= = 2).[200] The encapsulation of InSe by hBN also leads to an increased photoluminescence and Raman signals of InSe.

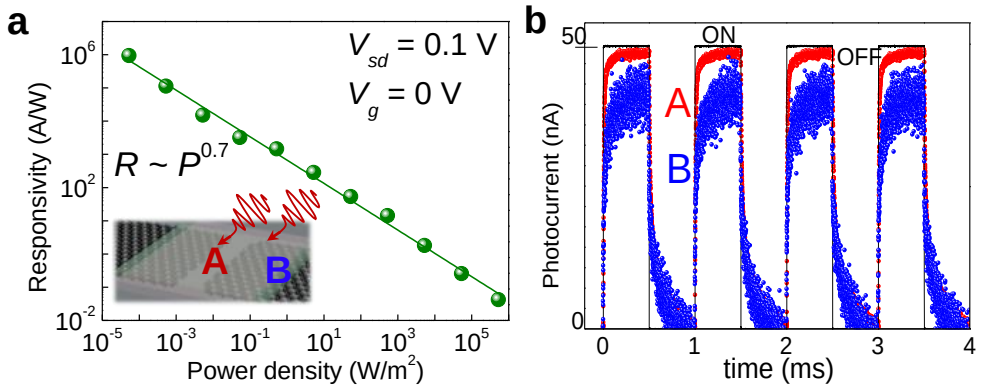

Figure 8.6.(a) Responsivity of planar graphene-InSe devices at different laser power densities and its empirical power-law fit $R \sim P^{0.7}$. **(b)** Temporal dependence of the photocurrent in regions A and B.

8.5. Summary

In conclusion, high-quality hybrid phototransistor devices can be realized using an InSe/graphene heterostructure. In these devices, the transport of photoexcited carriers in InSe is largely controlled by the electric field generated at the InSe/graphene interface. The light-induced charge-transfer at the InSe/graphene interface acts to photosensitize the graphene layer, giving rise to a fast and high photoresponsivity. All measurements presented in this work are obtained under quasistatic conditions so are not influenced by dynamic polarization effects. To probe the role of dipole-dipole interactions on the photoexcited charge transfer, ultra-fast pump-probe optical spectroscopy studies and optimized device geometries are required. These devices are made by a relatively simple fabrication process and offer a flexible route to integration with existing Si-manufacturing technologies beyond the capability of traditional semiconductor devices and other 2D photodetectors in the current literature.[59,200,222]

Chapter 9

Conclusions and outlook

The objectives of this PhD thesis were to exploit the inherent optoelectronic properties of 2D InSe and to demonstrate its potential for further technologies, through the investigation of InSe-graphene vdW heterostructures. The key findings of my research are summarised as follows:

(i) InSe nanosheets are mechanically flexible, making them robust when subjected to strain. Controllable and reproducible bending was achieved by exfoliation and transfer of atomically thin InSe nanoflakes onto a periodic array of Si-nanopillars.

(ii) A controlled modulation of the optical signals was demonstrated by exploiting the inherent optical anisotropy and mechanical flexibility of atomically thin 2D vdW InSe. This modulation depends on the InSe layer thickness, optical excitation energy and light polarization.

(iii) InSe provides an ideal conduction channel due to the strong dependence of its 2D energy subbands on quantum confinement, offering a route to the modulation of electrical properties. Charge tunnelling into consecutive 2D subbands of InSe leads to multiple regions of negative differential conductance that can be tuned by electrostatic gating. This experimental outcome is also backed by our theoretical modelling.

(iv) We have investigated field-effect transistor structures based on InSe and graphene of the significant potential for further technologies, such as low-power consumption transistors and broad-band sources and detectors compatible with

existing photonic and CMOS technologies. These devices also revealed photoresponsivity over a wide spectral range, including the UV range.

(v) Preliminary spectroscopic ellipsometry measurements on bulk InSe confirm absorption resonances in the UV. The experimental outcome is in good agreement with the theoretical predictions based on DFT.

(vi) A high-quality hybrid phototransistor based on InSe/graphene planar devices encapsulated by hBN was investigated. This device exhibits a fast, ultra-high photoresponsivity that exploits the exceptional electronic properties of InSe, hBN and graphene. The mechanism for photosensing is based on a light-induced charge transfer at the interface of InSe and graphene.

The key findings and prospects for further studies are discussed below.

9.1.1. Enhanced optical signals from bent InSe layers

The unique electronic band structure of InSe differs qualitatively from that of many other 2D materials, such as the widely studied TMDCs.[39] The conduction band edge states of InSe arise from antibonding In *s*-states, whereas the top valence band consists of Se p_z-like orbitals.[34,39,98] Thus, band-edge excitons tend to couple preferentially to light polarized along the *z*-direction (or *c*-axis), rather than along the *xy*-plane as for TMDCs.[39] Furthermore, mechanical strain can modify these properties.[55,145,146] In this work, we have demonstrated the deterministic positioning of 2D InSe flakes of different thicknesses onto a periodic array of Si-pillars. We have shown a reproducible bending of the layers, which causes a nanoscale spatial modulation of the Raman and photoluminescence signals across the array. Density functional theory-based calculations were used to model the measured effects and account for the role of

the geometrical shape and strain of the flake on the electronic states and light polarization properties. The geometrical shape significantly modifies the intensity of the emitted light, which can be understood by taking into account the orbital symmetry of the band-edge states and light polarization dipole selection rules. Our data and analysis indicate a route towards the controlled modulation of optical properties by bending the flakes, which is dependent on the layer thickness, optical excitation energy and light polarization. The proposed integration of 2D InSe with Si nanostructures exploits the flexibility of this 2D material and its compatibility with Si-platforms. These results were published in *Advanced Optical Materials*, **8**, 2000828 (2020).

9.1.2. Resonant tunnelling into the 2D subbands of InSe

This work reported on a novel type of TFETs based on a 2D InSe vdW crystal sandwiched between two multi-layered graphene electrodes. This type of vertical FET exhibits multiple regions of NDC peaks in the current-voltage characteristics and differs in several essential aspects from TFETs based on vdW crystals reported earlier.[105,119,167] These device structures exploit the tunnelling of charge carriers from a source of electrons into the distinct 2D subband states of an InSe vdW crystal a few atomic layers thick. The energy of the 2D subbands can be tuned by the thickness of the InSe layer due to the strong quantum confinement of the light effective mass electrons.[31] Our devices provide the foundation for further technologies, such as low-power consumption transistors and broad-band sources and detectors compatible with existing photonic and CMOS technologies. The results presented in this chapter were published in *Communications Physics* **3,** 16 (2020).

9.1.3. Photosensing with InSe/graphene heterostructures

We have investigated vertical FETs in which InSe is sandwiched between two multilayer graphene electrodes. These devices demonstrated potential for broadband sources and detectors. The optoelectronic transport characteristics suggest a highly favourable band alignment between InSe and graphene (in contrast to the metal-semiconductor heterojunctions), which facilitate the efficient extraction of photogenerated charge carriers. In particular, these devices revealed a strong UV photoresponsivity. To optimize the performance of InSe based photodetectors, various factors affecting the device performance have been systematically investigated. Preliminary ellipsometry measurements on bulk InSe confirmed enhanced pronounced UV resonances in the absorption. The experimental data are in good agreement with the theoretical predictions based on DFT. However, these preliminary results require further experiments and analysis.

9.1.4. Light-induced charge transfer between InSe/graphene

In this work, we exploited the effects of light on the transport properties of a hybrid field-effect phototransistor based on a graphene-contacted InSe layer encapsulated with hBN. In these devices, the transport of photoexcited carriers in InSe is largely controlled by the electric field generated at the InSe/graphene interface. The light-induced charge transfer at the InSe/graphene interface acts to photosensitize the graphene layer, giving rise to a fast and high photoresponsivity. All measurements presented in this work were obtained under quasistatic conditions so were not influenced by dynamic polarization effects. These devices were made by a relatively simple fabrication process and offer a flexible route to integration with existing Si-manufacturing technologies beyond

the capability of traditional semiconductor devices and other 2D photodetectors in the current literature.[59,200,222] These findings were published in *Advanced Functional Materials* **29**, 1805491 (2019).

9.2. Prospects

The work of this thesis suggests several avenues for further exploration. This section summarizes the future work and perspectives that arise from these results.

Layered III-VI chalcogenides, such as InSe, have a band-gap energy and electronic band structure that are very sensitive to quantum confinement.[54] For example, for InSe, as the thickness decreases from the bulk to the monolayer limit, the band-gap can be tuned from the infrared to the UV range.[31,41] This lead to a change of the optical constants, such as the psuedorefractive index (η and κ), pseudodielectric function (ε_1 and ε_2) and the absorption. Previous studies on TMDCs have identified that the absorption usually increases with the layer number.[210] A layer dependent absorption is also predicted for InSe.[99] However, a large set of samples with a controlled thickness of InSe is required to measure this dependence. Absorption measurements based on transmission spectroscopy require the 2D nanoflakes to be suspended and/or be deposited on transparent substrates, which is challenging.[210] The evolution of these optical properties with varying layer thickness can be further explored by the spectroscopic imaging ellipsometry technique.

Experimental observation of bulk InSe has demonstrated strong resonances in the UV. However, the optical transitions and electronic states responsible for such resonances remain unknown. Previous reports assigned the

UV resonances in the absorption spectra to the excitation of electrons from Se $p_x p_y$orbitals[223] and/or from deeper valence bands (consisting of In 5s and Se 4s states)[209] to the conduction band. Further systematic experimental investigations are necessary to model the optical response of InSe in the UV range.

Recent observations of intersubband transitions by near-field optics in TMDCs[177] have demonstrated the potential of 2D intersubband transitions for optoelectronics. The InSe-based TFETs demonstrated in chapter 7 have the potential for broad spectral range optoelectronics with intraband transitions tuneable from the near-infrared in a bilayer InSe to the far-infrared/terahertz range in thicker InSe films. In particular, by suitable design of the layer thicknesses, it may be possible to engineer population inversion between the subbands and tune the photon emission, as done in quantum cascade lasers based on traditional semiconductors.[178]

The potential of the 2D InSe/graphene heterostructure for photodetection based on light-induced charge transfer has already been demonstrated in this work. Further studies include probing the role of dipole-dipole interactions on the photoexcited charge transfer by ultra-fast pump-probe optical spectroscopy studies on optimized device geometries. Moreover. the integration of another 2D material with a wide-band (*e.g.* GaS, InS, hBN…) into these heterostructures could further increase the UV photoresponse and also be used to create heterojunctions devices for photovoltaics. Finally, the high electrical conductivity,[33] broad-band optical absorption,[35] and mechanical flexibility[41,54] of 2D InSe nanosheets offer exciting new routes for flexible electronics and optoelectronics.

More recently, work in collaboration with the National Physical Laboratory[224] demonstrated that 2D InSe has an anomalous low thermal conductivity, which is smaller than that of low-κ SiO_2 and decreases with reducing the lateral size and/or thickness of InSe. The thermal response was probed in free-standing InSe layers as well as layers supported by a substrate, revealing the role of interfacial thermal resistance, phonon scattering, and strain. These experimental findings are important for advancing the use of InSe in thermoelectric technologies that can benefit from the exceptional combination of the unusually low-κ and high electron mobility of this 2D material.

Finally, this thesis was based on studies of materials exfoliated from bulk crystals. However, there are exciting opportunities to move towards new approaches on the growth and fabrication of 2D materials, including epitaxial growth of atomically thin layers with precise control of composition and thickness. This will facilitate the design and fabrication of new structures for fundamental and device studies.

References

1. Nigam, T., Yiang, K.-Y. & Marathe, A. Moores law: Technology scaling and reliability challenges. *Microelectronics to Nanoelectronics: Materials, Devices & Manufacturability*, 1, (2012).

2. Iannaccone, G., Bonaccorso, F., Colombo, L. & Fiori, G. Quantum engineering of transistors based on 2D materials heterostructures. *Nature nanotechnology* **13**, 183-191, (2018).

3. Ahn, E.C. 2D materials for spintronic devices. *npj 2D Materials and Applications* **4**, 17, (2020).

4. Majumdar, A. *et al.* Hybrid 2D material nanophotonics: a scalable platform for low-power nonlinear and quantum optics. *Acs Photonics* **2**, 1160-1166, (2015).

5. Lundstrom, M. Moore's law forever? *Science* **299**, 210-211, (2003).

6. Li, M.-Y., Su, S.-K., Wong, H.-S.P. & Li, L.-J. (Nature Publishing Group, 2019).

7. Novoselov, K., Mishchenko, A., Carvalho, A. & Neto, A.H.C. 2D materials and van der Waals heterostructures. *Science* **353**, 461-473, (2016).

8. Redaelli, L. *et al.* Effect of the quantum well thickness on the performance of InGaN photovoltaic cells. *Applied Physics Letters* **105**, 131105, (2014).

9. Geim, A.K. & Novoselov, K.S. in *Nanoscience and technology: a collection of reviews from nature journals* 11-19 (World Scientific, 2010).

10. Novoselov, K.S. *et al.* Two-dimensional gas of massless Dirac fermions in graphene. *nature* **438**, 197-200, (2005).

11. Naumis, G.G., Barraza-Lopez, S., Oliva-Leyva, M. & Terrones, H. Electronic and optical properties of strained graphene and other strained 2D materials: a review. *Reports on Progress in Physics* **80**, 096501, (2017).

12. Lee, C., Wei, X., Kysar, J.W. & Hone, J. Measurement of the elastic properties and intrinsic strength of monolayer graphene. *science* **321**, 385-388, (2008).

13. Nair, R.R. *et al.* Fine structure constant defines visual transparency of graphene. *Science* **320**, 1308-1308, (2008).

14. Elias, D.C. *et al.* Control of graphene's properties by reversible hydrogenation: evidence for graphane. *Science* **323**, 610-613, (2009).

15. Cooper, D.R. *et al.* Experimental review of graphene. *International Scholarly Research Notices* **2012**, (2012).

16. Neto, A.C. *et al.* The electronic properties of graphene. *Reviews of modern physics* **81**, 109, (2009).

17. Radisavljevic, B. *et al.* Single-layer MoS 2 transistors. *Nature nanotechnology* **6**, 147-150, (2011).

18. Novoselov, K.S. *et al.* Two-dimensional atomic crystals. *Proceedings of the National Academy of Sciences* **102**, 10451-10453, (2005).

19. Terry, D.J. *et al.* Infrared-to-violet tunable optical activity in atomic films of GaSe, InSe, and their heterostructures. *2D Materials* **5**, 041009, (2018).

20. Arora, H. & Erbe, A. Recent progress in contact, mobility, and encapsulation engineering of InSe and GaSe. *InfoMat*, (2020).

21. Arya, S. & D'amico, A. Preparation, properties and applications of boron nitride thin films. *Thin Solid Films* **157**, 267-282, (1988).

22. Ishii, T. & Sato, T. Growth of single crystals of hexagonal boron nitride. *Journal of Crystal Growth* **61**, 689-690, (1983).

23. Li, L. *et al.* Quantum Hall effect in black phosphorus two-dimensional electron system. *Nature nanotechnology* **11**, 593-597, (2016).

24. Hu, Z.-X. *et al.* Interlayer electronic hybridization leads to exceptional thickness-dependent vibrational properties in few-layer black phosphorus. *Nanoscale* **8**, 2740-2750, (2016).

25. Ajayan, P., Kim, P. & Banerjee, K. van der Waals materials. *Physics Today* **69**, 38, (2016).

26. Mudd, G. *et al.* The direct-to-indirect band gap crossover in two-dimensional van der Waals Indium Selenide crystals. *Scientific reports* **6**, 39619-39629, (2016).

27. Mak, K.F. *et al.* Atomically thin MoS 2: a new direct-gap semiconductor. *Physical review letters* **105**, 136805, (2010).

28. Sun, Y. *et al.* InSe: a two-dimensional material with strong interlayer coupling. *Nanoscale* **10**, 7991-7998, (2018).

29. Yan, J. *et al.* Stacking-dependent interlayer coupling in trilayer MoS2 with broken inversion symmetry. *Nano letters* **15**, 8155-8161, (2015).

30. Chaves, A. *et al.* Bandgap engineering of two-dimensional semiconductor materials. *npj 2D Materials and Applications* **4**, 29, (2020).

31. Mudd, G.W. *et al.* Tuning the bandgap of exfoliated InSe nanosheets by quantum confinement. *Advanced Materials* **25**, 5714-5718, (2013).

32. Mudd, G. *et al.* Quantum confined acceptors and donors in InSe nanosheets. *Applied Physics Letters* **105**, 2219091-2219095, (2014).

33. Bandurin, D. *et al.* High Electron Mobility, Quantum Hall Effect and Anomalous Optical Response in Atomically Thin InSe. *Nature Nanotechnology* **12**, 223-227, (2016).

34. Wu, M. *et al.* Enhancement of photoluminescence and hole mobility in 1- to 5-layer InSe due to the top valence-band inversion: strain effect. *Nanoscale* **10**, 11441-11451, (2018).

35. Mudd, G.W. *et al.* High broad-band photoresponsivity of mechanically formed InSe–graphene van der Waals heterostructures. *Advanced Materials* **27**, 3760-3766, (2015).

36. Balakrishnan, N. *et al.* Engineering p–n junctions and bandgap tuning of InSe nanolayers by controlled oxidation. *2D Materials* **4**, 025043, (2017).

37. Zheng, T. *et al.* Layer-number dependent and structural defect related optical properties of InSe. *RSC advances* **7**, 54964-54968, (2017).

38. Shubina, T. *et al.* InSe as a case between 3D and 2D layered crystals for excitons. *Nature communications* **10**, 1-8, (2019).

39. Brotons-Gisbert, M. *et al.* Out-of-plane orientation of luminescent excitons in two-dimensional indium selenide. *Nature Communications* **10**, 3913, (2019).

40. Brotons-Gisbert, M. *et al.* Nanotexturing to enhance photoluminescent response of atomically thin indium selenide with highly tunable band gap. *Nano letters* **16**, 3221-3229, (2016).

41. SÁNCHEZ-ROYO, J.F. *et al.* in *Physics, Chemistry and Applications of Nanostructures* 189-192.

42. Zvyagin, B. in *Crystal Symmetries* 569-591 (Elsevier, 1988).

43. Ikari, T., Shigetomi, S. & Hashimoto, K. Crystal structure and Raman spectra of InSe. *physica status solidi (b)* **111**, 477-481, (1982).

44. Debbichi, L., Eriksson, O. & Lebègue, S. Two-dimensional indium selenides compounds: an ab initio study. *The journal of physical chemistry letters* **6**, 3098-3103, (2015).

45. Mudd, G.W. *III-VI metal chalcogenide semiconductor nanosheets and heterostructures*, University of Nottingham, (2016).

46. Dmitriev, A. *et al.* Investigation of the morphology of the van der Waals surface of the InSe single crystal. *Physics of the Solid State* **53**, 622-633, (2011).

47. Volykhov, A. *et al.* Study of the atomically clean InSe (0001) surface by X-ray photoelectron spectroscopy. *Russian Microelectronics* **41**, 521-526, (2012).

48. Balakrishnan, N. *et al.* Room temperature electroluminescence from mechanically formed van der Waals III–VI homojunctions and heterojunctions. *Advanced Optical Materials* **2**, 1064-1069, (2014).

49. Xiao, K., Carvalho, A. & Neto, A.C. Defects and oxidation resilience in InSe. *Physical Review B* **96**, 054112, (2017).

50. Arora, H. *et al.* Effective hexagonal boron nitride passivation of few-layered InSe and GaSe to enhance their electronic and optical properties. *ACS applied materials & interfaces* **11**, 43480-43487, (2019).

51. Wells, S.A. *et al.* Suppressing ambient degradation of exfoliated InSe nanosheet devices via seeded atomic layer deposition encapsulation. *Nano letters* **18**, 7876-7882, (2018).

52. Hamer, M.J. *et al.* Indirect to direct gap crossover in two-dimensional InSe revealed by angle-resolved photoemission spectroscopy. *ACS nano* **13**, 2136-2142, (2019).

53. Kress-Rogers, E., Nicholas, R., Portal, J. & Chevy, A. Cyclotron resonance studies on bulk and two-dimensional conduction electrons in InSe. *Solid State Communications* **44**, 379-383, (1982).

54. Mazumder, D. *et al.* Enhanced Optical Emission from 2D InSe Bent onto Si-Pillars. *Advanced Optical Materials* **n/a**, 2000828.

55. Li, Y. *et al.* Ultrasensitive tunability of the direct bandgap of 2D InSe flakes via strain engineering. *2D Materials* **5**, 021002, (2018).

56. Khoa, D.Q. *et al.* Modulation of electronic properties of monolayer InSe through strain and external electric field. *Chemical Physics* **516**, 213-217, (2019).

57. Lei, S. *et al.* Evolution of the electronic band structure and efficient photo-detection in atomic layers of InSe. *ACS Nano* **8**, 1263-1272, (2014).

58. Tamalampudi, S.R. *et al.* High performance and bendable few-layered InSe photodetectors with broad spectral response. *Nano letters* **14**, 2800-2806, (2014).

59. Koppens, F. *et al.* Photodetectors based on graphene, other two-dimensional materials and hybrid systems. *Nature nanotechnology* **9**, 780, (2014).

60. Kudrynskyi, Z.R. *et al.* Giant quantum hall plateau in graphene coupled to an InSe van der Waals crystal. *Physical review letters* **119**, 157701, (2017).

61. Bhuiyan, M.A. *et al.* Photoquantum Hall Effect and Light-Induced Charge Transfer at the Interface of Graphene/InSe Heterostructures. *Advanced Functional Materials*, 1805491-1805498, (2019).

62. Novoselov, K.S. *et al.* Electric field effect in atomically thin carbon films. *science* **306**, 666-669, (2004).

63. Katsnelson, M.I. Graphene: carbon in two dimensions. *Materials today* **10**, 20-27, (2007).

64. Zhu, Y. *et al.* Graphene and graphene oxide: synthesis, properties, and applications. *Advanced materials* **22**, 3906-3924, (2010).

65. Chen, J.-H. *et al.* Intrinsic and extrinsic performance limits of graphene devices on SiO 2. *Nature nanotechnology* **3**, 206-209, (2008).

66. Britnell, L. *et al.* Field-effect tunneling transistor based on vertical graphene heterostructures. *Science* **335**, 947-950, (2012).

67. Balandin, A.A. *et al.* Superior thermal conductivity of single-layer graphene. *Nano letters* **8**, 902-907, (2008).

68. Lee, G.-H. *et al.* High-strength chemical-vapor–deposited graphene and grain boundaries. *science* **340**, 1073-1076, (2013).

69. Elias, C. *et al.* Direct band-gap crossover in epitaxial monolayer boron nitride. *Nature Communications* **10**, 2639, (2019).

70. Watanabe, K., Taniguchi, T. & Kanda, H. Direct-bandgap properties and evidence for ultraviolet lasing of hexagonal boron nitride single crystal. *Nature Materials* **3**, 404-409, (2004).

71. Zhang, K. *et al.* Two dimensional hexagonal boron nitride (2D-hBN): synthesis, properties and applications. *Journal of Materials Chemistry C* **5**, 11992-12022, (2017).

72. Kumar, R., Rajasekaran, G. & Parashar, A. Optimised cut-off function for Tersoff-like potentials for a BN nanosheet: a molecular dynamics study. *Nanotechnology* **27**, 085706, (2016).

73. Petrone, N. *et al.* in *2015 IEEE International Electron Devices Meeting (IEDM).* 19.18. 11-19.18. 14 (IEEE).

74. Mayorov, A.S. *et al.* Micrometer-scale ballistic transport in encapsulated graphene at room temperature. *Nano letters* **11**, 2396-2399, (2011).

75. Li, L.H. *et al.* Strong oxidation resistance of atomically thin boron nitride nanosheets. *ACS nano* **8**, 1457-1462, (2014).

76. Meric, I. *et al.* Graphene field-effect transistors based on boron–nitride dielectrics. *Proceedings of the IEEE* **101**, 1609-1619, (2013).

77. Srivastava, A. & Fahad, M.S. Vertical MoS2/hBN/MoS2 interlayer tunneling field effect transistor. *Solid-State Electronics* **126**, 96-103, (2016).

78. Guo, N. *et al.* Fabrication of large area hexagonal boron nitride thin films for bendable capacitors. *Nano Research* **6**, 602-610, (2013).

79. Qian, K. *et al.* Direct observation of indium conductive filaments in transparent, flexible, and transferable resistive switching memory. *ACS nano* **11**, 1712-1718, (2017).

80. Velázquez, D. *et al.* Pulsed laser deposition of single layer, hexagonal boron nitride (white graphene, h-BN) on fiber-oriented Ag (111)/SrTiO3 (001). *Journal of Applied Physics* **119**, 095306, (2016).

81. Tan, C. *et al.* Recent advances in ultrathin two-dimensional nanomaterials. *Chemical reviews* **117**, 6225-6331, (2017).

82. Fu, L. *et al.* Direct growth of MoS2/h-BN heterostructures via a sulfide-resistant alloy. *ACS nano* **10**, 2063-2070, (2016).

83. Dean, C.R. *et al.* Boron nitride substrates for high-quality graphene electronics. *Nature nanotechnology* **5**, 722-726, (2010).

84. Duan, X. *et al.* Two-dimensional transition metal dichalcogenides as atomically thin semiconductors: opportunities and challenges. *Chemical Society Reviews* **44**, 8859-8876, (2015).

85. Chuang, H.-J. *et al.* Low-resistance 2D/2D ohmic contacts: a universal approach to high-performance WSe2, MoS2, and MoSe2 transistors. *Nano letters* **16**, 1896-1902, (2016).

86. Das, S., Demarteau, M. & Roelofs, A. Nb-doped single crystalline MoS2 field effect transistor. *Applied Physics Letters* **106**, 173506, (2015).

87. Lin, S. *et al.* Gate tunable monolayer MoS2/InP heterostructure solar cells. *Applied Physics Letters* **107**, 153904, (2015).

88. Abderrahmane, A. *et al.* High photosensitivity few-layered MoSe2 back-gated field-effect phototransistors. *Nanotechnology* **25**, 365202, (2014).

89. Fox, M. (American Association of Physics Teachers, 2002).

90. Citrin, D.S. Radiative lifetimes of excitons in quantum wells: Localization and phase-coherence effects. *Physical Review B* **47**, 3832-3841, (1993).

91. Wannier, G.H. The structure of electronic excitation levels in insulating crystals. *Physical Review* **52**, 191, (1937).

92. Frenkel, J. On the transformation of light into heat in solids. I. *Physical Review* **37**, 17, (1931).

93. Yu, H., Cui, X., Xu, X. & Yao, W. Valley excitons in two-dimensional semiconductors. *National Science Review* **2**, 57-70, (2015).

94. Wang, G. *et al.* Colloquium: Excitons in atomically thin transition metal dichalcogenides. *Reviews of Modern Physics* **90**, 021001, (2018).

95. Merle, J. *et al.* Direct-gap excitons in InSe by modulated magneto-optics and photoconductivity. *Solid State Communications* **28**, 251-255, (1978).

96. Camassel, J., Merle, P., Mathieu, H. & Chevy, A. Excitonic absorption edge of indium selenide. *Physical Review B* **17**, 4718, (1978).

97. Thygesen, K.S. Calculating excitons, plasmons, and quasiparticles in 2D materials and van der Waals heterostructures. *2D Materials* **4**, 022004, (2017).

98. Li, Y. *et al.* Enhanced Light Emission from the Ridge of Two-dimensional InSe Flakes. *Nano letters* **18**, 5078-5084, (2018).

99. Song, C. *et al.* The optical properties of few-layer InSe. *Journal of Applied Physics* **128**, 060901, (2020).

100. Wu, L., Chen, Y., Zhou, H. & Zhu, H. Ultrafast Energy Transfer of Both Bright and Dark Excitons in 2D van der Waals Heterostructures Beyond Dipolar Coupling. *ACS nano* **13**, 2341-2348, (2019).

101. Zhou, Y. *et al.* Probing dark excitons in atomically thin semiconductors via near-field coupling to surface plasmon polaritons. *Nature nanotechnology* **12**, 856-860, (2017).

102. Tartakovskii, A. Excitons in 2D heterostructures. *Nature Reviews Physics* **2**, 8-9, (2020).

103. Geim, A.K. & Grigorieva, I.V. Van der Waals heterostructures. *Nature* **499**, 419, (2013).

104. Ugeda, M.M. *et al.* Giant bandgap renormalization and excitonic effects in a monolayer transition metal dichalcogenide semiconductor. *Nature materials* **13**, 1091-1095, (2014).

105. Britnell, L. *et al.* Resonant tunnelling and negative differential conductance in graphene transistors. *Nature communications* **4**, 1-5, (2013).

106. He, K. *et al.* Tightly bound excitons in monolayer WSe 2. *Physical review letters* **113**, 026803, (2014).

107. Raja, A. *et al.* Coulomb engineering of the bandgap and excitons in two-dimensional materials. *Nature communications* **8**, 1-7, (2017).

108. Stier, A.V. *et al.* Probing the influence of dielectric environment on excitons in monolayer WSe2: insight from high magnetic fields. *Nano letters* **16**, 7054-7060, (2016).

109. He, K., Poole, C., Mak, K.F. & Shan, J. Experimental demonstration of continuous electronic structure tuning via strain in atomically thin MoS2. *Nano letters* **13**, 2931-2936, (2013).

110. Island, J.O. *et al.* Precise and reversible band gap tuning in single-layer MoSe 2 by uniaxial strain. *Nanoscale* **8**, 2589-2593, (2016).

111. Feng, J., Qian, X., Huang, C.-W. & Li, J. Strain-engineered artificial atom as a broad-spectrum solar energy funnel. *Nature Photonics* **6**, 866-872, (2012).

112. Cardona, M. & Peter, Y.Y. *Fundamentals of semiconductors*. Vol. 619 (Springer, 2005).

113. Shinada, M. & Sugano, S. Interband optical transitions in extremely anisotropic semiconductors. I. Bound and unbound exciton absorption. *Journal of the Physical Society of Japan* **21**, 1936-1946, (1966).

114. Chemla, D. *et al.* Room temperature excitonic nonlinear absorption and refraction in GaAs/AlGaAs multiple quantum well structures. *IEEE Journal of Quantum Electronics* **20**, 265-275, (1984).

115. Fujiwara, H. *Spectroscopic ellipsometry: principles and applications*. (John Wiley & Sons, 2007).

116. Tompkins, H. & Irene, E.A. *Handbook of ellipsometry*. (William Andrew, 2005).

117. Davies, J.H. *The Physics of Low-dimensional semiconductors - An Introduction*. (Cambridge University Press, 1998).

118. Mizuta, H. & Tanoue, T. *The physics and applications of resonant tunnelling diodes*. (Cambridge university press, 2006).

119. Campbell, P.M. *et al.* Enhanced resonant tunneling in symmetric 2D semiconductor vertical heterostructure transistors. *ACS nano* **9**, 5000-5008, (2015).

120. Zhao, P., Feenstra, R.M., Gu, G. & Jena, D. SymFET: A proposed symmetric graphene tunneling field-effect transistor. *IEEE Transactions on Electron Devices* **60**, 951-957, (2013).

121. Feenstra, R.M., Jena, D. & Gu, G. Single-particle tunneling in doped graphene-insulator-graphene junctions. *Journal of Applied Physics* **111**, 043711, (2012).

122. de la Barrera, S.C., Gao, Q. & Feenstra, R.M. Theory of graphene–insulator–graphene tunnel junctions. *Journal of Vacuum Science & Technology B, Nanotechnology and Microelectronics: Materials, Processing, Measurement, and Phenomena* **32**, 04E101, (2014).

123. Li, M. *et al.* Single particle transport in two-dimensional heterojunction interlayer tunneling field effect transistor. *Journal of Applied Physics* **115**, 074508, (2014).

124. Li, M.O. *et al.* Two-dimensional heterojunction interlayer tunneling field effect transistors (Thin-TFETs). *IEEE Journal of the Electron Devices Society* **3**, 200-207, (2015).

125. Esaki, L. New phenomenon in narrow germanium p− n junctions. *Physical review* **109**, 603, (1958).

126. Chang, L.L., Esaki, L. & Tsu, R. Resonant tunneling in semiconductor double barriers. *Applied physics letters* **24**, 593-595, (1974).

127. Campbell, P.M. *et al.* Band structure effects on resonant tunneling in III-V quantum wells versus two-dimensional vertical heterostructures. *Journal of Applied Physics* **119**, 024503, (2016).

128. Ishii, T. High quality single crystal growth of layered InSe semiconductor by Bridgman technique. *Journal of crystal growth* **89**, 459-462, (1988).

129. Katerinchuk, V., Kovalyuk, Z., Netyaga, V. & Betsa, T. Heterojunctions Produced from the Layered Semiconductors SnS1. 9Se0. 1and GaSe〈 Cd〉. *Inorganic materials* **37**, 336-338, (2001).

130. Watanabe, K. & Taniguchi, T. Hexagonal boron nitride as a new ultraviolet luminescent material and its application. *International Journal of Applied Ceramic Technology* **8**, 977-989, (2011).

131. Castellanos-Gomez, A. *et al.* Deterministic transfer of two-dimensional materials by all-dry viscoelastic stamping. *2D Materials* **1**, 011002, (2014).

132. Bie, Y.Q. *et al.* Site-Specific Transfer-Printing of Individual Graphene Microscale Patterns to Arbitrary Surfaces. *Advanced Materials* **23**, 3938-3943, (2011).

133. He, J., Hummer, K. & Franchini, C. Stacking effects on the electronic and optical properties of bilayer transition metal dichalcogenides MoS 2, MoSe 2, WS 2, and WSe 2. *Physical Review B* **89**, 075409, (2014).

134. Zhang, H. *et al.* Atomic force microscopy for two-dimensional materials: A tutorial review. *Optics Communications* **406**, 3-17, (2018).

135. Gupta, A., Sakthivel, T. & Seal, S. Recent development in 2D materials beyond graphene. *Progress in Materials Science* **73**, 44-126, (2015).

136. Patane, A. & Balkan, N. *Semiconductor Research: Experimental Techniques*. Vol. 150 (Springer Science & Business Media, 2012).

137. Pankove, J.I. *Optical processes in semiconductors*. (Courier Corporation, 1975).

138. Jorio, A., Dresselhaus, M.S., Saito, R. & Dresselhaus, G. *Raman spectroscopy in graphene related systems*. (John Wiley & Sons, 2011).

139. Wurstbauer, U. *et al.* Imaging ellipsometry of graphene. *Applied Physics Letters* **97**, 231901, (2010).

140. Funke, S. *et al.* Spectroscopic imaging ellipsometry for automated search of flakes of mono-and n-layers of 2D-materials. *Applied Surface Science* **421**, 435-439, (2017).

141. Funke, S. *et al.* Imaging spectroscopic ellipsometry of MoS2. *Journal of Physics: Condensed Matter* **28**, 385301, (2016).

142. Sangwan, V.K. & Hersam, M.C. Electronic transport in two-dimensional materials. *Annual review of physical chemistry* **69**, 299-325, (2018).

143. Mounet, N. *et al.* Two-dimensional materials from high-throughput computational exfoliation of experimentally known compounds. *Nature Nanotechnology* **13**, 246-252, (2018).

144. Ma, Y. *et al.* Engineering a topological phase transition in β-InSe via strain. *New Journal of Physics* **15**, 073008, (2013).

145. Li, Y., Niu, X. & Wang, J. Strain-dependent electronic structure and optical properties of monolayer indium selenide: A density functional+ tight-binding model+ many-body perturbation theory study. *FlatChem* **15**, 100092, (2019).

146. Akinwande, D., Petrone, N. & Hone, J. Two-dimensional flexible nanoelectronics. *Nature Communications* **5**, 5678, (2014).

147. Yagmurcukardes, M., Senger, R., Peeters, F. & Sahin, H. Mechanical properties of monolayer GaS and GaSe crystals. *Physical Review B* **94**, 245407-245413, (2016).

148. Zhao, Q., Frisenda, R., Wang, T. & Castellanos-Gomez, A. InSe: a two-dimensional semiconductor with superior flexibility. *Nanoscale* **11**, 9845-9850, (2019).

149. Wang, Q. *et al.* Strain Effect on Thermoelectric Performance of InSe Monolayer. *Nanoscale Research Letters* **14**, 287-296, (2019).

150. Sánchez-Royo, J.F. *et al.* Electronic structure, optical properties, and lattice dynamics in atomically thin indium selenide flakes. *Nano Research* **7**, 1556-1568, (2014).

151. Martinez-Pastor, J., Segura, A., Julien, C. & Chevy, A. Shallow-donor impurities in indium selenide investigated by means of far-infrared spectroscopy. *Physical Review B* **46**, 4607-4616, (1992).

152. Ferrer-Roca, C. *et al.* Investigation of nitrogen-related acceptor centers in indium selenide by means of photoluminescence: Determination of the hole effective mass. *Physical Review B* **55**, 6981-6987, (1997).

153. Li, Y. *et al.* Elastic properties and intrinsic strength of two-dimensional InSe flakes. *Nanotechnology* **30**, 335703, (2019).

154. Song, C. *et al.* Largely tunable band structures of few-layer InSe by uniaxial strain. *ACS applied materials & interfaces* **10**, 3994-4000, (2018).

155. Branny, A., Kumar, S., Proux, R. & Gerardot, B.D. Deterministic strain-induced arrays of quantum emitters in a two-dimensional semiconductor. *Nature Communications* **8**, 15053-15060, (2017).

156. Palacios-Berraquero, C. *et al.* Large-scale quantum-emitter arrays in atomically thin semiconductors. *Nature Communications* **8**, 15093-15099, (2017).

157. Tonndorf, P. *et al.* Single-photon emission from localized excitons in an atomically thin semiconductor. *Optica* **2**, 347-352, (2015).

158. Iff, O. *et al.* Deterministic coupling of quantum emitters in WSe2 monolayers to plasmonic nanocavities. *Opt. Express* **26**, 25944-25951, (2018).

159. Tripathi, L.N. *et al.* Spontaneous Emission Enhancement in Strain-Induced WSe2 Monolayer-Based Quantum Light Sources on Metallic Surfaces. *ACS Photonics* **5**, 1919-1926, (2018).

160. Luo, Y. *et al.* Deterministic coupling of site-controlled quantum emitters in monolayer WSe2 to plasmonic nanocavities. *Nature Nanotechnology* **13**, 1137-1142, (2018).

161. Cai, T. *et al.* Radiative Enhancement of Single Quantum Emitters in WSe2 Monolayers Using Site-Controlled Metallic Nanopillars. *ACS Photonics* **5**, 3466-3471, (2018).

162. Chaste, J. *et al.* Intrinsic Properties of Suspended MoS2 on SiO2/Si Pillar Arrays for Nanomechanics and Optics. *ACS Nano* **12**, 3235-3242, (2018).

163. Kumar, S., Kaczmarczyk, A. & Gerardot, B.D. Strain-Induced Spatial and Spectral Isolation of Quantum Emitters in Mono- and Bilayer WSe2. *Nano Letters* **15**, 7567-7573, (2015).

164. Sortino, L. *et al.* Enhanced light-matter interaction in an atomically thin semiconductor coupled with dielectric nano-antennas. *Nature Communications* **10**, 5119, (2019).

165. Bezares, F.J. *et al.* Mie resonance-enhanced light absorption in periodic silicon nanopillar arrays. *Opt. Express* **21**, 27587-27601, (2013).

166. Fiori, G. *et al.* Electronics based on two-dimensional materials. *Nature nanotechnology* **9**, 768, (2014).

167. Yan, R. *et al.* Esaki diodes in van der Waals heterojunctions with broken-gap energy band alignment. *Nano letters* **15**, 5791-5798, (2015).

168. Roy, T. *et al.* Dual-gated MoS2/WSe2 van der Waals tunnel diodes and transistors. *ACS nano* **9**, 2071-2079, (2015).

169. Liu, X. *et al.* Modulation of quantum tunneling via a vertical two-dimensional black phosphorus and molybdenum disulfide p–n junction. *ACS nano* **11**, 9143-9150, (2017).

170. Magorrian, S., Ceferino, A., Zólyomi, V. & Fal'ko, V. Hybrid k· p tight-binding model for intersubband optics in atomically thin InSe films. *Physical Review B* **97**, 165304, (2018).

171. Greenaway, M. *et al.* Tunnel spectroscopy of localised electronic states in hexagonal boron nitride. *Communications Physics* **1**, 1-7, (2018).

172. Kress-Rogers, E. *et al.* The electric sub-band structure of electron accumulation layers in InSe from Shubnikov-de Haas oscillations and inter-sub-band resonance. *Journal of Physics C: Solid State Physics* **16**, 4285, (1983).

173. Zhang, F., Sahu, B., Min, H. & MacDonald, A.H. Band structure of A B C-stacked graphene trilayers. *Physical Review B* **82**, 035409, (2010).

174. Hayden, R. *et al.* Probing the hole dispersion curves of a quantum well using resonant magnetotunneling spectroscopy. *Physical review letters* **66**, 1749, (1991).

175. Kudrynskyi, Z.R. *et al.* Resonant tunnelling into the two-dimensional subbands of InSe layers. *Communications Physics* **3**, 1-7, (2020).

176. Kuroda, N. & Nishina, Y. Resonant Raman scattering at higher M0 exciton edge in layer compound InSe. *Solid State Communications* **28**, 439-443, (1978).

177. Schmidt, P. *et al.* Nano-imaging of intersubband transitions in van der Waals quantum wells. *Nature nanotechnology* **13**, 1035-1041, (2018).

178. Faist, J. *et al.* Quantum cascade laser. *Science* **264**, 553-556, (1994).

179. in *Nanotechnology: The Future is Tiny* 85-114 (The Royal Society of Chemistry, 2016).

180. Khan, K. *et al.* Recent developments in emerging two-dimensional materials and their applications. *Journal of Materials Chemistry C* **8**, 387-440, (2020).

181. Li, X., Zhang, X., Park, H. & Di Bartolomeo, A. Editorial: Electronics and Optoelectronics of Graphene and Related 2D Materials. *Frontiers in Materials* **7**, (2020).

182. Wang, J., Mu, X., Sun, M. & Mu, T. Optoelectronic properties and applications of graphene-based hybrid nanomaterials and van der Waals heterostructures. *Applied Materials Today* **16**, 1-20, (2019).

183. Wang, J. *et al.* Recent progress on localized field enhanced two-dimensional material photodetectors from ultraviolet—visible to infrared. *Small* **13**, 1700894, (2017).

184. Bonaccorso, F., Sun, Z., Hasan, T. & Ferrari, A.C. Graphene photonics and optoelectronics. *Nature Photonics* **4**, 611-622, (2010).

185. Long, M., Wang, P., Fang, H. & Hu, W. Progress, Challenges, and Opportunities for 2D Material Based Photodetectors. *Advanced Functional Materials* **29**, 1803807, (2019).

186. Zhang, H., Wang, J., Hasan, T. & Bao, Q. Photonics of 2D materials. *Optics Communications* **406**, 1, (2018).

187. Liu, Y. *et al.* Recent Progress in the Fabrication, Properties, and Devices of Heterostructures Based on 2D Materials. *Nano-Micro Letters* **11**, 13, (2019).

188. Chen, H. *et al.* New concept ultraviolet photodetectors. *Materials Today* **18**, 493-502, (2015).

189. Shi, L. & Nihtianov, S. Comparative study of silicon-based ultraviolet photodetectors. *IEEE Sensors Journal* **12**, 2453-2459, (2012).

190. Solt, K. *et al.* PtSi–n–Si Schottky-barrier photodetectors with stable spectral responsivity in the 120–250 nm spectral range. *Applied physics letters* **69**, 3662-3664, (1996).

191. Monroy, E., Omnès, F. & Calle, F. Wide-bandgap semiconductor ultraviolet photodetectors. *Semiconductor science and technology* **18**, R33, (2003).

192. Razeghi, M. Short-wavelength solar-blind detectors-status, prospects, and markets. *Proceedings of the IEEE* **90**, 1006-1014, (2002).

193. Xie, C. *et al.* Recent progress in solar-blind deep-ultraviolet photodetectors based on inorganic ultrawide bandgap semiconductors. *Advanced Functional Materials* **29**, 1806006, (2019).

194. Wu, J. *et al.* Colossal ultraviolet photoresponsivity of few-layer black phosphorus. *ACS nano* **9**, 8070-8077, (2015).

195. Alkis, S. *et al.* Thin film MoS 2 nanocrystal based ultraviolet photodetector. *Opt. Express* **20**, 21815-21820, (2012).

196. Zheng, Z. *et al.* Flexible, transparent and ultra-broadband photodetector based on large-area WSe2 film for wearable devices. *Nanotechnology* **27**, 225501, (2016).

197. Khrapach, I. *et al.* Novel highly conductive and transparent graphene-based conductors. *Advanced materials* **24**, 2844-2849, (2012).

198. Zamora, D. & Torres, A. Method for outlier detection: a tool to assess the consistency between laboratory data and ultraviolet–visible absorbance spectra in wastewater samples. *Water science and technology* **69**, 2305-2314, (2014).

199. Bingjun, L., Wenjie, J. & Yonghui, L. Solar-blinded detector by UV radiation from missile plume [J]. *Aerospace Electronic Warfare* **6**, (2006).

200. Yan, F. *et al.* Fast, multicolor photodetection with graphene-contacted p-GaSe/n-InSe van der Waals heterostructures. *Nanotechnology* **28**, 27LT01-08, (2017).

201. Buscema, M. *et al.* Photocurrent generation with two-dimensional van der Waals semiconductors. *Chemical Society Reviews* **44**, 3691-3718, (2015).

202. Sze, S.M. *Semiconductor devices: physics and technology*. (John wiley & sons, 2008).

203. Su, G. *et al.* M. Ajayan, P.; Lou, J.; Peng, H. *Chemical vapor deposition of thin crystals of layered semiconductor SnS2 for fast photodetection application. Nano Lett* **15**, 506-513, (2015).

204. Katerinchuk, V. & Kovalyuk, M. InSe p-n Homojunction Diodes. *physica status solidi (a)* **133**, K45-K48, (1992).

205. Piacentini, M. *et al.* Electronic properties of the III-VI layer compounds GaS, GaSe and InSe. *Il Nuovo Cimento B (1971-1996)* **54**, 248-268, (1979).

206. Andriyashik, M., Yu. Sakhnovskii, M., Timofeev, V. & Yakimova, A. Optical transitions in the spectra of the fundamental absorption and reflection of InSe single crystals. *physica status solidi (b)* **28**, 277-285, (1968).

207. Choi, S.G. *et al.* Ellipsometric study of single-crystal γ-InSe from 1.5 to 9.2 eV. *Applied Physics Letters* **96**, 181902, (2010).

208. McCanny, J. & Murray, R. The band structures of gallium and indium selenide. *Journal of Physics C: Solid State Physics* **10**, 1211, (1977).

209. Mamy, R. & Couget, A. Optical properties of InSe from 2 eV to 25 eV. *Solid State Communications* **32**, 1129-1131, (1979).

210. Li, X.-L. *et al.* Determining layer number of two-dimensional flakes of transition-metal dichalcogenides by the Raman intensity from substrates. *Nanotechnology* **27**, 145704, (2016).

211. Ferrari, A.C. *et al.* Science and technology roadmap for graphene, related two-dimensional crystals, and hybrid systems. *Nanoscale* **7**, 4598-4810, (2015).

212. Feng, W., Zheng, W., Cao, W. & Hu, P. Back gated multilayer InSe transistors with enhanced carrier mobilities via the suppression of carrier scattering from a dielectric interface. *Advanced Materials* **26**, 6587-6593, (2014).

213. Chen, Z., Biscaras, J. & Shukla, A. A high performance graphene/few-layer InSe photo-detector. *Nanoscale* **7**, 5981-5986, (2015).

214. Greener, J.D.G. *et al.* High-Frequency Elastic Coupling at the Interface of van der Waals Nanolayers Imaged by Picosecond Ultrasonics. *ACS Nano* **13**, 11530-11537, (2019).

215. Wilson, N.R. *et al.* Weak mismatch epitaxy and structural feedback in graphene growth on copper foil. *Nano Research* **6**, 99-112, (2013).

216. Kistanov, A.A. *et al.* Atomic-scale mechanisms of defect- and light-induced oxidation and degradation of InSe. *Journal of Materials Chemistry C* **6**, 518-525, (2018).

217. Kang, J. *et al.* Computational study of metal contacts to monolayer transition-metal dichalcogenide semiconductors. *Physical Review X* **4**, 031005, (2014).

218. Hughes, H. & Scarfe, J. in *Electron Spectroscopies Applied to Low-Dimensional Materials* 99-160 (Springer, 2002).

219. Chen, X. *et al.* Improving the performance of graphene phototransistors using a heterostructure as the light-absorbing layer. *Nano letters* **17**, 6391-6396, (2017).

220. Georgiou, T. *et al.* Vertical field-effect transistor based on graphene–WS 2 heterostructures for flexible and transparent electronics. *Nature nanotechnology* **8**, 100-103, (2013).

221. Greener, J.D. *et al.* Coherent acoustic phonons in van der Waals nanolayers and heterostructures. *Physical Review B* **98**, 075408, (2018).

222. Goossens, S. *et al.* Broadband image sensor array based on graphene–CMOS integration. *Nature Photonics* **11**, 366-371, (2017).

223. Piacentini, M. *et al.* Electronic properties of the III-VI layer compounds GaS, GaSe and InSe. *Il Nuovo Cimento B (1971-1996)* **54**, 269-293, (1979).

224. Buckley, D. *et al.* Anomalous Low Thermal Conductivity of Atomically Thin InSe Probed by Scanning Thermal Microscopy. *Advanced Functional Materials* **31**, 2008967, (2021).